Andreev processes in two-terminal and multiterminal graphene based hybrid junctions

Zur Erlangung des akademischen Grades einer
DOKTORIN DER NATURWISSENSCHAFTEN (Dr. rer. nat.)

von der KIT-Fakultät für Physik
des Karlsruher Instituts für Technologie
genehmigte

DISSERTATION

von

M.Sc. Pandey, Preeti

Tag der mündlichen Prüfung: 06.12.2019

1. Referent: Prof. Dr. Detlef Beckmann
2. Korreferent: Prof. Dr. Wolfgang Wernsdorfer

Contents

1 Introduction **3**
- 1.1 Brief overview and Motivation . . . 3
- 1.2 Outline of the thesis . . . 5

2 Theoretical overview **7**
- 2.1 Normal metal/superconductor interfaces . . . 7
- 2.2 Andreev reflection processes . . . 10
- 2.3 Basic physics of Josephson junctions . . . 13
- 2.4 Graphene . . . 15
  - 2.4.1 Band structure . . . 16
  - 2.4.2 Klein tunnelling . . . 18
  - 2.4.3 Superconductivity in graphene . . . 19

3 Device fabrication methods and measurement set-up **23**
- 3.1 Fabrication of the h-BN/graphene/h-BN van der Waals heterostructures 24
  - 3.1.1 Exfoliation and identification of single layer graphene . . . 24
  - 3.1.2 Fabrication of the van der Waals heterostructures . . . 27
- 3.2 Fabrication of graphene devices with hybrid contacts . . . 31
  - 3.2.1 Basic fabrication processes . . . 31
  - 3.2.2 Process flow for graphene based junctions with hybrid contacts . 32
- 3.3 Measurement set-up . . . 35

4 Andreev reflection in ballistic two terminal normal metal/graphene/superconductor junctions **39**
- 4.1 Device geometry . . . 39
- 4.2 Normal state characterisation . . . 40
  - 4.2.1 Estimation of the charge carrier density . . . 41
- 4.3 Ballistic transport . . . 43

4.3.1 Effect of the asymmetric contacts on the energy dependent interference . . . 43
4.3.2 Quantum interference in the magnetic field . . . 45
4.4 Superconductivity in hybrid graphene based junctions . . . 46
4.4.1 Analytical Model . . . 47
4.4.2 Experimental results and discussion . . . 49
4.5 Conclusion . . . 54

5 Tuning the supercurrent in multiterminal graphene based Josephson junctions 55
5.1 Device geometry . . . 56
5.2 Normal state characterisation . . . 57
5.2.1 Gate dependent electronic transport . . . 57
5.2.2 Fabry-Pérot resonances and ballistic transport . . . 59
5.3 Magnetic field dependence of the supercurrent . . . 61
5.4 Tuning the supercurrent in graphene based Josephson junctions . . . 62
5.4.1 Gate voltage controlled supercurrent . . . 64
5.4.2 Tuning the supercurrent with a transverse normal current . . . 65
5.5 Conclusion . . . 70

6 Crossed Andreev reflections in multiterminal graphene based Josephson junction 71
6.1 Experimental results . . . 72
6.2 Analytical model . . . 74
6.3 Bias conditions for the crossed Andreev reflections . . . 78
6.4 Observation of the crossed Andreev reflections . . . 78
6.5 Gate dependence of the crossed Andreev reflections . . . 84
6.6 Temperature dependence of the crossed Andreev reflections . . . 87
6.7 Conclusion . . . 88

7 Summary and outlook 91

Bibliography 95

Chapter 1

Introduction

1.1 Brief overview and Motivation

Ever since the discovery of superconductivity by H. Kammerlingh Onnes in 1911, zero resistance electronic transport has been an interesting physical phenomenon in terms of fundamental physics as well as in strong industrial applications. From the point of view of fundamental physics, it is the combination of a superconductor with another metal or an insulator, that plays an important role in the devices which utilise superconductivity. The electronic transport is carried out via quantum tunnelling in case of the Josephson junctions with insulating weak links, while proximity induced superconductivity and various Andreev processes are responsible for the electronic transport in the Josephson junctions with metallic/semiconducting weak links, and in superconductor/normal metal or superconductor/semiconductor junctions [1–5]. In case of normal metal and superconductor junctions (NS junctions), the transport properties of the junctions strongly depend on the interface between the superconductor and the normal metal, *i. e.*, whether the NS junction is in the metallic regime with no interface barrier or in the tunnelling regime due to a finite interface barrier [3]. These NS junctions are of obvious interest due to the fact that while the charge transport in a normal metal is of fermionic single particle nature, the electronic transport in a superconductor in its ground state is carried out by the Cooper pairs. The conversion of two Fermi particles into a Cooper pair via the Andreev reflection is what sparks interest in these normal metal/superconductor junctions. The nature of the Andreev reflection, local (Andreev retro-reflection, multiple Andreev reflection, specular Andreev reflection) or nonlocal (crossed Andreev reflection, specular crossed Andreev reflection), strongly depends not only on the transport properties of the normal metal and the superconductor, but on their interface as well [3, 4, 6–9].

In electronic transport, graphene takes advantage over the other normal metals due to its highly tunable electronic properties [10–13]. A single layer graphene (SLG) is

a gapless semiconductor with a linear dispersion relation in the low-energy regime. It makes SLG a host of relativistic quasiparticles or massless fermions where relativistic physics can be studied in a device on a small chip without using extremely high energy. Bilayer graphene (BLG), on the other hand, has significantly different band structure from its single layer counterpart [10]. It has a gapless parabolic energy dispersion in the low-energy regime which shows massive fermions in contrast to the SLG. In both of the graphene systems, an electronic band gap can be opened by breaking the lattice inversion symmetry [10, 14]. While in a SLG system, a potential difference between the two sublattices is required to break the inversion symmetry, this symmetry breaking can be achieved comparatively easily in a BLG system by applying a potential difference between the two graphene layers [10, 14].

In case of proximity induced superconductivity, graphene has been extensively studied as a weak link between two superconductors[15–29]. However, in most of these studies the primary focus has been to measure large supercurrents and signatures of ballistic transport in the superconducting regime. In terms of Andreev processes, the focus in these studies has been on studying the multiple Andreev reflections in graphene based Josephson junctions, while a different approach was implemented by Bretheau *et al.* [30] where the authors investigated the Andreev bound states in proximitized graphene by using tunnelling spectroscopy. On the other hand, there have been very few studies where graphene has been utilised to study the properties of superconductor/normal metal interfaces with a single superconducting interface. Observation of the specular Andreev reflection in BLG based junctions [31], reflectionless tunnelling in SLG [32] and two-gap superconductivity in niobium diselenide/graphene ($NbSe_2$/SLG) junctions [33] show that graphene is a suitable material for the investigation of the Andreev processes in NS junctions. Despite its potential, the research area of graphene based NS interfaces has remained far from its Josephson junction counterpart in terms of research and development.

Drawing motivation from the above discussion, the present doctoral thesis is dedicated to the study of the Andreev processes and superconductivity in single layer graphene based devices with hybrid contacts, *i. e.*, with a combination of superconducting and normal metal contacts. To take advantage of the electronic transport properties of pristine graphene, the devices were fabricated with hexagonal boron nitride (h-BN) encapsulated graphene [34]. h-BN encapsulation shields the graphene sheet from the external contamination such as the condensation of the water molecules or hydrocarbons due to the ambient conditions, and the residues of the polymers that are used during the lithography processes. At the same time, the bottom h-BN provides a perfectly flat substrate to the overlying graphene contrary to the graphene on a Si/SiO_2 substrate. In order to achieve a better electrical contact, the metal contact to the graphene is established on its one-dimensional (1D) edges instead of the two-dimensional (2D) surface [34] by following a process similar to the one shown by Kraft *et al.* [25]. Low temperature

electronic transport characterisation of these devices was carried out by using a He^3/He^4 dilution refrigerator and standard low frequency lock-in detection technique.

1.2 Outline of the thesis

The thesis is structured as given below with the current chapter being **Chapter 1** where the subject of research is introduced.

In **Chapter 2**, a brief theoretical background is provided on the subject of the Andreev processes at the normal metal/superconductor interfaces, proximity induced superconductivity, and electronic transport in graphene. This chapter includes the recent developments in the research area of interest.

Device fabrication techniques, and experimental methods employed for the fabrication and characterisation of the devices are described in **Chapter 3**. This chapter mainly focuses on the van der Waals assembly of the h-BN/graphene/h-BN heterostructures, the processes defining the edge-contact geometry of the devices, and the low temperature electronic transport measurement setup.

In **Chapter 4**, experimental characterisation of the devices with simple two-terminal normal metal/graphene/superconductor junctions is shown and discussed. These devices were characterised in the normal state where the device configuration is NGN′ (normal metal/graphene/normal metal, N′ denotes the normal state of the superconductor) due to two different normal metals, and in the superconducting state where the device configuration is NGS (normal metal/graphene/superconductor). A modified Octavio-Tinkham-Blonder-Klapwijk (OTBK) model [4] and a generalized Blonder-Tinkham-Klapwijk (BTK) model [3, 35, 36] were used to explain the experimental results obtained in the superconducting regime.

The experimental results obtained from the multiterminal graphene based devices are discussed in **Chapter 5**. These devices were fabricated to provide two transverse graphene based junctions in the configuration SGS (superconductor/graphene/superconductor) and NGN (normal metal/graphene/normal metal). This chapter is primarily focused on the tuning of the supercurrent across the SGS junction by applying a current across the NGN junction.

Chapter 6 shows the experimental results obtained from the same multiterminal device as shown in Chapter 5, however, here, the focus of the study is the nonlocal Andreev reflection. These graphene based multiterminal devices offer a perfect testbed for tunable nonlocal transport. Signatures of the crossed Andreev reflections were observed and traced as a function of the gate voltage as well as temperature. Along with the modified OTBK model and the generalized BTK model used to explain the superconducting transport properties in these devices, a three-terminal beam splitter model was employed

to explain the observed crossed Andreev reflection.

Chapter 7 concludes the thesis with a summary of the experimental results that were presented and discussed in the previous chapters. In addition, an outlook on the future research work in the field of graphene based hybrid junctions is shared.

Chapter 2

Theoretical overview

The electronic transport in a metal or a semiconductor is due to the fermions with half-integer spin which follow the Fermi-Dirac distribution. In a conventional superconductor, on the other hand, the electronic transport is due to the bound pairs of electrons having equal and opposite momentum and spin, very well-known as the Cooper pairs after the Bardeen-Cooper-Schrieffer (BCS) theory of superconductivity.

In this chapter, a brief theoretical overview of the Andreev processes (which account for the transport between a normal metal and a superconductor) and Josephson junctions is provided that forms the basis of this research work. It is followed by an introduction to the electronic transport properties of graphene and its role as a material of interest in terms of superconductivity.

2.1 Normal metal/superconductor interfaces

In a normal metal/superconductor (NS) junction, when the Fermi energy of an incident electron from the metal lies within the superconducting gap, charge transport across the junction takes place by a process known as the Andreev reflection. In 1964, A. F. Andreev showed that an electron which incidents from the N on the NS-interface has a finite probability of being retro-reflected as a hole in N [2]. Due to the conservation of momentum, this Andreev reflected hole travels along the same path as the incident electron and its group velocity changes sign. The Andreev reflection probability, however, depends strongly on the interface between the metal and superconductor as was shown by Blonder, Tinkham and Klapwijk which is widely known as the BTK model [3]. In this section, a brief description of this model has been provided to gain an insight into the NS interfaces.

Fig. 2.1(a) shows the processes considered by the BTK model at an NS interface in the dynamic equilibrium, the figure is taken from reference [3]. In equilibrium, all

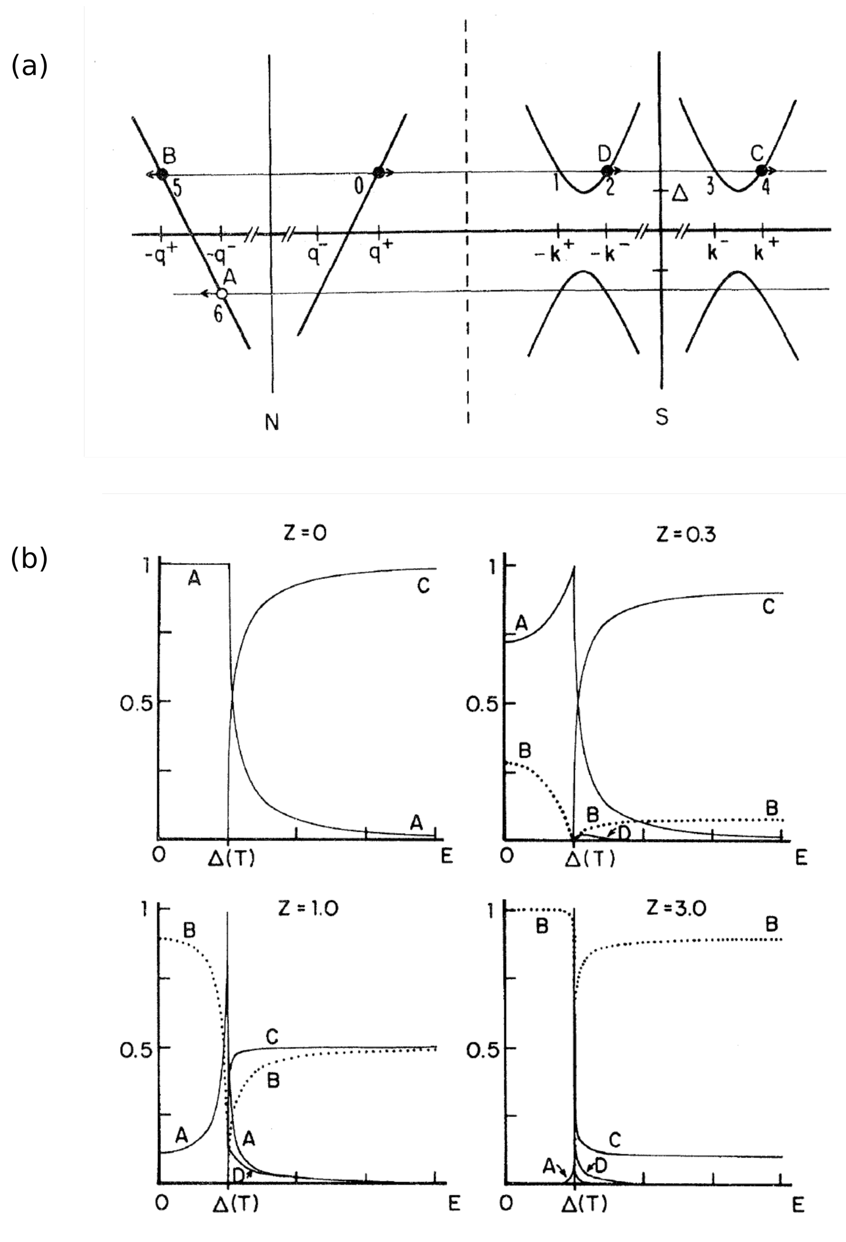

Figure 2.1: .(a) Energy vs. momentum diagram at an NS interface in dynamic equilibrium. Closed circles denote electrons and open circles denote holes. The arrows point in the direction of group velocity. The figure describes an incident electron (0) with the resulting transmitted (2, 4) and reflected (5,6) particles. (b) Plots of reflection and transmission coefficients at an NS interface. A denotes the Andreev reflection probability, B gives the normal reflection probability, C gives transmission probability without branch crossing, and D gives the transmission probability with branch crossing. Z denotes the barrier strength at the NS interface. *Figure taken from reference* [3].

the quasiparticle states denoted by 0, 1, 2, 3, 4 and 5 are occupied with the same probability $f_0(E)$. It also gives the probability of a hole at $-E$ labelled as state 6 in the figure. However, as the particles approach the NS interface, they are transmitted or reflected with certain probabilities. The four processes *A, B, C*, and *D* show the Andreev reflection, normal reflection, transmission without branch crossing, and transmission with branch crossing, respectively, if the energy E of the incident electron is greater than the superconducting gap Δ as shown in the figure.

Blonder *et al.* calculated these reflection and transmission probabilities in the presence of a barrier at the NS interface, as shown in Fig. 2.1(b), which ranges from the metallic regime ($Z = 0$) with no barrier to the intermediate regime ($Z = 3$) with a finite barrier. In the figure, the parameter Z denotes the barrier strength (dimensionless) which is related to the transmission coefficient τ according to the relation $\tau = (1 + Z^2)^{-1}$, and to the reflection coefficient r as $r = Z^2/(1+Z^2)$. Note that the four probabilities, the reflection probabilities $A(E), B(E)$, and the transmission probabilities $C(E), D(E)$, are bound by the condition $A(E) + B(E) + C(E) + D(E) = 1$, due to the conservation of probability. In Fig. 2.1(b), it can be seen that as the barrier strength increases, the reflection and transmission probabilities change significantly. The Andreev reflection probability $A(E)$ is the quantity of interest in the present case, and it can be followed that $A(E) = 1$ in the metallic contact regime, no barrier since $Z = 0$, *i. e.*, a perfect contact between the normal metal and the superconductor. $A(E)$ decreases as Z increases, reducing to close to zero in the case of strong barriers (corresponding to $Z = 3$ case in Fig. 2.1(b)). The model signifies the importance of the interface between the normal metal and the superconductor for the observation of the Andreev reflection.

Blonder *et al.*, calculated the current-voltage ($I - V$) characteristics of these NS junctions at a finite voltage with the following relation:

$$I = 2N(0)ev_F\mathcal{A}\int_{-\infty}^{\infty}[f_0(E-eV) - f_0(E)][1 + A(E) - B(E)]dE \tag{2.1}$$

where $N(0)$ denotes the spin-split density of states (prefactor 2 takes into account the spin degeneracy), v_F is the Fermi velocity, $\mathcal{A}$ is the effective cross-sectional area, $f_0(E)$ is the distribution function of the incoming electrons from the S side, and $f_0(E - eV)$ is the distribution function of the incoming electrons from the N side with the accelerating voltage V.

The quantity $[1 + A(E) - B(E)]$ in Eqn. 2.1 denotes the spectral conductance, and it can be readily seen that the Andreev reflection increases the current while the normal reflection decreases it. Fig. 2.2 shows the differential conductance normalized with the normal state conductance $R_N(dI/dV)$ as a function of the bias voltage V. The evolution of these curves with the increasing barrier strength shows the diminishing of the Andreev

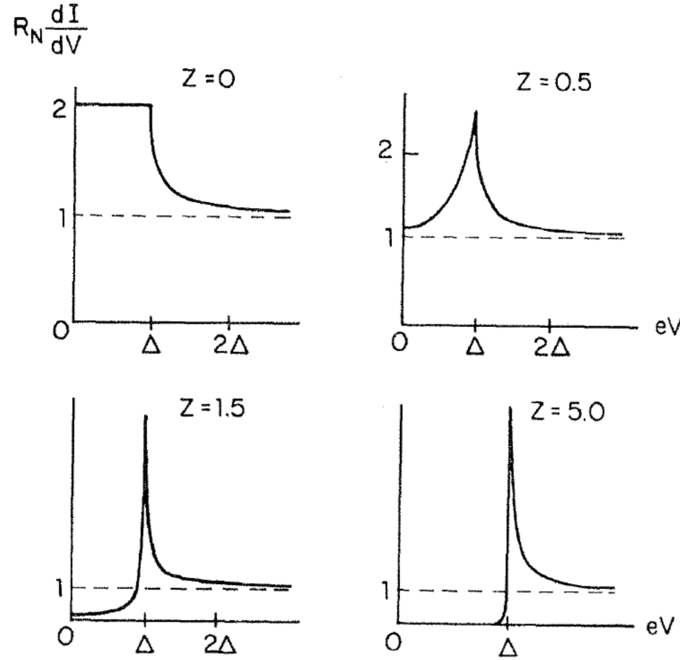

Figure 2.2: Differential conductance normalized by the normal state conductance $R_N(dI/dV)$ as a function of an applied bias across the NS junction for various barrier strengths at $T = 0$. The calculated quantity is proportional to the spectral conductance at $E = eV$. *Figure taken from reference* [3].

reflection probability in the region $eV \leq \Delta$. To summarise, according to the BTK model, information about the NS-interface in a normal metal/superconductor junction can be obtained by analysing its subgap differential conductance.

2.2 Andreev reflection processes

Energy conservation in an Andreev process requires $|E_\mathrm{e}| = |E_\mathrm{h}|$, where E_e and E_h denote the energies of the incident electron and the Andreev reflected hole, respectively. Therefore, a hole is generated as far below the Fermi level as the incident electron is above the Fermi level [3].

In case of a metallic junction with a single superconducting interface, two distinct Andreev reflection processes can be realized which depend on the excitation energy E of the incident particle, the Fermi energy E_F and the superconducting gap Δ. The first process is the Andreev retroreflection process in which the hole is reflected in the conduction band of the normal metal. This reflected hole travels back through the same path as the incident electron, which means $\theta_\mathrm{inc} = -\theta_\mathrm{ref}$ for a perfect retro reflection where θ_inc and θ_ref denote the angle of incidence and reflection, respectively. In this case, all components of the velocity change sign for the retroreflected hole. Andreev retroreflection

is the primary process for the electronic transport across the NS junctions in case of a normal metal. Fig. 2.3(a) and (b) show the illustration of the Andreev retroreflection process. In NS junctions, as shown in the previous section, the Andreev reflection probability depends on the interface of the normal metal and the superconductor. In case of a point-contact NS junction with no barrier, the subgap conductance of the junction becomes twice of its normal state conductance due to the Andreev reflections [3].

It was shown by Beenakker in 2006 [7] that a distinct Andreev reflection process can be realized in NS junctions with zero-gap semiconductors for excitations with energy $E \leq \Delta$ if $E_{\mathrm{F}} \leq \Delta$. Under these conditions, for an incident electron the reflected hole might appear in the valence band instead of the conduction band, a process known as the specular Andreev reflection ($\theta_{\mathrm{inc}} \approx \theta_{\mathrm{ref}}$), that can be observed if E_{F} can be tuned close to the charge neutrality point of the zero-gap semiconductor [7–9]. It was experimentally observed in bilayer graphene/niobium diselenide (BLG/$NbSe_2$) junctions [31]. Fig. 2.3(c) and (d) show the illustration of the specular Andreev reflection.

It is to be noted that both of the above mentioned Andreev reflection processes, Andreev retroreflection and specular Andreev reflection, require only one NS interface. Since the reflected hole always resides in the same normal metal or semiconductor, these processes are known as the local Andreev processes.

An entirely different reflection process can be realized in the presence of more than one NS interface. In a general case, considering a normal metal/superconductor/normal metal (NSN) junction, it is also possible for an incident electron from one N to be reflected as a hole in the other N through S, as long as the distance between the two N terminals is smaller than the superconducting coherence length. In such a case, the incident electron and the reflected hole reside in two different N terminals, however, the phase coherence between the electron and the hole is maintained due to the Andreev reflection. This coherence between two spatially separated particles is the manifestation of quantum entanglement between the incident electron and the reflected hole in space. Such a reflection process is known as the nonlocal Andreev reflection or crossed Andreev reflection (CAR). This process can be observed in a SNS junction as well, where, for instance, the electron from the N terminal incidents on one of the NS interfaces, and gets reflected as a hole into the other S terminal. Fig. 2.3(e) and (f) show the illustration of CAR in an NSN junction. However, in these junctions, there are two other competing processes, one is the Andreev retroreflection and the second is the elastic co-tunnelling. In the case of elastic cotunnelling, the incident electron from the N terminal tunnels through the S to the other N without generating the Cooper pair in the S terminal.

CAR was originally proposed to be observed in ferromagnet/superconductor structures by taking advantage of the spin-selectivity [37, 38], however, theoretical studies were further extended to observe CAR in normal metal/superconductor junctions as well [39]. Experimental observation of CAR has been reported in ferromagnet/superconductor

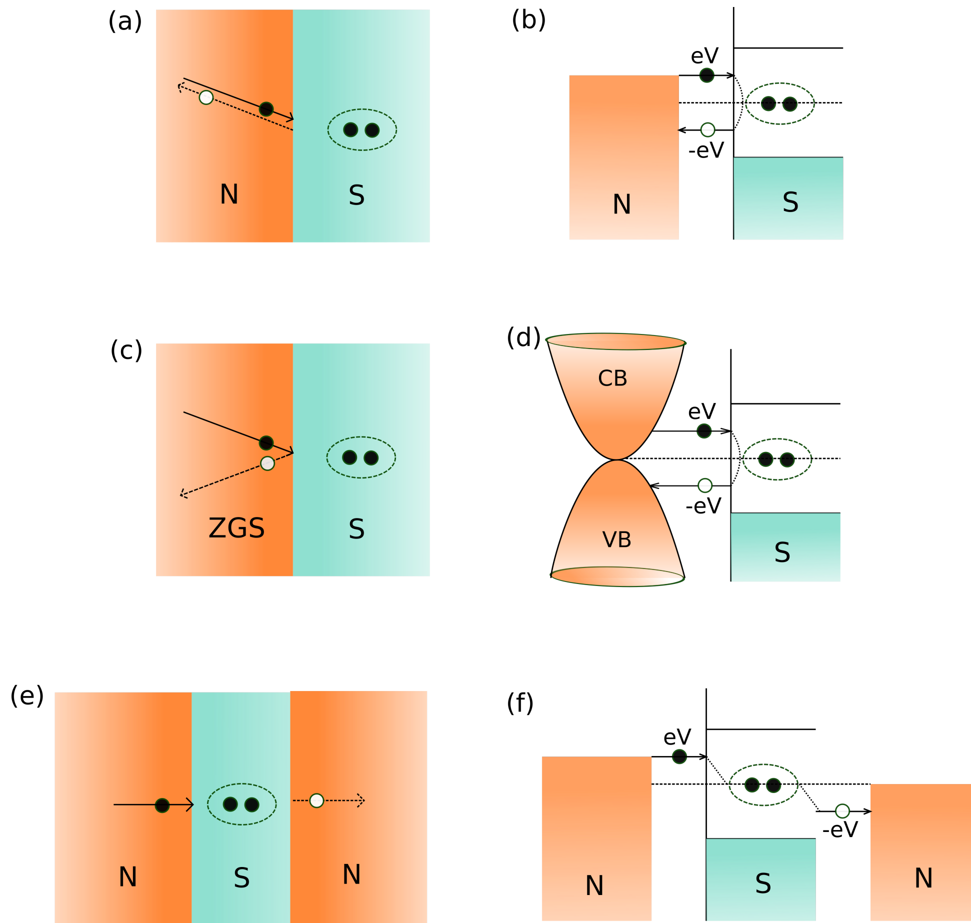

Figure 2.3: Illustration of the Andreev processes. (a) and (b) Andreev retroreflection, (c) and (d) Specular Andreev reflection (ZGS: Zero Gap Semiconductor, CB: Conduction Band, VB: Valence Band) (Figure adapted from [31]), (e) and (f) Crossed Andreev reflection. (Filled and empty circles denote electrons and holes, respectively.)

structures [40, 41] in the metallic regime where the nonlocal spin valve signal was used as a probe for CAR. In normal metal/superconductor structures, CAR has been observed in the tunnelling regime [42] as well as in the metallic regime [43]. Manifestation of CAR in the form of Cooper pair splitting, where a Cooper pair from a S terminal is split between two different N terminals, has been reported in quantum dot systems [44–50]. Crossed Andreev effects were proposed to be observed in the superconductor/quantum Hall systems where the chiral edge states result in CAR [51, 52], and were recently observed in an encapsulated graphene device in the quantum Hall regime [53].

In case of a superconductor/normal metal/superconductor (SNS) junction known as the Josephson junction (here, N can be replaced by a semiconductor as well), while all of the above Andreev reflection processes are possible, another Andreev process known as the multiple Andreev reflection (MAR) can be observed. This process gives rise to the subgap conductance features in the conductance spectrum of the junction according

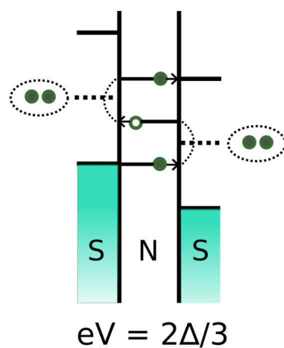

Figure 2.4: Schematic representation of multiple Andreev reflections for an incident electron from the left onto the right superconductor ($N = 3$). Filled and empty circles denote the electrons and holes, respectively.

to the relation $V = 2\Delta/Ne$ where V denotes the bias voltage across the Josephson junction and N is an integer [4, 5, 54]. This process is shown in Fig. 2.4. An electron with energy eV incidents on the right S terminal and is reflected as a hole in the N. This Andreev reflected hole gains the energy eV due to the electric field while it travels back to the right terminal. Here, the hole is Andreev reflected into an electron in N which can go through the same process as the previous electron. After multiple iterations of this process, the particle can be transmitted as a quasiparticle above 2Δ. These multiple iterations generate conductance features in the subgap condutance spectrum and strongly depend on the scattering in the N terminal as well as on the transparency of the NS interfaces.

2.3 Basic physics of Josephson junctions

This subsection is primarily based on [5].

First proposed by Josephson in 1962 [1], Josephson junctions have been extensively studied due to their apparent application in tunable superconductivity. Josephson predicted that a finite supercurrent can flow between two superconductors separated by a thin insulating layer due to quantum tunnelling. The supercurrent in such a junction was described by the relation

$$I_s = I_c \sin\phi \tag{2.2}$$

where I_c, known as the critical current, denotes the maximum supercurrent that can be supported by the Josephson junction before it becomes resistive, and ϕ denotes the gauge-invariant macroscopic phase-difference between the two superconductors. Under a finite voltage V across the junction, ϕ was predicted to be modulating with time

according to the relation

$$\frac{d\phi}{dt} = \frac{2eV}{\hbar} \tag{2.3}$$

It results in an alternating current with the amplitude of I_c and frequency $\nu = 2eV/h$, also known as the Josephson frequency. These two effects are known as the dc and ac Josephson effects. It was later found that the Josephson junctions are not limited just to the insulators (corresponding to quantum tunnelling process), but can be extended to metal and semiconductor weak links as well due to the proximity induced superconductivity.

While the ideal dc Josephson effect can be described by Eqn. 2.2, in case of an ac Josephson effect, the Josephson junction is described by the resistively-capacitively shunted junction (RCSJ) model. This model shunts the ideal Josephson junction with a resistance R and a capacitor C. The resistor corresponds to the dissipation in the presence of finite bias without affecting the dc response of the junction. The capacitor C corresponds to the geometric capacitance between the two superconductors. The total current through the junction can, then, be defined by three parallel current components, *i. e.*, for a bias current I, the junction can be defined as

$$I = I_{c0} \sin\phi + V/R + C\,(dV/dt) \tag{2.4}$$

where I_{c0} denotes the actual critical current through the ideal Josephson junction which can be greater than the observable critical current I_c in this case. Using the voltage dependent phase-modulation, Eqn. 2.4 can be further simplified to give

$$I/I_{c0} = \sin\phi + Q^{-1}(d\phi/d\tau) + d^2\phi/d\tau^2 \tag{2.5}$$

where $\tau = \omega_p t$ is a dimensionless time variable, $\omega_p = (2eI_{c0}/\hbar C)^{1/2}$ is the plasma frequency of the junction, and $Q = \omega_p RC$ is the quality factor which characterises the damping of the junction. Depending on the value of Q, the junctions are categorised as overdamped junctions ($Q \ll 1$ corresponding to very small C), and underdamped junctions ($Q > 1$ corresponding to large C).

If a Josephson junction is irradiated with a radiation of frequency ω, the supercurrent in the junction shows constant-voltage steps known as the Shapiro steps at voltages $V_n = n\hbar\omega/2e$ [5, 55, 56]. Beginning with a simple case of an ideal Josephson junction, if an ac voltage bias of an angular frequency ω is applied in addition to the dc bias, the voltage across the junction can be described as

$$V = V_0 + V_1 \cos(\omega t) \tag{2.6}$$

The phase difference ϕ across the junction can be determined by integrating Eqn. 2.6 according to the relation shown in Eqn. 2.3, and results in

$$\phi(t) = \phi_0 + \frac{2e}{\hbar}V_0 t + \frac{2e}{\hbar\omega}V_1 \sin(\omega t) \tag{2.7}$$

where ϕ_0 is a constant of integration and $(2e/\hbar)V_0$ is the Josephson frequency ω_J. Substituting $\phi(t)$ in Eqn. 2.2 to obtain the supercurrent in the junction, and using Bessel functions for the expansion of the sine of a sine, Eqn. 2.2 can be written as

$$I_s = I_c \Sigma (-1)^n J_n(\frac{2e}{\hbar\omega}V_1) \sin(\phi_0 + \omega_J t - n\omega t) \tag{2.8}$$

It is clear from Eqn. 2.8 that a dc component is observed when $\omega_J = n\omega$, in other words, when the dc voltage V_0 takes the values

$$V_n = n\frac{\hbar\omega}{2e}, \tag{2.9}$$

it generates step-like features in the current at these voltages in the $I - V$ characteristics of the junction, and these features are known as the Shapiro-steps.

A phenomenon known as the dual Shapiro steps, can be observed in Josephson junctions with phase-slip centers (where the superconducting phase changes in discontinuous steps due to the localized resistive centers in the junction). In these junctions, equidistant steps in the voltage can be observed when the current increases beyond I_c. This phenomenon was first observed in long tin-whiskers by Webb *et al.* [57] in 1968, and studied in detail by Meyer *et al.* [58] in 1972. In the quantum phase-slip regime, these dual Shapiro steps are of interest as they represent the charge-phase duality of a superconductor [59–61].

2.4 Graphene

While the theoretical study on the electronic band structure of graphene was already developed in 1947 [62], the first experimental study on few layer graphene was reported by Novoselov *et al.* [63] in 2004. The authors showed the stable existence of few atomic layers of graphite (or multilayer graphene) and the possibility to use this material for charge transport in the field effect transistors. It was later shown that a single layer of graphite, known as graphene or single layer graphene (SLG), is also stable under ambient conditions [64], and can be employed for studying the Dirac fermions [65] owing to its relativistic band structure in the low-energy regime [7, 10, 62]. In the present section, a brief introduction is provided to the SLG in terms of its electronic transport properties. It is to be noted that SLG and BLG have very different electronic band structures, *e. g.* SLG has a linear dispersion in the low-energy regime which indicates massless Dirac fermions and exhibits the Klein tunnelling, while BLG has a parabolic dispersion which indicates massive fermions and exhibits the anti-Klein tunnelling [10].

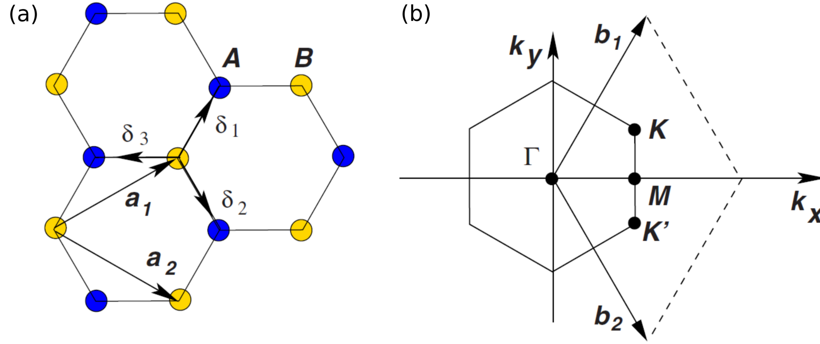

Figure 2.5: (a) Graphene lattice in real space. Blue and yellow dots indicate the two sublattices, A and B. (b) Reciprocal lattice vectors and high symmetry points in the Brillouin zone *Figure taken from reference* [11].

2.4.1 Band structure

This subsection is primarily based on references [9–11].

Graphene is a two-dimensional (2D) atomic plane in which carbon atoms are arranged in a honeycomb lattice formed by two sublattices, A and B. Each atom in sublattice A is surrounded by three atoms from the sublattice B as shown in Fig. 2.5(a). The Bravais lattice can be described with the lattice vectors

$$\vec{a_1} = \frac{a}{2}(3, \sqrt{3}), \qquad \vec{a_2} = \frac{a}{2}(3, -\sqrt{3}), \tag{2.10}$$

where $a \approx 1.42$ Å denotes the nearest-neighbour distance and the lattice constant is defined as $|a_c| = \sqrt{3}a \approx 2.46$ Å. The honeycomb lattice contains two atoms in each primitive cell which belong to the two sublattices, A and B. The nearest neighbour vectors are given as

$$\vec{\delta_1} = \frac{a}{2}(1, \sqrt{3}), \qquad \vec{\delta_2} = \frac{a}{2}(1, -\sqrt{3}), \qquad \vec{\delta_3} = a(-1, 0). \tag{2.11}$$

The reciprocal lattice can be described with the lattice vectors

$$\vec{b_1} = \frac{2\pi}{3a}(1, \sqrt{3}), \qquad \vec{b_2} = \frac{2\pi}{3a}(1, -\sqrt{3}), \tag{2.12}$$

as shown in Fig. 2.5(b).

The electronic band structure of graphene was first developed by Wallace in 1947 with the tight-binding model to explain the electronic and optical properties of graphite [62]. The conduction and the valence band form conically shaped valleys which touch each other at the six corners of the first Brillouin zone as shown in Fig. 2.6. These points, where the two bands touch each other, are known as the Dirac points and belong to two inequivalent set of points known as K and K' given by the wave vectors

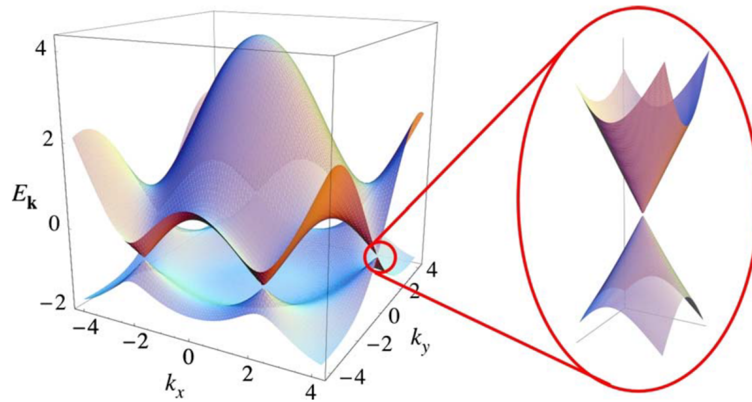

Figure 2.6: Electronic band structure of graphene (left) and zoom in of the energy bands close to one of the Dirac points (right). *Figure taken from reference* [11].

$$\vec{K} = \frac{2\pi}{3a}(1, \frac{1}{\sqrt{3}}), \qquad \vec{K'} = \frac{2\pi}{3a}(1, -\frac{1}{\sqrt{3}}) \tag{2.13}$$

With the nearest-neighbour hopping energy $t \approx$2.8eV and the next nearest-neighbour hopping energy $t' \approx$0.1eV [11], the dispersion relation can be written as

$$E_{\pm}(\vec{k}) = \pm t\sqrt{3 + f(\vec{k})} - t' f(\vec{k}) \tag{2.14}$$

$$f(\vec{k}) = 2\cos(\sqrt{3}k_y a) + 4\cos(\frac{\sqrt{3}}{2}k_y a)\cos(\frac{3}{2}k_x a), \tag{2.15}$$

where the $+$ sign denotes the conduction band and the $-$ sign denotes the valence band. It is clear from the dispersion relation that the band structure is symmetric around zero energy if t' =0. For finite values of t', the electron-hole symmetry is broken. In the low-energy regime where $|E| \ll |t|$, the electronic transport in graphene is governed by the relation

$$E_{\pm}(\vec{k}) = \pm\hbar v_{\mathrm{F}}|\vec{k}| \tag{2.16}$$

where

$$v_{\mathrm{F}} = \frac{3a|t|}{2} \approx 10^6\, m/s$$

is the Fermi velocity.

Due to the linear energy dispersion shown in eqn. 2.16, the low energy excitations in graphene have zero effective mass. These excitations are governed by the Dirac equation for the relativistic particles. The Hamiltonian in the linear regime can be defined as:

$$H_K = v_{\mathrm{F}}\sigma\vec{k}, \qquad H_{K'} = v_{\mathrm{F}}\sigma^*\vec{k} \tag{2.17}$$

for the K and K' points where $\sigma = (\sigma_x, \sigma_y)$ and $\sigma^* = (\sigma_x, -\sigma_y)$ show the Pauli matrices. Here, the spin degree of freedom described by the Pauli matrices is called the 'pseudospin', to distinguish it from the real electron spin, and it appears because of the two independent sublattices. The momentum space wave functions around the K and the K' points are defined as

$$\Psi_{\pm,K}(\vec{k}) = \frac{1}{\sqrt{2}}(e^{-i\theta_{\vec{k}}/2}, \pm e^{i\theta_{\vec{k}}/2}), \qquad \Psi_{\pm,K'}(\vec{k}) = \frac{1}{\sqrt{2}}(e^{i\theta_{\vec{k}}/2}, \pm e^{-i\theta_{\vec{k}}/2}). \tag{2.18}$$

where the $+$ and $-$ signs correspond to the conduction and the valence bands, respectively, and

$$\theta_{\vec{k}} = \arctan(\frac{k_x}{k_y})$$

. Therefore, the complete low-energy Hamiltonian is a 4 x 4 matrix which accounts for the two sublattices and the two inequivalent conical points, K and K', and can be defined as:

$$H = \begin{pmatrix} H_K & 0 \\ 0 & H_{K'} \end{pmatrix} \tag{2.19}$$

In terms of electronic transport in the low-energy regime (for massless Dirac fermions) [11, 66], the electron density n is related to the Fermi momentum k_F as per the relation $k_F = \sqrt{n\pi}$.

2.4.2 Klein tunnelling

In quantum mechanics, a non-relativistic particle has a finite probability of penetrating through a potential barrier which is higher than its energy. However, the transmission through the barrier in this case decreases exponentially with the height and the width of the barrier. Klein tunnelling refers to the relativistic phenomenon in which a Dirac particle can be transmitted through a potential barrier which is higher than its energy while the transmission probability τ depends very weakly on the barrier height [67]. It can be understood by the fact that the Dirac Hamiltonian allows for both types of the energy states, *i. e.*, the positive and negative energy states corresponding to the electrons and holes, respectively. In such a case, a barrier which is repulsive for the electrons is attractive for the holes and vice versa. Considering a positive potential barrier for instance, the electron states outside the barrier are aligned with the hole states inside the barrier for the Klein tunnelling.

Due to the relativistic band structure of graphene, Katsnelson *et al.* [68] proposed the observation of Klein tunnelling in graphene. The authors showed an angle-dependent transmission profile for Klein tunnelling in single layer graphene where the barrier becomes completely transparent at certain incidence angles as shown in Fig. 2.7 for

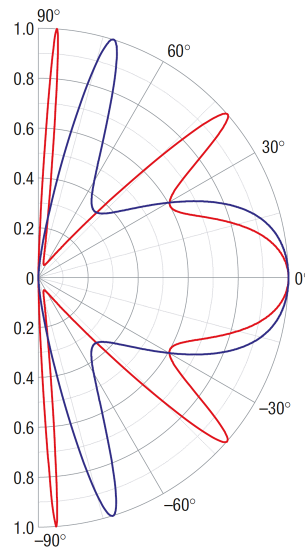

Figure 2.7: Angle dependence of the Klein tunnelling in single layer graphene. Transmission probability τ as a function of the incident angle for a 100 nm wide barrier with barrier heights 200 (red curve) and 285 (blue curve) meV for an incident energy of ≈80 meV. *Figure taken from reference* [68].

sharp potential barriers. The sharp barrier assumption is valid if the Fermi wavelength is larger than the width of the edge smearing of the potential barrier. Most importantly, the barrier remains perfectly transparent for the incidence angles close to zero. This process can be understood by considering the conservation of the sublattice pseudospin which results in the prohibition of intervalley scattering as shown in Fig. 2.8. An electron from the red branch having a pseudospin σ (*i. e.*, belonging to a specific valley) can be scattered only to a hole state in the same branch with pseudospin σ. This electron cannot be scattered into any state in the green branch as it would require for the electron to flip its pseudospin. In the absence of pseudospin-flip processes, this condition results in a perfect transmission ($\tau = 1$) through the barrier since backscattering is prohibited.

Potential barriers in graphene can be easily created by electrostatic doping through a gate electrode and hence, provide an easy way to study the Klein tunnelling. The first experimental report on the observation of Klein tunnelling in graphene was presented by Young *et al.* [69] where the authors studied quantum interference pattern in an electrostatically induced npn junction in the presence of magnetic field.

2.4.3 Superconductivity in graphene

This section is dedicated mainly to experimental reports in single layer graphene systems.

The first experimental study on the proximity induced superconductivity in graphene was performed by Heersche *et al.* [70]. The authors reported proximity induced super-

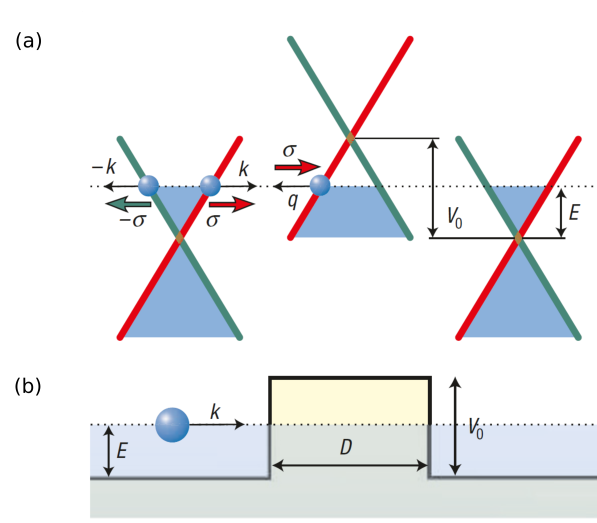

Figure 2.8: Tunnelling process in graphene through a potential barrier. (a) The red and the green curves show the linear spectrum in the low-energy regime originating from the crossing between the energy bands that belong to the sublattices A and B. (b) Potential barrier of height V_0 and width D corresponding to (a). *Figure taken from reference*[68].

conductivity in electrostatically doped graphene where a supercurrent can be carried by electrons in the conduction band (n-type doping) or holes in the valence band (p-type doping). This property makes graphene a bipolar supercurrent transistor. An important step in this direction was the co-existence of the quantum Hall effect and superconductivity as demonstrated in graphene based Josephson junctions by Rickhaus *et al.* [71] followed by another report by Komatsu *et al.* [72]. However, most of the early studies in the field of proximity induced superconductivity in graphene were conducted in the diffusive regime.

Owing to the improvement in device fabrication methods, ballistic Josephson junctions were realized in suspended graphene devices [73, 74]. However, the major improvement in graphene based Josephson junctions can be attributed to hexagonal boron nitride (h-BN) encapsulated graphene devices (extensive freedom in the substrate-supported device architecture as compared to the suspended devices) which exhibit large supercurrent and ballistic interferences [16, 17, 19, 21, 23, 24]. Amet *et al.* reported the observation of ballistic supercurrent in the quantum Hall regime using encapsulated graphene based Josephson junctions [18] which indicates the possibility to use these devices for topological superconductivity. Nanda *et al.* studied the current-phase relation (CPR) in encapsulated graphene based superconducting quantum interference devices (SQUID) and found that the CPR in these devices is skewed in contrast to the sinusoidal CPR for Josephson junctions [22]. Moreover, this skewness can be tuned as a function of an applied gate voltage. Gate tunable microwave circuits were exhibited in encapsulated graphene Josephson junctions by Schmidt *et al.* [26] and Kroll *et al.* [27]. Recent progress

in graphene based Josephson junctions was the study by Draelos *et al.* [28] where the authors studied supercurrent flow in multiterminal Josephson junctions.

In terms of graphene based devices with a single superconducting interface, there are very few reports and even fewer regarding single layer graphene. The first experimental report on this subject was presented by Popinciuc *et al.* [32], where the authors observed a zero bias conductance peak in a superconductor/graphene/normal metal (SGN) junction. This zero bias conductance peak was attributed to the reflectionless tunnelling in the device which results from diffusive transport through the graphene channel. Another report on the NGS junctions was presented by Efetov *et al.* [31] which showed the signatures of specular Andreev reflection in a bilayer graphene device as originally proposed by Beenakker for a single layer graphene system [7]. Han *et al.* [33] employed a few layer graphene as a probe to investigate the superconducting gap structure of $NbSe_2$. The most recent report in the context of single layer graphene was presented by Lee *et al.* [53], where the authors employed a h-BN/graphene/h-BN heterostructure with a finger-like superconducting contact made of niobium nitride (NbN) to study crossed Andreev conversion in the quantum Hall regime. This phenomenon was theoretically proposed by Clarke *et al.* [51] and Hou *et al.* [52] to be observed in two-dimensional quantum hall systems connected to a superconductor.

Chapter 3

Device fabrication methods and measurement set-up

While the first measurements on graphene were conducted with Si/SiO_2 as the substrate [14, 63–65, 75], results obtained from these devices were inferior to what was expected from the peculiar band structure of graphene [10]. The reason was the influence of the underlying SiO_2 layer on the electronic properties of graphene. While graphene is a flat two-dimensional (2D) material, the underlying SiO_2 layer is usually disordered and rough. Graphene on a Si/SiO_2 substrate suffers in terms of electronic transport due to the charge puddles and charge traps which could be present in the substrate or at the graphene/substrate interface [66, 76, 77]. Suspended graphene devices [74, 78–80] and graphene on boron nitride devices [16, 17, 19, 34, 81] are shown to have significant improvement in its electronic transport properties. Amongst the two techniques, the substrate supported devices are comparatively easier to fabricate. This technique also allows extensive freedom on the device architecture which is relatively difficult to achieve in the suspended graphene devices. h-BN serves as a perfect substrate for the substrate supported graphene devices due to its perfectly flat 2D nature with a mere 1.7% lattice mismatch between the graphene and h-BN crystal lattices [81].

The other limitation in the early graphene based devices were the 2D on-top electrical contacts which suffered from the poor bonding between the metal contacts and graphene [82]. Graphene has strong in-plane σ-bonds while the out-of-plane bonding is the weak π-bonding. This makes the on-top metal contacts to have weak coupling with graphene which results in poor graphene/metal contacts. Another important point of consideration is the contamination of graphene due to the chemicals and polymers used during the fabrication processes. Both of these detrimental factors were addressed by using the h-BN encapsulated graphene devices with one-dimensional metallic contact on the edge of the graphene [34]. This led to the fabrication and measurement of high quality graphene devices with high charge carrier mobility and ballistic transport [16, 17, 34]. It was

also found that under certain conditions, h-BN can modify the electronic and optical properties of graphene such as the appearance of the moiré pattern, Hofstadter butterfly and Brown-Zak oscillations due to the formation of graphene/h-BN superlattice, and tunable polariton modes due to the hybridization between the polaritons in graphene and h-BN [83].

All of the above stated factors make h-BN encapsulated graphene an ideal system to study and modify the electronic transport properties of graphene. Therefore, the building block of the graphene based devices studied under the scope of this thesis, are the h-BN/graphene/h-BN heterostructures with 1D edge contacts.

3.1 Fabrication of the h-BN/graphene/h-BN van der Waals heterostructures

Preparation of the h-BN/graphene/h-BN heterostructures can be crudely divided into two main parts. One is the exfoliation of graphene and h-BN crystals from their thicker parent material, and the other is assembling these crystals in a certain order. Since these crystals are kept together by the van der Waals forces acting between the surfaces of the constituting material layers, these heterostructures are commonly known as the van der Waals heterostructures [84]. In the present section, fabrication of these h-BN encapsulated graphene heterostructures is discussed.

3.1.1 Exfoliation and identification of single layer graphene

Natural graphite crystals (commercially available from NGS Naturgraphit GmbH) and h-BN powder (commercially available from Momentive, product PT110), were used as the sources for graphene and h-BN crystals, respectively. Single layer graphene and multilayer h-BN crystals were exfoliated from their parent crystals by using the traditional micromechanical cleavage method [63, 64]. In this method, a relatively thicker crystal is thinned down by peeling it repeatedly with the scotch tape strips. After the crystal is thinned down to making a weak shadow on the tape, the tape is pressed with slight force against a pre-cleaned substrate and then, removed gently from the substrate. Due to the weak forces between the substrate and the crystals on the tape, some part of the crystals are transferred on to the substrate. This substrate is then checked for the presence of exfoliated graphene or h-BN crystals.

Since graphene is highly transparent (2.3% absorption in the visible spectrum), the choice of substrate plays an important role in the exfoliation process. Graphene is clearly visible on a Si/SiO_2 substrate with 300 nm thick SiO_2, and hence, it was chosen as the substrate (1 x 1 cm^2 substrate) for the exfoliation process. The substrate was cleaned with acetone and isopropanol first (to remove any adsorbates/dirt), then ultrasonicated for 2

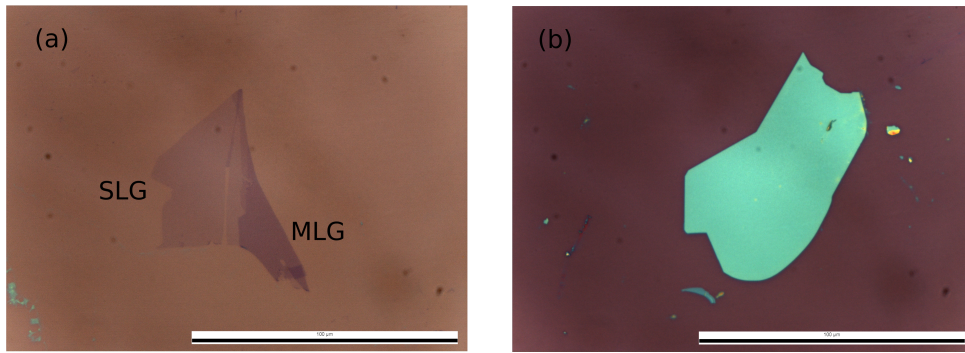

Figure 3.1: Optical image of exfoliated (a) single layer graphene (SLG) and multilayer graphene (MLG), and (b) h-BN crystal. Scalebar is 100 μm.

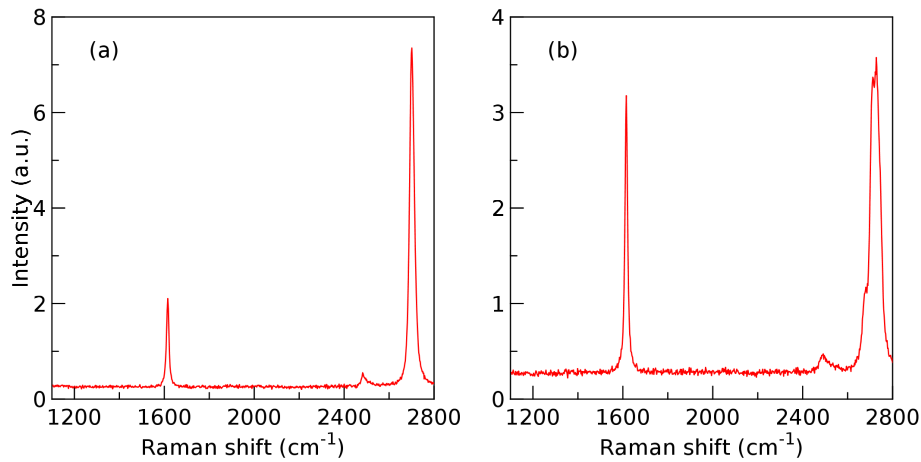

Figure 3.2: Raman spectrum of (a) single layer graphene on a Si/SiO_2 substrate, and (b) bilayer graphene on a Si/SiO_2 substrate.

min. It was followed by an oxygen plasma cleaning to remove any remaining contaminant. This substrate is then used for the exfoliation of graphene or h-BN.

After the exfoliation, the substrate is viewed under an optical microscope. Fig. 3.1(a) shows the exfoliated single layer and multilayer graphene on the substrate. h-BN crystals are exfoliated in the same way as graphene, however, the h-BN crystals are chosen with respect to their thickness. In this work, the chosen top or bottom h-BN crystals were 15 - 30 nm thick as measured with an atomic force microscope after the fabrication of the van der Waals heterostructures. Fig. 3.1(b) shows an h-BN crystal which was found to be $\sim$28 nm thick.

The h-BN crystals which are to be used in the van der Waals heterostructures, were selected just with the contrast from the optical microscope. The graphene layer is chosen after making an additional test which is to measure a Raman spectrum to verify the single

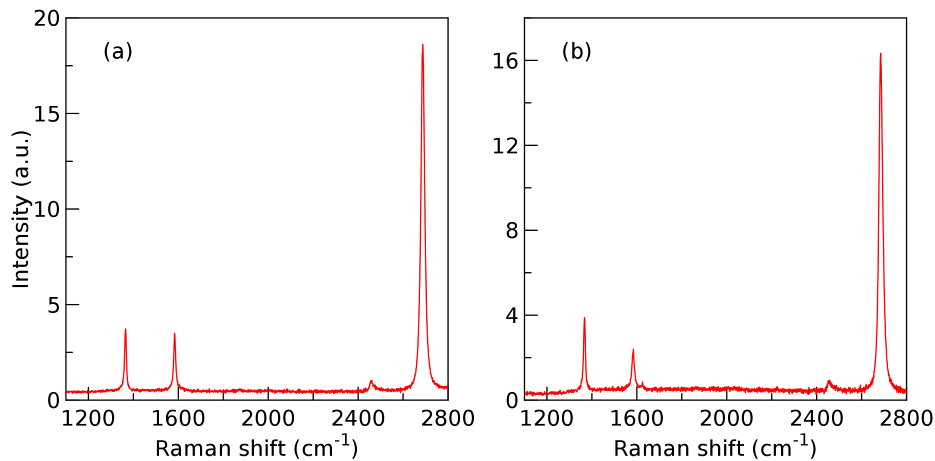

Figure 3.3: Raman spectrum of h-BN encapsulated graphene on a Si/SiO_2 substrate in (a) h-BN/graphene/h-BN heterostructure used for two-terminal NGS devices, and (b) h-BN/graphene/h-BN heterostructure used for multiterminal NGS devices.

layer graphene. Raman spectrometry is a non-invasive, reliable characterisation technique to obtain information about the vibrational energy levels of a material. Due to its non-invasiveness, it is highly suitable for graphene based devices where the contamination of graphene is detrimental for the electronic transport. Since single layer and bilayer graphene (BLG) have different phonon band structures, the difference between the two can be directly seen in their Raman spectrum [85–87]. Due to this factor, Raman spectrometry is a strong tool to characterise graphene in terms of layer thickness as well. In this work, Renishaw Raman microscope was used to characterise the exfoliated graphene with an incident laser wavelength of 532 nm. Fig. 3.2(a) and (b) show the Raman spectrum of SLG and BLG, respectively, on a Si/SiO_2 substrate. The first Raman peak appearing close to 1600 cm^{-1} corresponds to the G-band phonon process which is a direct first order Raman process. The other prominent peak is the G′ peak close to 2700 cm^{-1} which corresponds to the second order double resonance Raman scattering process. Note that the D peak (appears close to 1350 cm^{-1} in the disordered graphene systems) is missing in these spectra indicating defect free graphene layers. Comparing the two spectra shown in Fig. 3.2(a) and (b), a clear distinction can be made by observing: (i) the relative intensity of the G′ and G peak $I_{G'}/I_G$, and (ii) the shape of the G′ peak. In case of SLG, $I_{G'}/I_G \approx 4$ while it is ≈ 1 in case of BLG. In addition, the G′ peak is a collection of four peaks (four Raman processes) in case of BLG, hence the peculiar shape, while in SLG, G′ is only one single peak due to one Raman process.

Fig. 3.3(a) and (b) show the Raman spectrum of h-BN encapsulated graphene in two different van der Waals heterostructures. The fabrication process of these heterostructures will be discussed in the next subsection. The effect of the substrate induced effects in

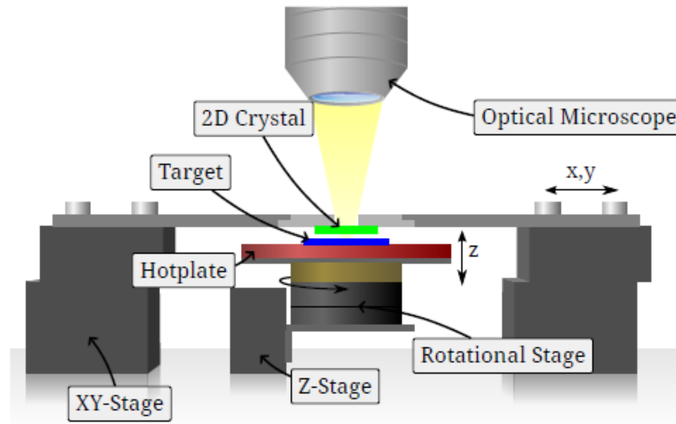

Figure 3.4: Illustration of the alignment setup used for the fabrication of van der Waals heterostructures [89].

graphene samples can be clearly seen by comparing Fig. 3.2(a) (graphene on a Si/SiO$_2$ substrate) with Fig. 3.3(a) and (b) (h-BN encapsulated graphene). The G-peak can now be observed close to 1580 cm^{-1} with a higher $I_{G'}/I_G$ ratio. In addition, the full-width at half-maximum (FWHM) of the G′ peak, which is a measure of the disorder [87], reduces from 22 cm^{-1} for the SLG on Si/SiO$_2$ substrate as shown in Fig. 3.2(a) to 19 cm^{-1} for the same SLG in the van der Waals heterostructure as shown in Fig. 3.3(a). The FWHM of the G′ peak of the encapsulated SLG shown in Fig. 3.3(b) is 18 cm^{-1}. The additional peak that appears close to 1380 cm^{-1} belongs to the Raman mode of the h-BN crystallite [88]. Note that these are the same heterostructures that were later used for the fabrication of the two-terminal and multiterminal graphene devices which will be discussed in the successive chapters.

3.1.2 Fabrication of the van der Waals heterostructures

After selecting the suitable graphene and h-BN crystals, the next step is to fabricate a heterostructure using these crystals. The fabrication of the graphene/h-BN van der Waals heterostructures was carried out by using the dry transfer technique [25, 34]. In this technique, the graphene layer does not come in contact with any polymer or any other chemical during the entire transfer process, *i. e.*, the transfer of the top h-BN on graphene, and later, the transfer of these two on the bottom h-BN.

In order to pick-up and transfer the crystals, a long working distance microscope was used along with a movable stage with horizontal ($xy-$movement) and vertical ($z-$movement) adjustments. This setup allows to align the crystals during the pick-up and transfer process to obtain the desired stacking of the h-BN/graphene/h-BN heterostructure. The schematic of the setup has been shown in Fig. 3.4. As can be seen, in this figure, the target chip is placed on the hotplate while the stamp which is marked

as "2D crystal" in the Fig. 3.4, (with/without the 2D crystal) stays above the target. The in-plane position of the target and the stamp relative to one-another can be adjusted by the $xy-$screws of the stage. Usually, the target chip is either glued or clamped with screws onto the hotplate. The position of the stamp is set by screwing the metallic frame (which contains the stamp) in such a way that the crystals are roughly aligned in the $xy-$plane with respect to each other. The $xy-$micrometer adjustment screws can, then, be used to get a fine adjustment by moving only the top part of the alignment setup which holds the metallic frame relative to the target. After the in-plane adjustment is good enough for the stacking of the crystals, the target and the stamp are brought in contact by using the $z-$ screw which raises the hotplate. Fine tuning of the $xy-$ adjustment is usually required during this process to ensure perfectly aligned stacking of the crystals in order to cover maximum graphene area with the top and bottom h-BN. The hotplate is employed to heat the target after the target and the stamp are in contact to ensure better adhesion between the crystals.

For preparing the van der Waals heterostructures with the dry transfer method, first of all, a poly-dimethyl-siloxane (PDMS) stamp supported by a thin glass substrate is spin coated with poly-propyl-carbonate (PPC), PPC 10 wt% in ethyl-acetate. The PDMS stamp has a central circular knob with the height of 0.5 mm and diameter of 1.5 mm which helps to restrict the area of the sample that comes in contact with the PPC. This helps in selectively picking the desired h-BN or graphene with lesser number of surrounding h-BN or graphite crystals. The PPC-coated PDMS stamp is then glued to a metallic transfer frame by using polymethyl methacrylate (PMMA). The frame has a central wide opening to provide the optical view of the transfer process, and the PDMS stamp is glued in a way to keep the circular knob in this wide opening. The metallic frame containing the PPC-coated PDMS stamp is then baked in an oven under ambient atmosphere at 80°C for 15 min. After the baking, the PPC film around the central knob is carefully removed under the microscope by using a scalpel and leaving the PPC film only on the central knob. This is the stamp which is used for the stacking of the crystals. Note that some of the heterostructures were prepared by using the method employed by Kraft *et al.* [25]. In this method, the PPC film is spin-coated on the substrate containing the top h-BN crystal. This PPC-coated substrate is then baked in the oven at 80°C for 15 min to cure the PPC. The h-BN crystals on the substrate stick to the PPC-film and this PPC-film is picked-up by the PDMS stamp. This PDMS stamp which contains the top h-BN is used for stacking top h-BN/graphene, and subsequently top h-BN/graphene/bottom h-BN.

The process flow of the fabrication of the van der Waals heterostructure is as shown in Fig. 3.5. The top h-BN (lying on the hotplate shown in Fig. 3.4) is brought in contact with the PPC-coated PDMS stamp using the $z-$screw. The substrate is heated to 60°C in this position. At this temperature, the PPC softens and sticks to the substrate. With the help of the $z-$ screw, the hotplate is lowered immediately. Due to the softening, the PPC leaves the PDMS stamp and sticks onto the substrate. The substrate is, then,

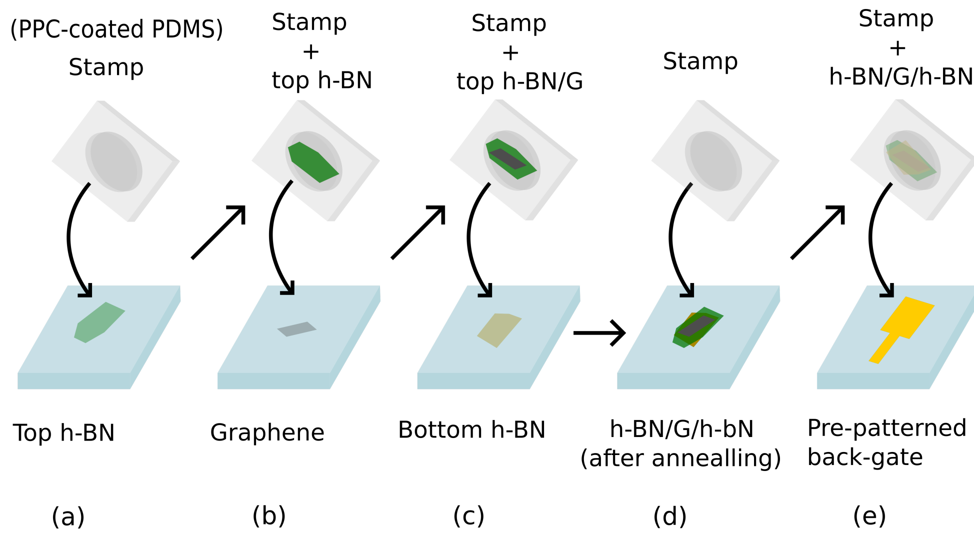

Figure 3.5: Illustration of the van der Waals assembly process.

allowed to cool to room temperature which solidifies the softened PPC. In this process, the h-BN crystal sticks to the PPC. This solidified PPC is then picked by the central knob of the same PDMS stamp by making use of the adhesive forces between the two polymers.

Now, the stamp contains the top h-BN crystal and the target substrate is the substrate containing the selected graphene layer. Both, the substrate and the stamp, are now aligned with respect to each other as explained before. The top h-BN and graphene are brought in contact where the top h-BN is dropped on the graphene layer by softening the PPC as before. The van der Waals forces between the top h-BN and graphene ensure that the graphene sticks to the h-BN crystal and leaves the substrate. After the PPC is solidified the top h-BN/graphene stack, which is now sticking to the PPC film, is picked by the PDMS stamp.

The process of aligning the crystals and dropping the PPC is repeated for stacking the top h-BN/graphene on the bottom h-BN. However, in this step, the PPC is dissolved in acetone after it solidifies on the substrate. This leaves the h-BN/graphene/h-BN heterostructure on the Si/SiO_2 substrate. This substrate is rinsed with acetone and isopropanol to remove the residues of the polymer. Note that during the entire process of encapsulation, the graphene layer remains untouched by the polymer. After this, the heterostructures are annealed in an oven under ambient atmosphere at 300°C for 3 hours. This annealing process helps in achieving clean h-BN/graphene interfaces by squeezing out the dirt or contaminants that are trapped between the crystals. These contaminants form isolated pockets at high temperature and leave sufficient clean area in the h-BN/graphene/h-BN heterostructure which is used for the device fabrication. After the annealing, if required, the heterostructure can be picked up again by using a

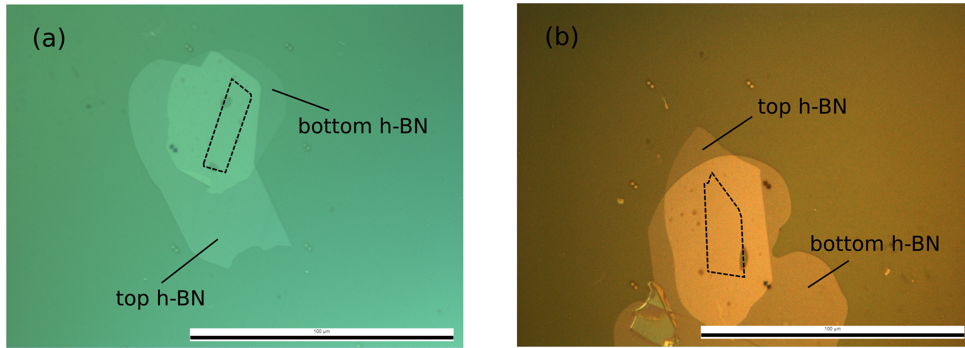

Figure 3.6: (a) and (b) Optical images of two h-BN/graphene/h-BN heterostructures after the van der Waals assembly. Region enclosed by the dotted black lines roughly marks the h-BN encapsulated graphene. Scalebar is 100 μm.

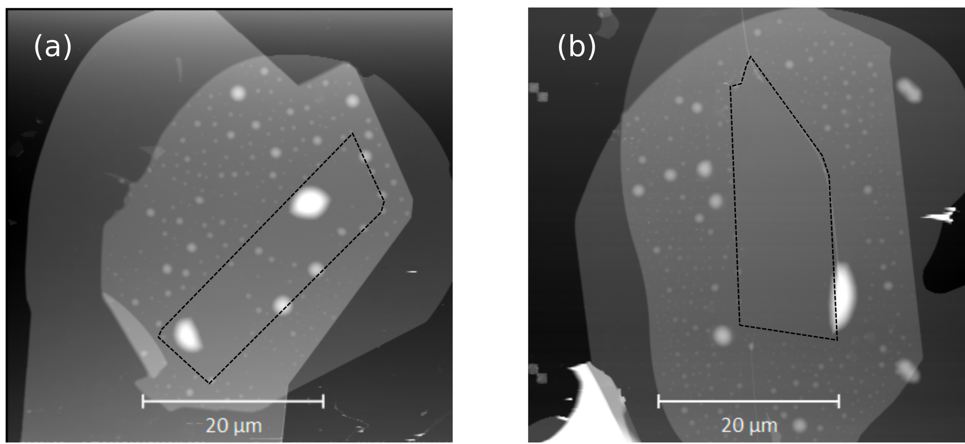

Figure 3.7: (a) and (b) AFM images of two h-BN/graphene/h-BN heterostructures after the van der Waals assembly as shown in Fig. 3.6. Region enclosed by the dotted black lines marks the h-BN encapsulated graphene.

PPC-coated PDMS with a fresh PPC film and transferred to another substrate.

In Fig. 3.6(a) and (b), optical images of two h-BN/graphene/h-BN heterostructures are shown after the annealing process, followed by their transfer onto a Si/SiO_2 substrate with 1000 nm thick SiO_2 layer. The difference in the colour between the two images is due to the optical filter. The dirt pockets that form after the annealing can be vaguely seen in these images. However, to fabricate the devices, it is essential to know if the graphene/h-BN interfaces are clean, which is difficult to conclude from the optical images. Therefore, an atomic force microscopy (AFM) image of the h-BN/graphene/h-BN heterostructure is captured as shown in Fig. 3.7(a) and (b) which correspond to the heterostructure shown in Fig. 3.6(a) and (b), respectively. The region marked with the dotted black lines shows the h-BN encapsulated graphene. It can be seen that in the dotted region, there is sufficiently large area which is perfectly flat and free from the dirt pockets. This clean

h-BN encapsulated graphene area is later used for the fabrication of the devices.

3.2 Fabrication of graphene devices with hybrid contacts

The number of devices that can be fabricated on a single chip using a single h-BN/graphene/h-BN heterostructure is limited only by the size of the clean graphene region, and later by the size of the chip itself. After selecting a suitable h-BN/graphene/h-BN heterostructure with a large enough graphene region which is free from the trapped contaminants (the requirements for the clean graphene region will vary from device to device), the next step is to fabricate the devices from this heterostructure.

3.2.1 Basic fabrication processes

The devices studied under the scope of this thesis employ two different contact materials, one for the superconducting electrode(s) and the other for the normal metal electrode(s). The process flow for the device fabrication is a little different from the one followed in the early report on the edge-connected graphene devices [34], while individual fabrication processes are similar to the ones shown by Kraft *et al.* [25]. Two different types of devices (two-terminal and multiterminal devices) are fabricated and measured, as will be shown in the successive chapters. The fabrication process for both type of the devices is identical. For the sake of clarity, the device fabrication process can be divided into two important parts as given below:

1. **Fabrication of the electrodes**

   Fig. 3.8 shows the illustration of the electrode fabrication process. First, poly (methyl methacrylate) (PMMA), used as the positive electron beam resist, is spin coated on the 1 x 0.5 cm^2 Si/SiO_2 chip containing the h-BN/graphene/h-BN heterostructure. The usual thickness of the PMMA 950K (4.5% in anisole) after spin-coating at 6000 rpm for 90 s is $\sim$280 nm. The PMMA-coated chip is baked in an oven under ambient atmosphere at 160°C for 30 min. This chip is then loaded into the electron beam lithography (EBL) setup (eLine from Raith was used for the devices reported here). The desired pattern is defined on the chip using EBL at an acceleration voltage of 30 kV. The defined pattern is then developed using a solution of methyl-isobutyl-ketone (MIBK) and isopropanol (IPA) (MIBK:IPA ratio of 1:3) for 15 - 18 s and rinsed with IPA for 10 s afterwards. Following the development of the pattern, the chip is transferred to the reactive ion etching (RIE) chamber after checking the developed pattern under the optical microscope or measuring an AFM map in case of a very fine pattern. RIE is employed to access the edge of the encapsulated graphene layer by etching through the h-BN/graphene/h-BN stack

in the selected region (defined by the developed pattern) using a combination of 40 sccm CHF_3 and 15 sccm O_2 at 60 mTorr chamber pressure and 60 W RF power. The etching time is calculated from a calibrated etching rate to have an etching depth slightly more than the thickness of the top h-BN. It is to make sure that the edge of the graphene layer is exposed for making a metallic contact after the etching process. Immediately after the etching process, the chip is transferred to the metal evaporation setup where the electrode material for the contact is evaporated. Multiple metals can be evaporated one after the other to obtain the desired material combination in a single metallisation step. The metal deposition is carried out in an ultra high vacuum metal evaporator setup (pressure is of the order of 10^{-9} mbar during the deposition process) at low temperature (sample is cooled to -120°C using the liquid nitrogen cooling of the sample holder). After allowing the chip to come to the room temperature, the last step in the contact electrode fabrication process is the lift-off of the undesired excess metal. It is done by keeping the chip in acetone for 3 - 4 hours which usually provides a clean lift-off. After this, the chip is rinsed gently with acetone followed by IPA to remove any remaining chemical residues.

It is to be noted that the fabrication process for gate electrodes is similar to the contact electrodes except the etching of the heterostructure using RIE. In case of the gate electrode fabrication, the metal deposition is carried out immediately after the development of the pattern.

2. **Etching of the mesa and defining the device geometry**

   This is a fabrication process which separates the devices form each other as well as from the surrounding graphene region to avoid any shorts between the devices or electrodes. This process is identical to the etching process discussed in the above fabrication step where a combination of CHF_3 and O_2 is used to etch a pattern defined using EBL. After the etching process is complete, the chip is rinsed with acetone to remove the PMMA layer. It is followed by rinsing with IPA to remove the chemical residues.

3.2.2 Process flow for graphene based junctions with hybrid contacts

Using the above two processes in a certain order, the graphene devices with normal metal and superconducting electrodes can be fabricated reliably according to the process flow described below.

1. **Fabrication of the superconducting electrodes**

   In these devices, a combination of Ti/Al is used to serve as the superconducting electrodes. This material combination is also quite immune to any damage from the

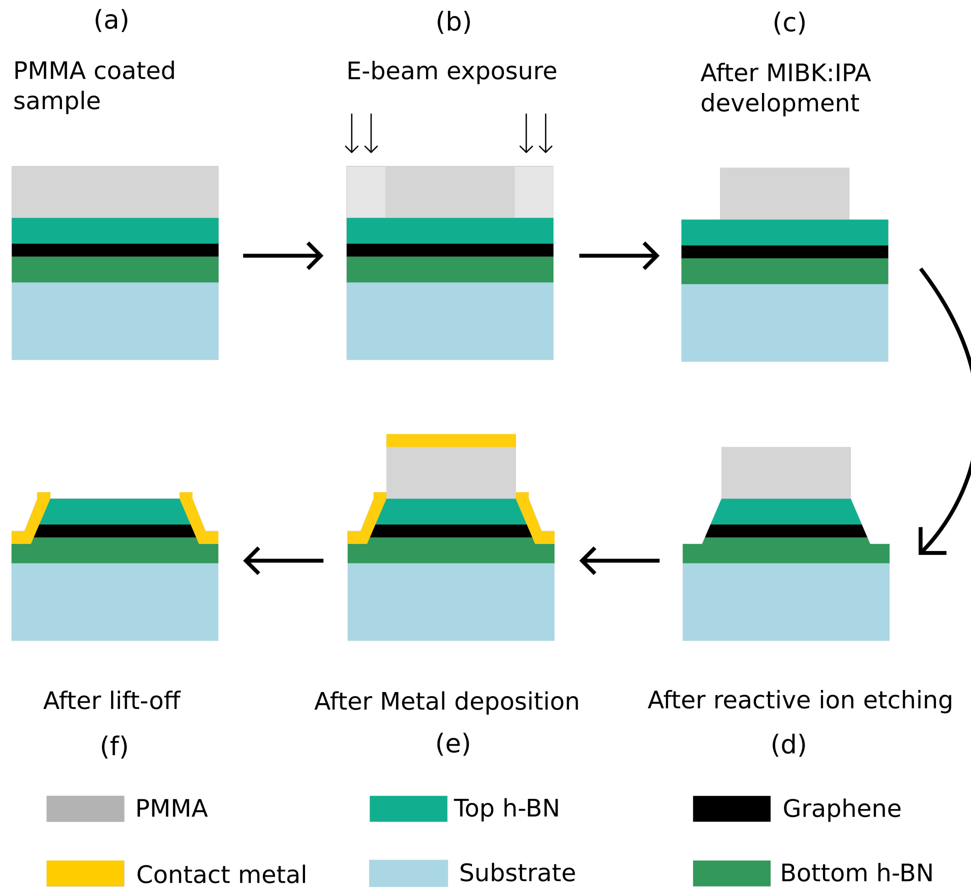

Figure 3.8: Illustration of the electrode fabrication process.

subsequent lithography steps due to the formation of a thin natural aluminium oxide (Al_2O_3) layer on the surface. Therefore, this is the first step in the device fabrication process. After using EBL and RIE to pattern the electrodes, superconducting electrodes in the present step, first a thin layer of Ti (5 nm) was deposited which acts as an adhesive layer to make contact with graphene. It is followed by the deposition of a thicker Al layer (60 - 70 nm), thereby establishing the superconducting Ti/Al electrodes. The usual deposition rate for Ti and Al are usually $\sim$0.5 nm/min and 6 - 7 nm/min, respectively.

2. **Defining the device geometry**

In the devices fabricated under this study, the normal metal is a combination of Ti/Cu/Al. Since Cu is highly reactive to PMMA, any fabrication step with the exposed Cu metal cannot be followed by the coating of the PMMA layer. Therefore, the etching step, defining the device geometry and separating the devices from the surroundings, was performed before the deposition of the normal metal electrode. However, in order to keep the contact between the graphene and the normal metal free from the polymer contamination, the etching was done in a manner to leave

some predefined unetched regions where the normal metal contacts will be defined in the subsequent step.

3. **Fabrication of the normal electrodes**

   The normal metal electrodes are deposited using the same protocol as the superconducting electrodes. At first, the electrodes are defined using the EBL and RIE. It is to be noted that in this step, the region left unetched for the formation of the normal electrodes in the previous etching step, is precisely the region that is patterned, developed and etched. After the RIE process, a thin Ti layer (5 nm), which is the adhesive layer, is deposited. It is followed by the deposition of the normal metal which in this case, is a thick Cu layer (70 - 80 nm). Since Cu is very sensitive to oxidation, a 5 nm thick Al layer was deposited which acts as a capping layer. This capping layer forms a natural Al_2O_3 layer as the chip is exposed to the ambient conditions. This Al_2O_3 capping then protects the underlying Cu layer from the environment.

4. **Atomic layer deposition of the gate dielectric**

   The graphene devices discussed here were fabricated on Si/SiO_2 substrates with a 300 nm thick SiO_2 in case of the two-terminal NGS junctions, and with a 1000 nm thick SiO_2 in case of the multiterminal junctions. The substrates with the thicker SiO_2 layer were chosen for the devices fabricated after the two-terminal NGS junctions in order to avoid the breaking of the SiO_2 layer during the wire bonding of the devices. Since the SiO_2 layers are quite thick, very high voltages are required if the underlying Si substrate is desired to be used as the gate electrode. Taking this into account, a top gate electrode with a thinner gate dielectric was preferred which will tune the graphene sheet more efficiently compared to the Si back gate. It is to be noted that in a h-BN/graphene/h-BN heterostructure, h-BN always acts as a gate dielectric. However, to tune the device homogeneously, the gate electrode would need to cover the entire graphene region between the contact electrodes. This brings the need to have an additional gate dielectric layer to avoid shorts between the gate electrode and the contact electrodes. Therefore, an Al_2O_3 layer with a thickness of $\sim$25 nm was deposited using the atomic layer deposition (ALD) in case of both, the two-terminal and the multiterminal, devices. The precursors used for this process were trimethylaluminium (TMA) and water (H_2O) where the reaction temperature/sample temperature was $\sim$110°C. Atomic layer deposition ensures a conformal growth of the Al_2O_3 layer which is required to provide insulation between the gate electrodes and the contact electrodes.

5. **Fabrication of the gate electrodes**

   The final step in the device fabrication process is the fabrication of the gate electrodes. The fabrication protocol is similar to the contact electrodes without

the etching step. The gate electrode is patterned and developed, and the substrate is transferred to the evaporation chamber for the metallisation process. Here, gate electrodes with Ti/Cu/Al material combination were used which were metallised in the same way as the normal metal electrodes with thin Ti and Al layers serving as the adhesive and capping layers, respectively. It is to be noted that the gate electrode is required to cover the entire device area. Therefore, an overlap between the contact electrodes and the gate electrode is necessary. In the devices fabricated and studied here, the thickness of the Cu layer was 80 - 100 nm with the Ti and the Al layer being 5 nm each.

This entire process flow is shown in Fig. 3.9(a)-(d) as an example with the help of the AFM images. Fig. 3.9(a) shows the h-BN/graphene/h-BN stack shown in Fig. 3.7(a) after the fabrication of the superconducting Ti/Al electrodes. It denotes step 1 of the process flow. Fig. 3.9(b) shows the device geometry defined by the etching process corresponding to step 2. The region enclosed by the white dashed lines roughly shows the area where the encapsulated graphene was before the etching process. Note that some of the region in the h-BN/graphene/h-BN region is left unetched apart from the defined device area itself. This marks the region of the normal metal contact electrodes and contact leads that will be defined in step 3. These normal metal electrodes and leads can be clearly seen to reside in the marked region by comparing Fig. 3.9(b) and (c) where the latter corresponds to step 3 of the fabrication process. Step 4 in the process flow, where the Al_2O_3 layer is deposited using the ALD process, has not been shown in Fig. 3.9 as the Al_2O_3 layer grows conformally over the entire chip. Therefore, it does not change the topography of the device as measured with the AFM. Fig. 3.9(d) corresponds to the fabrication step 5 where individual top gate electrodes are defined. The gate electrodes can be clearly seen by comparing Fig. 3.9(c) and (d).

3.3 Measurement set-up

All of the fabricated devices were characterised by using the low temperature electronic characterisation methods. Most of the measurements were performed in an Oxford He^3/He^4 dilution refrigerator (wet dilution refrigerator), while some of the measurements were performed in a Bluefors He^3/He^4 dilution refrigerator (dry dilution refrigerator). In both of the cases, the devices were first wire bonded to a sample holder with an Al alloy (Al/Si with 1% Si) bond wire. The devices were then cooled down to ~ 4 K to study the normal state electronic transport in the devices. Note that the superconductor used in these devices is Ti/Al with a superconducting critical temperature T_C of ~ 1 K. Therefore, the normal state electronic transport in these devices shows the effect of two different electrode materials on the electronic transport in graphene. In some of the cases, the normal state measurement was made below T_C with an applied perpendicular

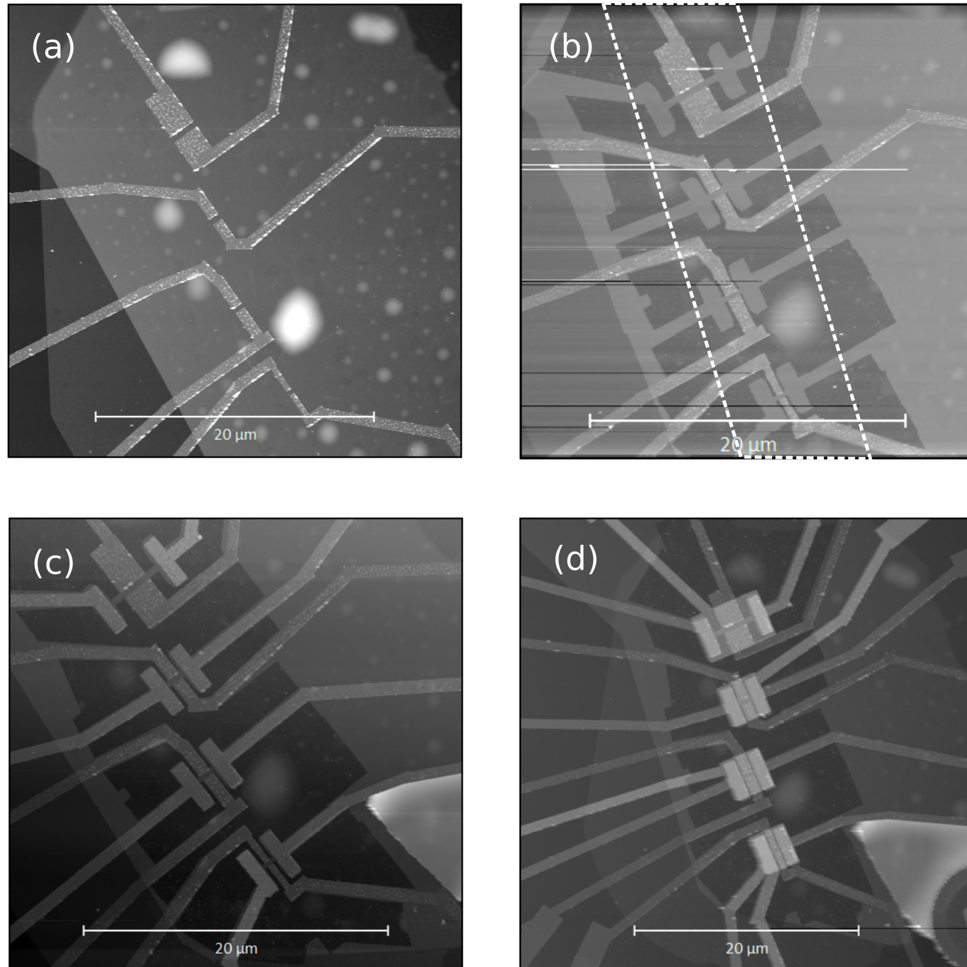

Figure 3.9: Process flow of the encapsulated graphene based device fabrication with hybrid contacts as shown using the AFM images. (a) Superconducting (Ti/Al) electrodes defined with the help of EBL, RIE and subsequent metallisation. (b) Device geometry defined by EBL and subsequent RIE. Note that the region that is left unetched in the shape of electrodes, marks the region where the normal electrodes will be defined later. (c) Normal electrodes (Ti/Cu/Al) defined with EBL, RIE and metallisation. This process is followed by the deposition of an additional gate dielectric layer (top h-BN is already present as the gate dielectric) to avoid forming shorts between the contact electrodes and the gate electrode. (d) Individual gate electrodes defined for each of the device using EBL, RIE and metallisation. The straight horizontal lines in (b) and (d) are due to the artifacts induced by the AFM tip during the measurement.

magnetic field $B \gg B_C$, where $B_C < 15\,\mathrm{mT}$ is the critical magnetic field as observed in the measured devices. For characterisation in the superconducting state, the devices were measured in the base temperature range of 20 - 50 mK, except the temperature dependent measurements. The temperature dependent measurements were conducted in a higher temperature range, however, always below a base temperature of 800 mK, *i. e.*, below the T_C of the measured devices, hence, preserving the superconductivity.

All of the measurements were performed by using standard low frequency (7 - 138 Hz) lock-in detection technique with a small ac excitation (2 - 50 μV). The devices were always measured in a pseudo four-probe geometry in case of two terminal devices. In case of multiterminal devices, most of the measurements were performed in a pseudo four-probe geometry, however, some of the measurements were performed in a pseudo three-probe geometry due to the limited number of connections available on the sample holder. In case of dc-bias dependent measurements conducted in the Oxford dilution refrigerator, bias voltage was supplied by using a home-made battery operated voltage divider circuit set by a motor-controlled potentiometer. For the measurements performed in the Bluefors dilution refrigerator, dc-bias voltage was supplied by using an Itest ultra low noise power supply unit. In both of the cases, the differential conductance/resistance was determined by using two different lock-in amplifiers for detecting the potential drop across the device and current through the device. dc component of the current/voltage was measured with the dc preamplifiers and read with the standard digital multimeters.

Chapter **4**

Andreev reflection in ballistic two terminal normal metal/graphene/superconductor junctions

In this chapter, the focus is on the experimental study of the two-terminal graphene based junctions in normal metal/graphene/superconductor (NGS) geometry. In the normal state, *i. e.*, in NGN′ (N′ denotes the normal state of the superconductor) configuration, such a system provides an opportunity to study the effect of asymmetric contacts on the charge transport in graphene. In the superconducting state, owing to the gate tunability of graphene, the NGS system serves as a perfect platform to study the properties of tunable normal metal/superconductor junctions. It is to be noted that there is a single superconducting interface in these NGS junctions as opposed to the widely studied graphene based Josephson junctions where the primary focus is on a large supercurrent and multiple Andreev reflections [16, 17, 19, 21, 23, 24]. Andreev reflection processes in these NGS junctions are explained with a modified Octavio-Tinkham-Blonder-Klapwijk (OTBK) model [3, 4, 35, 36] which takes into account the asymmetry of the contacts. This chapter is based on the results published in reference [90].

4.1 Device geometry

In these devices, single layer graphene is encapsulated between two h-BN crystals which are 16 and 20 nm thick for the top and bottom BN crystal, respectively. The encapsulated graphene is then edge-contacted by the normal metal on one of its edges and by the superconductor on the other parallel edge. For the superconducting contact, Ti/Al (5 and 70 nm, respectively) has been used, while for the normal metal contact, Ti/Cu/Al

(5, 70 and 5 nm, respectively) has been used. In both of the contacts, Ti serves as an adhesive layer while Al in the normal metal contact serves as a capping layer to protect Cu from oxidation. To tune the charge carrier density in graphene, overall top-gates using Ti/Cu/Al (5, 80 and 5 nm, respectively) were fabricated for individual devices. In addition to the top h-BN, a 25 nm thick Al_2O_3 layer (by atomic layer deposition) serves as the gate dielectric. Details on the device fabrication have been provided in the previous chapter, **Chapter 3**. Fig. 4.1 shows the device schematics and atomic force microscope (AFM) image of the measured devices. Geometrical dimensions of the measured devices are width W (along the graphene/metal interface) = 6 μm, length L (length of the graphene channel between the two contact metals) = 0.25 μm, and W = 5 μm, L = 0.45 μm for devices A and B, respectively. Most of the data presented in this thesis is obtained from device A unless stated otherwise.

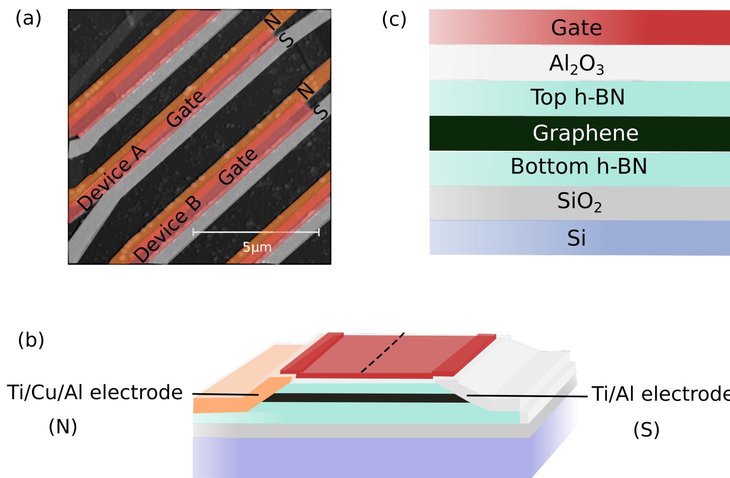

Figure 4.1: (a) AFM image of the measured devices. (b) Device schematics. (c) cross-section of the device across the line segment shown in (b).

4.2 Normal state characterisation

The normal state characterisation of any graphene device relies on its gate dependent conductance curve. Fig. 4.2 shows the gate voltage V_g dependent resistance and conductance of device A measured at T = 4.2 K. The charge carrier density n was estimated from the Shubnikov de Haas measurements as a function of V_g. (Details of the method are shown in the next subsection). As can be readily seen in Fig. 4.2, the charge neutrality point (CNP) is shifted to a negative V_g indicating n-type doping of the graphene channel. In addition, the device exhibits higher resistance in the hole-doped regime as compared to the electron-doped regime suggesting a stronger potential barrier for charge transport in the hole doped regime. Both of these features can be explained by considering the metal contact induced doping of graphene due to the difference in the work function of

graphene and the contact metal [82, 91, 92]. On one hand, this charge transfer process shifts the CNP and on the other hand, it creates a potential barrier for charge transport in the hole-doped regime which results in the formation of pn junctions in the vicinity of the graphene/metal interfaces. It is also to be noted that the two different electrode materials used to contact graphene in these devices might also play a role in the charge transport asymmetry observed in Fig. 4.2.

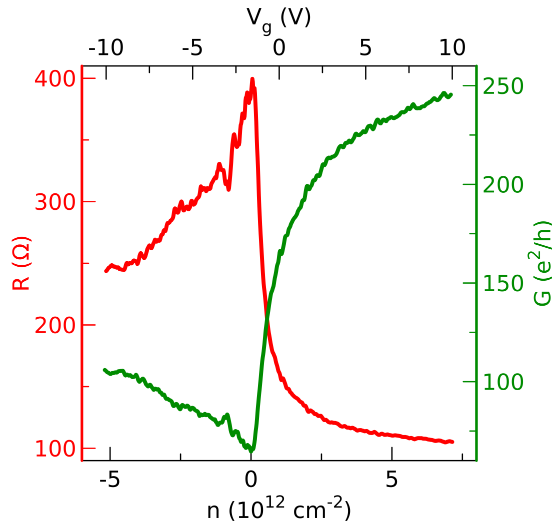

Figure 4.2: Resistance R and conductance G of device A at $T = 4.2$ K as a function of the charge carrier density n and gate voltage V_{g}.

4.2.1 Estimation of the charge carrier density

Using a parallel plate capacitor model in graphene/gate dielectric/gate electrode formation, the charge carrier density n can be defined as

$$n = \frac{C_{\mathrm{g}} V_{\mathrm{g}}}{Ae} = \alpha\, V_{\mathrm{g}} \tag{4.1}$$

where C_{g} is the gate capacitance, A is the effective gate area and α is the gate coupling efficiency. It is clear that knowing the value of C_{g}, the charge carrier density can be easily calculated. However, it is to be noted that in these devices, there are two different gate dielectric layers, the top h-BN and Al_2O_3 where the dielectric constant changes at low temperatures. Therefore, it is difficult to calculate the correct value of C_{g} from the dielectric constant values available in the literature.

In such cases, a more precise estimation of the charge carrier density can be achieved by using the Shubnikov de Haas oscillation measurements. In the presence of a perpendicular magnetic field, the charge carriers experience a Lorentz force which bends the charge

carrier trajectories and results in the cyclotron orbits with radius $r_C = (\hbar k)/eB$. In case of a 2D system, if r_C becomes smaller than the device dimensions, no charge transport takes place through the bulk of the device as the charge carriers can now complete their cyclotron orbits without being scattered. In this state, the charge transport takes place through the edge modes. At high magnetic field, the energy levels in the system become quantized into discrete Landau levels and the current is carried only by the edge modes through skipping orbits whenever the Fermi level lies between the two Landau levels. This effect, known as the quantum Hall effect (QHE), can be observed by increasing the magnetic field strength to achieve the Landau quantization. As the charge transport in a device enters the quantum Hall regime, the longitudinal resistance/conductance of the device shows oscillations with increasing charge carrier density as the subsequent Landau levels are filled, and resistance/conductance minima between two consecutive Landau levels. This quantization can also be observed in the transverse conductance of the device with respect to the charge carrier density [65, 93, 94]. As edge transport takes place when the Fermi level lies between two Landau levels, it results in a series of conductance plateaus in the transverse conductance of the device whenever a Landau level is filled. In the quantum Hall regime, the relation between the magnetic field B and n is defined as

$$\nu = \frac{nh}{eB} \tag{4.2}$$

where ν is the Landau level filling factor or Landau level index. The energy levels in single layer graphene are four-fold degenerate due to the spin and valley degeneracy. The lowest Landau level appears at $\nu = 2$ due to the spin degeneracy while the successive levels appear at $\nu = 6, 10, 14, 18....$ accounting for the spin and valley degeneracy. From eqn. 4.1 and 4.2, we have

$$\nu = \frac{\alpha V_g h}{eB} \tag{4.3}$$

where α remains the only unknown quantity.

In Fig. 4.3(a), the dependence of the device conductance on varying the applied gate voltage $\delta V_g = V_g - V_{CNP}$ (which accounts for the shift of the CNP as seen in Fig. 4.2) and B is shown, commonly known as the Landau fan diagram. The conductance $G = dI/dV$ of the device is differentiated with respect to V_g in order to enhance the visibility of the conductance oscillations. While the Fabry-Pérot resonances (discussed in the next subsection) due to the formation of the pn-junctions can be very well observed at the low magnetic fields in the p-doped regime, the Landau fan is relatively weaker here as compared to the n-doped regime because of these pn-junctions [95, 96]. From eqn. 4.3, it is clear that in a V_g vs B plot for transverse conductance in the quantum Hall regime, a linear fit can be made depending only on ν and α for the conductance plateaus. Since ν can only take predefined values as discussed above, such linear fits give a near-perfect approximation of α which can then be used to calculate n in a precise way. Fig. 4.3(b)

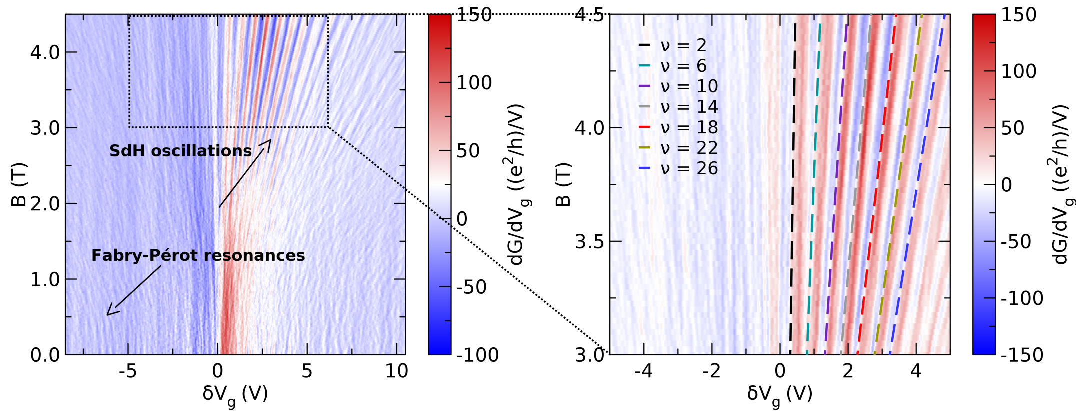

Figure 4.3: (a) Magnetic field dependence of conductance differentiated with respect to the gate voltage at $T = 4.2$ K. (b) Zoomed-in region of (a) showing the linear fit used to obtain the gate coupling efficiency α by using the Landau level filling factor ν

shows a zoomed-in section of Fig. 4.3(a) where the zero of the differentiated conductance shows the conductance plateaus. The evolution of these plateaus is followed with linear fits for various ν with an average α of the order of 6.14 x $10^{11}\,\mathrm{V^{-1}cm^{-2}}$. This value of α was used to calculate n by substituting it in eqn. 4.1 and $\delta V_{\mathrm{g}} = V_{\mathrm{g}} - V_{\mathrm{CNP}}$ was used instead of V_{g}.

4.3 Ballistic transport

In this section, the results obtained from the bias spectroscopy and the magnetic field dependent measurements are presented when the device is in the NGN′ configuration. It will be shown that the graphene/metal interface asymmetry can be observed easily in the ballistic regime where the difference in transmission through the two interfaces modifies the signature of ballistic charge transport in graphene.

4.3.1 Effect of the asymmetric contacts on the energy dependent interference

As discussed in section 4.2, due to the n-type doping from the metal contacts to the graphene sheet, pn-junctions are created in the vicinity of the graphene/metal interface when the Fermi level of graphene lies in the valence band. The two pn-junctions formed at the two graphene/metal interfaces result in the formation of an electronic npn cavity where the pn-junctions act as partially transmitting interfaces. This phenomenon is analogous to an optical Fabry-Pérot (FP) cavity where the pn-junctions play the role of partially transmitting mirrors in the FP cavity. In this electronic cavity, the charge carriers travel back and forth in the cavity by getting reflected from the pn-junctions

in the vicinity of the graphene/metal interfaces before they are transmitted. If the cavity length is smaller than the mean free path of the charge carriers, *i. e.*, the charge transport in the cavity is in the ballistic regime, then multiply reflected charge carrier trajectories result in a conductance/resistance interference pattern. This interference pattern can be seen as the oscillations in the conductance/resistance of the device due to the constructive/destructive interference of the charge carrier trajectories. Constructive interference of the trajectories results in the conductance maxima according to the relation:

$$2L_{\mathrm{C}}\cos\theta = N\lambda_{\mathrm{F}} \tag{4.4}$$

where L_{C} is the cavity length, θ is the angle of incidence, λ_{F} is the Fermi wavelength and $N \in \mathbb{N}$. In the simplest case where $\theta = 0$, *i. e.*, normal incidence, it is clear that the interference pattern can be tuned by tuning the Fermi wavelength. Simplifying eqn. 4.4 in this case results in the following relation:

$$k_{\mathrm{F}}L_{\mathrm{C}} = N\pi \tag{4.5}$$

where k_{F} is the Fermi wavevector defined as:

$$k_{\mathrm{F}} = \frac{2\pi}{\lambda_{\mathrm{F}}} = \sqrt{\pi\, n} = \sqrt{\pi\,\alpha\,|V_{\mathrm{g}} - V_{\mathrm{CNP}}|} \tag{4.6}$$

In agreement to the relation in eqn. 4.6, the FP resonances can be seen in the p-doped regime in Fig.4.2 as oscillations in the conductance/resistance with changing V_{g}. It clearly indicates that the charge transport in this device is in the ballistic regime. Another way of tuning the FP resonances is by applying a bias voltage across the device. It leads to a change in the energy of the charge carriers as $\delta E = eV_{\mathrm{bias}}/2$ where V_{bias} is the applied bias voltage. Due to the linear relation between E and k in the low-energy regime, this modifies k as per the relation $\delta k = eV_{\mathrm{bias}}/(2\hbar v_{\mathrm{F}})$ where v_{F} is the Fermi velocity. Therefore, a well-accepted way of characterizing the ballistic transport in graphene-based devices is to map the FP resonances as a function of V_{g} and V_{bias} [75, 97, 98]. Using the resonance condition shown in eqn. 4.5 and substituting the value of k_{F} and δk, a simple equation can be derived for the FP resonance pattern:

$$V_{\mathrm{bias}} = \pm(2\hbar v_{\mathrm{F}}\sqrt{\pi\,\alpha}/e)\sqrt{|V_{\mathrm{g}} - V_{\mathrm{CNP}}|} + N\,\frac{2\pi\,\hbar\, v_{\mathrm{F}}}{eL} \tag{4.7}$$

According to eqn. 4.7, a checkerboard conductance/resistance pattern is usually observed for graphene devices [75, 97, 98].

In Fig. 4.7(a), the energy dependence of the FP resonances is shown with respect to the variation in V_{g} and V_{bias}. As the conductance profile of the device varies strongly with V_{g} and V_{bias}, a non-oscillating background was subtracted from the data to enhance the visibility of the oscillatory conductance G_{OSC}. It can be clearly seen that the interference pattern observed here is stripe-like instead of the usual checkerboard pattern. This

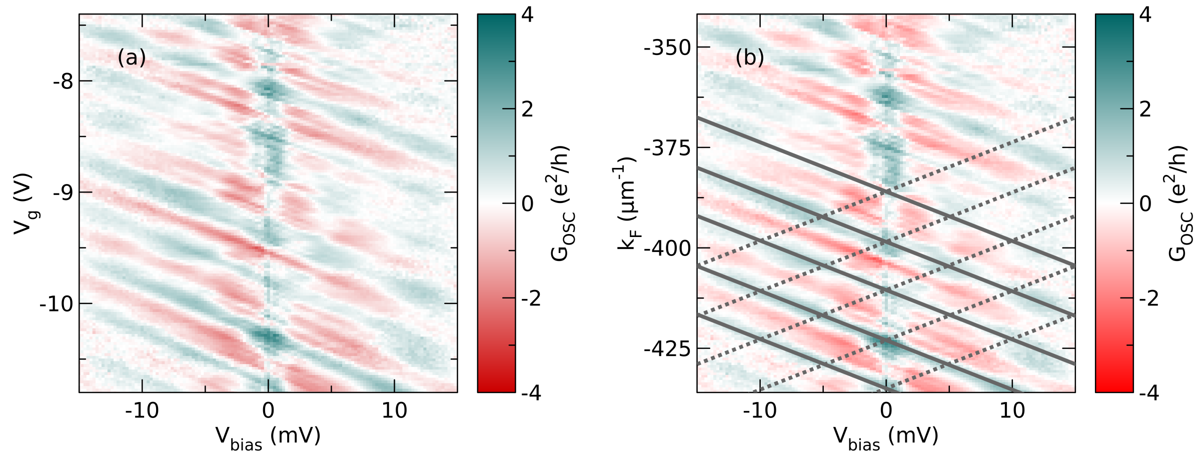

Figure 4.4: (a) Modulation of the FP resonances with varying V_g and V_{bias} at $T = 100\,\text{mK}$ and $B = 50\,\text{mT}$. (b) Linear fit of the conductance resonances shown in (a) according to eqn. 4.7 where solid fits show the observed resonances and dotted fits show the missing symmetry of the resonance spectrum.

asymmetric interference pattern indicates the asymmetry of the two graphene/metal contact interfaces which is expected from this device as the two contact electrodes are made of different metals. Similar asymmetry in the FP interference pattern was observed in carbon nanotube (CNT) based devices with energy dependent transmission coefficients [99]. Linear fits of the conductance resonances as per eqn. 4.7 are shown in Fig. 4.4(b) where k_F is calculated by using eqn. 4.6. These linear fits have two fitting parameters in accordance with eqn. 4.7, namely α defining the slope of the fits and L_C defining the intercept. Using the value of α obtained from the SdH oscillations as described in section 4.2.1, the value of L_C is found to be $240 \pm 5\,\text{nm}$ which is in agreement with the length of the measured device. It is clear that while the charge transport in this device is in the ballistic regime, the asymmetry of the contact interfaces is clearly reflected in the FP interference pattern.

4.3.2 Quantum interference in the magnetic field

As discussed earlier in section 4.2.1, at high magnetic fields, the energy levels in a 2D system are quantized into discrete Landau levels. However, at smaller magnetic fields, the energy levels are continuous. In this regime, the Lorentz force acting on the charge carriers bends their electronic trajectory which changes the angle of incidence at the transmitting interface. Due to the angular dependent transmission in graphene [10, 68], this leads to an interesting phenomenon known as the Klein tunnelling as discussed in **Chapter 2**. In this tunnelling process, the charge carriers with normal incidence or close to the normal incidence are transmitted with a transmission probability close to

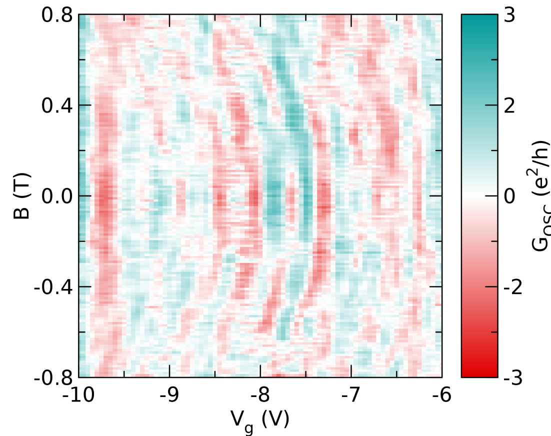

Figure 4.5: G_{OSC} as a function of the gate voltage V_{g} and perpendicular magnetic field B in the normal state at 4.2 K

unity while the transmission at other incidence angles is suppressed. Due to this angle dependence of the transmission, the FP resonances can be tuned by a perpendicular magnetic field before the charge transport enters into the quantum Hall regime. Fig. 4.5 shows the tuning of the FP resonances by small magnetic fields where the parabolic dispersion of the interference pattern comes from the Aharonov-Bohm phase. As the applied magnetic field increases, the charge carrier trajectories in the FP-cavity bend to an extent that they enclose the origin in the graphene band structure. This adds a non-trivial Berry phase of π to these trajectories, thereby modifying the angle dependence of the transmission through the cavity which serves as a proof of the Klein tunnelling [69]. This effect is seen as a π-phase shift of the conductance oscillation at a certain magnetic field which is weakly visible in Fig. 4.5. It is to be noted that this magnetic field dependence was measured in a different cool-down of the device. It accounts for the slight change in the position of the conductance maxima/minima with respect to the data observed in Fig. 4.4(a).

4.4 Superconductivity in hybrid graphene based junctions

In the previous sections, the measurements were carried out in the NGN′ configuration. The results obtained from these measurements show the impact on the charge transport in 2-terminal graphene based junctions when the two contact electrodes are made of different metals. In the present section, the measurement results were obtained after the superconducting electrode was cooled below its superconducting transition temperature. It results in the device configuration NGS which implies that the two metal/graphene interfaces have completely different transport properties. The experimental results obtained in

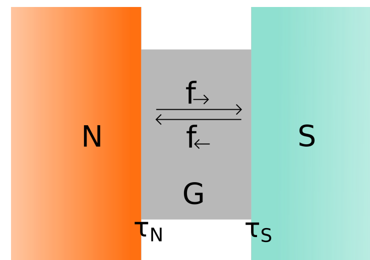

Figure 4.6: Modelling schematic for an NGS junction (See text for description).

this configuration are explained by using a modified Octavio-Tinkham-Blonder-Klapwijk (OTBK) model [4, 35, 36]. A brief description of the model is provided in the next subsection followed by the experimental results.

4.4.1 Analytical Model

Credit note: This model was developed by Prof. Detlef Beckmann (Supervisor of this thesis). It is provided in the current thesis for completeness.

In order to address the transport through two different interfaces in the NGS devices, the system is modelled in the superconducting state by using a modified OTBK model [4, 35, 36]. As shown in Fig. 4.6, the graphene sheet is modelled as an ideal conductor which connects a normal metal (N) electrode (left terminal) and a superconductor (S) electrode (right terminal). This configuration implies that due to a single superconducting interface in the system, multiple Andreev reflections cannot take place. The two interfaces have normal-state transmission probabilities τ_{N} and τ_{S}, respectively. These two different transmission probabilities account for the different material interfaces and the formation of pn junctions in the p-doped region. The normal metal terminal is at the electrochemical potential $\mu = -eV$ while the superconducting terminal is at an electrochemical potential $\mu = 0$. The current through the device can be calculated by using the right- and left-moving distribution functions, $f_{\rightarrow}(\epsilon)$ and $f_{\leftarrow}(\epsilon)$, respectively, from the boundary conditions provided below:

$$\begin{aligned} f_{\rightarrow}(\epsilon) &= \tau_{\mathrm{N}} f_0(\epsilon-\mu) + r_{\mathrm{N}} f_{\leftarrow}(\epsilon), \\ f_{\leftarrow}(\epsilon) &= T(\epsilon) f_0(\epsilon) + R(\epsilon) f_{\rightarrow}(\epsilon) + A(\epsilon)\left(1 - f_{\rightarrow}(-\epsilon)\right), \end{aligned} \tag{4.8}$$

where f_0 is the Fermi function, ϵ is the energy, $r_{\mathrm{N}} = 1 - \tau_{\mathrm{N}}$ is the reflection probability at the normal metal terminal, and $T(\epsilon)$, $R(\epsilon)$ and $A(\epsilon)$ denote the normal transmission, normal reflection and Andreev reflection probabilities, respectively, at the superconducting terminal.

From the analytical solution of the equation system 4.8, the current through the device can be calculated by integrating the difference between the distribution functions,

$f_{\rightarrow}(\epsilon) - f_{\leftarrow}(\epsilon)$, over energy. The differential conductance dI/dV can be calculated from the current as shown below.

$$\frac{dI}{dV} = G_{\mathrm{N}} \int g(\epsilon) \left(-\frac{\partial f_0(\epsilon + eV)}{\partial eV} \right) d\epsilon \tag{4.9}$$

Here, G_{N} is the normal-state conductance, and $g(\epsilon)$ is the normalized spectral conductance which is given as

$$g(\epsilon) = \frac{1}{\tau^*} \frac{\tau_{\mathrm{N}}(A^2(\epsilon) r_{\mathrm{N}} - (R(\epsilon) - 1)(R(\epsilon) r_{\mathrm{N}} - 1) - A(\epsilon)\tau_{\mathrm{N}})}{(A^2(\epsilon) r_{\mathrm{N}}^2 - (R(\epsilon) r_{\mathrm{N}} - 1)^2)} \tag{4.10}$$

where $\tau^* = \tau_{\mathrm{S}}\tau_{\mathrm{N}}/(1 - r_{\mathrm{S}} r_{\mathrm{N}})$ gives the effective transmission probability in the normal state.

Contrary to the original OTBK model where $T(\epsilon), R(\epsilon)$ and $A(\epsilon)$ are calculated with the BTK model [3], a generalized BTK model [35, 36] is used here. The BTK model describes ballistic microconstrictions between a BCS superconductor and a normal metal [100], while the generalized BTK model takes into account the magnetic pair-breaking in an applied magnetic field, and its effect on the spectral conductance in the superconducting state. Using this model, $A(\epsilon)$ and $R(\epsilon)$ can be calculated as

$$A(\epsilon) = \tau_{\mathrm{S}}^2 \left| \frac{\hat{f}(\epsilon)}{D(\epsilon)} \right|^2, \tag{4.11}$$

$$R(\epsilon) = \frac{4 r_{\mathrm{S}}}{|D(\epsilon)|^2}, \tag{4.12}$$

Here $D(\epsilon) = (1 + r_{\mathrm{S}}) + (1 - r_{\mathrm{S}})\hat{g}(\epsilon)$, and $\hat{g}(\epsilon)$ and $\hat{f}(\epsilon)$ are the normal and anomalous Green's functions of the superconductor, respectively. The Green's functions are determined by using the normalization condition $\hat{g}^2(\epsilon) + \hat{f}^2(\epsilon) = 1$ along with the Usadel equation, which in this case is defined as [36]

$$\epsilon \hat{f}(\epsilon) + i\alpha \hat{g}(\epsilon)\hat{f}(\epsilon) - i\Delta \hat{g}(\epsilon) = 0, \tag{4.13}$$

Here α is the magnetic depairing energy which accounts for the magnetic pair-breaking effects [101], and Δ is the superconducting order parameter. In the absence of the magnetic depairing, *i. e.*, $\alpha = 0$, $A(\epsilon)$ and $R(\epsilon)$ take the form of the analytical BTK expressions [3].

In summary, the fitting parameters required to fit the experimentally obtained conductance spectrum are the normal state conductance G_{N}, the transmission probabilities

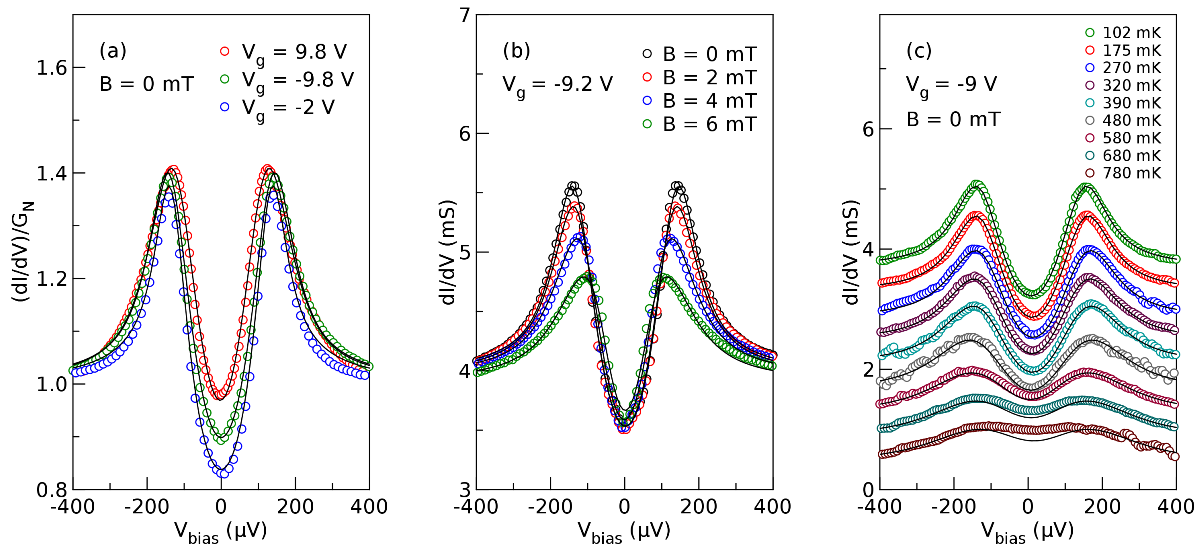

Figure 4.7: Differential conductance dI/dV measured as a function of the applied bias voltage V_{bias} for: (a) applied gate voltage V_{g} at $T \sim 20\,\text{mK}$ corresponding to the electron-doped region ($V_{\text{g}} = 9.8\,\text{V}$), the hole-doped region ($V_{\text{g}} = -9.8\,\text{V}$), and close to the charge neutrality point ($V_{\text{g}} = -2\,\text{V}$). Note that the dI/dV has been normalized with the normal state conductance G_{N} (as obtained from the measurement at T 4.2 K). (b) various values of magnetic field B applied perpendicular to the device at $T \sim 20\,\text{mK}$ and $V_{\text{g}} = -9.2\,\text{V}$ corresponding to the hole-doped region. (c) different temperatures at $V_{\text{g}} = -9\,\text{V}$, *i. e.*,in the hole-doped region. In all of the panels, the experimental data is represented by the symbols while the solid curves represent the fit of the data with the modified OTBK model.

τ_{S} and τ_{N}, the superconducting order parameter Δ, the magnetic depairing energy α, and the effective electronic temperature T. Note that T enters through the Fermi function f_0.

4.4.2 Experimental results and discussion

As the superconducting electrode is made of Ti/Al, a superconducting critical temperature $T_{\text{C}} \sim 990\,\text{mK}$ was observed for the NGS devices. In order to understand the superconductivity in these hybrid junction devices, a systematic experimental study of the conductance spectra was performed as a function of the gate voltage V_{g}, magnetic field B and temperature T. Results obtained from these measurements are shown in Fig. 4.7 for device A. Fig. 4.7(a) shows the evolution of the differential conductance dI/dV normalized with the normal state conductance G_{N} (from the measurement at $T \sim 4.2\,\text{K}$) as a function of the bias voltage V_{bias} at $B = 0$ and $T \sim 20\,\text{mK}$ in three different charge transport regimes, where $V_{\text{g}} = 9.8$, -9.8 and -2 V corresponds to the n-doped region, the p-doped region and close to the CNP, respectively. The non-zero conductance observed in the subgap regime is due to the Andreev reflections which

indicates a metallic junction behaviour. The experimental data shown here was fitted by using the modified OTBK model and a change in the superconducting gap Δ from $\sim 127\mu$eV in the n-doped region to $\sim$144 μeV in the p-doped region was observed. The fitting parameters extracted from the modified OTBK fits of the data are shown in Table 4.1. Since the measurements were conducted at the zero magnetic field, it implies $\alpha = 0$. The change in Δ from the p-doped region to the n-doped region can be clearly seen as a shift in the position of the maxima of dI/dV as shown in Fig. 4.7(a). Two arguments can be presented to address the difference in Δ, first, the device has a higher conductance in the n-doped region compared to the p-doped region as can be seen in Fig. 4.2. This could lead to the self-heating of the device at high charge carrier densities in the n-doped region which would result in the reduction of Δ. Second, a gate-dependent voltage division between the normal metal lead and graphene could also appear as a change in Δ.

V_g (V)	Δ (μeV)	τ_N	τ_S	T (mK)
9.8 (n-doped)	127	0.92	0.7	354
-9.8 (p-doped)	144	0.73	0.69	270
-2 (close to the CNP)	140	0.59	0.67	190

Table 4.1: The superconducting order parameter Δ, transmission probabilities τ_N and τ_S, and the effective electronic temperature T as extracted from the fit of the conductance spectra shown in Fig. 4.7(a)

Fig. 4.7(b) shows the evolution of dI/dV and Δ in a perpendicular magnetic field B in the hole-doped regime at V_g = -9.2 V and T $\sim$20 mK. The magnetic field was kept below the critical magnetic field in order to preserve superconductivity in the device. This series of measurement also serves as an additional test for the applicability of the modified OTBK model in explaining the experimental data. Increasing B from 0 to 6 mT results in a clear decrease of Δ as can be seen in the successive curves in Fig. 4.7(b). By fitting the data with the modified OTBK model, a decrease in Δ from $\sim$143 μeV at 0 mT to $\sim$125 μeV at 6 mT was observed. As the model takes into account the pair-breaking

B (mT)	Δ (μeV)	α (Δ)
0	143	0
2	143	0.03
4	136	0.09
6	125	0.18

Table 4.2: The superconducting order parameter Δ and the magnetic depairing energy α as extracted from the fit of the conductance spectra shown in Fig. 4.7(b). The effective electronic temperature T was 265 mK and the transmission probabilities τ_N and τ_S were 0.73 and 0.69, respectively, for all of the fits.

Fig. 4.7	V_g (V)	τ_N	τ_S
(a)	9.8	0.922 ± 0.01	0.697 ± 0.002
(a)	-9.8	0.729 ± 0.008	0.694 ± 0.003
(a)	-2	0.589 ± 0.006	0.667 ± 0.002
(b)	-9.2	0.73 ± 0.017	0.692 ± 0.004
(c)	-9	0.743 ± 0.023	0.675 ± 0.006

Table 4.3: Transmission probabilities τ_N and τ_S as extracted from the fits shown in Fig. 4.7(a), (b) and (c).

effect in an applied magnetic field [101, 102], the magnetic depairing energy was found to increase from 0 to ∼0.18Δ with the increasing magnetic field. The change in Δ and α as a function of B is shown in Table 4.2 as extracted from the fits of the data.

After considering the effect of electrostatic doping, *i. e.*, V_g dependence, and B dependence, temperature is another important parameter to characterise the evolution of superconductivity. Increasing temperature results in the weakening of superconductivity which can be seen in Fig. 4.7(c) as the decrease in Δ with the increase in T. These measurements were performed in the p-doped region at V_g = -9 V under zero magnetic field ($B = 0$ implies $\alpha = 0$), with T ranging from ∼102 mK to 780 mK. The curves are shifted downwards in successive steps of 0.4 mS for the sake of clarity. This temperature dependence of the differential conductance can be very-well described by the modified OTBK model where a decrease in Δ from ∼144 μeV to ∼119 μeV is observed as the temperature is increased from ∼102 mK to 780 mK. While the series is well captured by the model in the low temperature regime, it is not very-well fitted as the temperature approaches to T_C. It indicates the limitation of the model with respect to T close to T_C.

As has been pointed out in section 4.3.1 and 4.4.1, the two different graphene/metal interfaces, *i. e.*, the normal metal/graphene and graphene/superconductor interfaces, influence the charge transport through graphene. This difference between the two interfaces is accounted by considering their respective transmission probabilities. Table 4.3 shows the transmission probabilities as extracted from the fits of the data shown in Fig. 4.7(a), (b) and (c) with respect to the applied gate voltage V_g. In Fig. 4.8(a), the transmission probabilities τ_N and τ_S for the normal metal/graphene and graphene/superconductor interfaces, respectively, are shown for device A and B as extracted from the OTBK fits of the experimental data. It is to be noted that the data was collected in a select gate voltage range for device A with high resolution in the gate voltage step-size while the data for device B was collected over a large gate voltage range with comparatively lower resolution in the gate voltage step-size. Therefore, the fine details of the electronic transport can be traced with the data collected from the measurements on device A, while an overall trend of the charge transport can be obtained from device B to compare

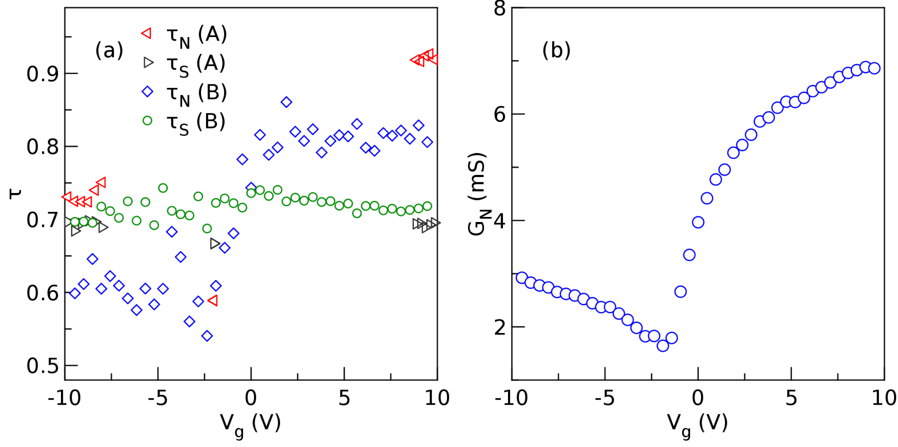

Figure 4.8: (a) Transmission probabilities $\tau_{\rm N}$ and $\tau_{\rm S}$, respectively for device A and B. (b) Normal state conductance $G_{\rm N}$ as a function of the gate voltage $V_{\rm g}$ in device B. All of the parameters, $\tau_{\rm N}$, $\tau_{\rm S}$ and $G_{\rm N}$, are extracted from the fitting of the differential conductance data by using the modified OTBK model. The measurements were done at a base temperature of 20 mK and $B = 0$ T.

it with device A.

For device A, $\tau_{\rm N}$ varies from 0.74 in the p-doped region to 0.92 in the n-doped region while it drops to 0.59 close to the CNP. $\tau_{\rm S}$, on the other hand, remains fairly constant by varying between 0.67 to 0.71 for this entire $V_{\rm g}$ range. The comparatively low value of $\tau_{\rm S}$ in terms of the metallic junction indicates a weak barrier at the graphene/superconductor interface which could be present due to lithographic imperfections. Comparing the values of $\tau_{\rm N}$ and $\tau_{\rm S}$ for device B with device A, it is clear that the normal metal/graphene interface in device B is comparatively lesser transparent than device A. However, the dependence of $\tau_{\rm N}$ and $\tau_{\rm S}$ on $V_{\rm g}$ is similar in both of the devices. It is worth noting that this dependence of doping is clearly visible in the subgap conductance as shown in Fig. 4.7(a). In addition, the difference between $\tau_{\rm N}$ and $\tau_{\rm S}$ confirms and explains the observed asymmetry of the FP interfernce pattern as shown in Fig. 4.4(a). In Fig. 4.8(b), the normal state conductance $G_{\rm N}$ is shown for device B which was extracted from the same OTBK fits that were used to extract $\tau_{\rm N}$ and $\tau_{\rm S}$ as shown in Fig. 4.8(a). A large difference between the conductance in the n-doped region and the p-doped region can be clearly seen as well as the shift of CNP to the negative $V_{\rm g}$ due to the n-doping of graphene from the contact electrodes as discussed in section 4.2. It indicates that the modified OTBK model used for fitting can qualitatively explain the experimental data in the entire gate voltage range.

In order to understand the correlation between the transmission probabilities $\tau_{\rm N}$ and $\tau_{\rm S}$, and the normal state conductance $G_{\rm N}$, a series of conductance spectra was

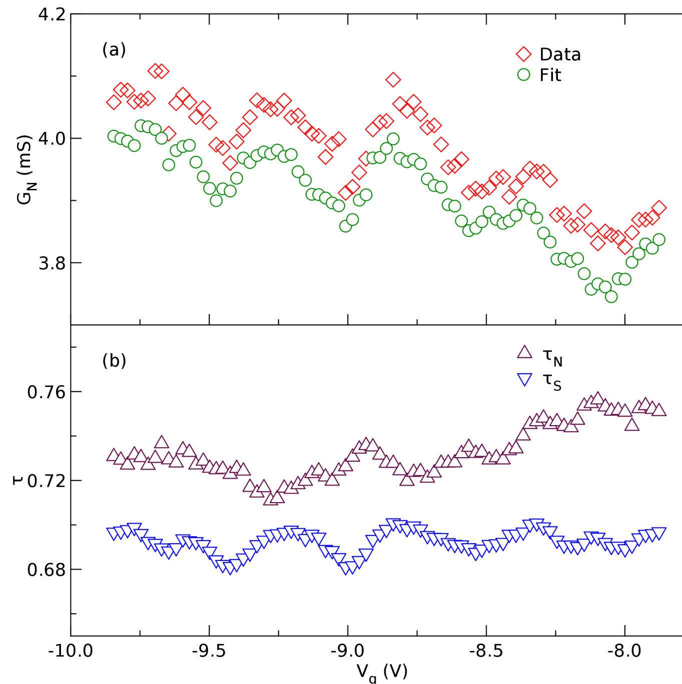

Figure 4.9: (a) Oscillations in G_{N} as a function of the gate voltage V_{g} in the hole-doped region (data) as observed at a base temperature of 20 mK and $B = 0$ T, and fitting value of G_{N} for the conductance as extracted from the OTBK fits of the experimental data (fit). (b) Transmission probability τ (showing τ_{N} and τ_{S}) as obtained from the OTBK fits of the same experimental data.

measured with varying V_{g} in the p-doped region in device A at $B = 0$ T and $T \sim$20 mK. Fig. 4.9(a) shows the measured G_{N} as well as the extracted G_{N} (from the OTBK fits of the experimental data) as a function of V_{g}. It can be clearly seen that the FP resonances, as observed in Fig. 4.2, are visible in the extracted value of G_{N} as well. Fig. 4.9(b) shows the transmission probabilities extracted from the same OTBK fits and the same V_{g} dependent oscillation pattern can be seen in the transmission probabilities, most precisely in τ_{S}. It indicates that the transmission through the interfaces in the NGS configuration is tuned by V_{g} in a similar way as it was tuned in case of the FP resonances. Using eqn. 4.5 from section 4.3.1 to calculate the cavity length L_{C} from these oscillations, $L_{\mathrm{C}} \sim$236±10 nm is obtained. It shows that the oscillations observed here are indeed due to the FP interference of the Andreev reflected charge carriers. In case of graphene based Josephson junctions, the signatures of FP interferences can be observed in the superconducting state as the oscillation in the critical current [16–19, 23, 25] or multiple Andreev reflections [21]. However, the results shown here clearly indicate that the FP resonances, which show ballistic transport in these hybrid junctions, can be traced in the transmission probabilities of the device interfaces as the charge carriers are Andreev reflected.

4.5 Conclusion

To conclude, it has been shown that the charge transport through graphene is significantly tuned by the graphene metal/interfaces. In case of a ballistic device, it can be observed as the asymmetry in the Fabry-Pérot interference pattern which results from the difference in the transmission through the two graphene/metal interfaces. In the superconducting state, the modified OTBK model provides a qualitative explanation of the charge transport through the normal metal/graphene/superconductor (NGS) junctions by accounting for two different transmission probabilities for the normal metal/graphene and graphene/superconductor interfaces. In addition, the signature of Fabry-Pérot resonances in the superconducting state can be observed in these hybrid junctions by following the transmission probabilities through the two graphene/metal interfaces.

Chapter **5**

Tuning the supercurrent in multiterminal graphene based Josephson junctions

In this chapter, the electronic transport in multiterminal graphene based devices is discussed. These devices have a Josephson junction where graphene acts as a weak link between two superconductors, and a normal junction where graphene acts as a narrow channel between two normal metal electrodes. This device geometry results in two transverse graphene based junctions, namely the superconductor/graphene/superconductor (SGS) junction and the normal metal/graphene/normal metal (NGN) junction.

It was observed in case of a diffusive metallic weak link based Josephson junction that the supercurrent through a Josephson junction can be controlled via a normal transverse current [103, 104]. This normal transverse current changes the occupation of the Andreev levels in the weak link. The current-phase relation of the Josephson junction in such a case can be modified from $I = I_\mathrm{c}\sin(\phi)$ to $I = I_\mathrm{c}\sin(\phi + \pi)$. These junctions, known as the π-junctions due to the modified current phase relation, provide control on the magnitude as well as the direction of the supercurrent by modifying the phase of the Josephson junction. In a similar direction, control and manipulation of the supercurrent in ballistic Josephson junctions with two-dimensional electron gas (2DEG) systems was also observed [105–107]. With a similar analogy, the electronic transport through the SGS junction can be modified by applying a potential difference or passing a current across the NGN junction and vice versa, as was shown in case of graphene based diffusive Josephson junctions [108].

This chapter deals with the experimental results obtained from these multiterminal devices with the primary focus on the control and manipulation of the supercurrent in the SGS junction by passing a control current through the transverse NGN junction.

5.1 Device geometry

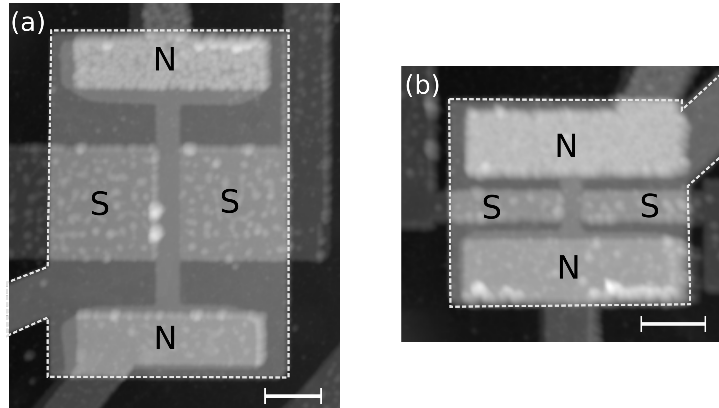

Figure 5.1: Atomic force microscopy image of (a) device A and (b) device B. Scale bar is 1 μm in both of the panels. N and S show the normal and superconducting electrodes, respectively. In both of the devices, the region enclosed with the white dashed lines shows the overall top gate electrode and the narrow channel connecting the four electrodes shows the h-BN encapsulated graphene. In (a), the channel is 4 μm long between N-N and 0.46 μm between S-S while the contact region between S and graphene is 2 μm wide. In (b), the channel is 1 μm long between N-N, 0.36 μm between S-S and the S-graphene contact region is 0.47 μm wide.

In order to fabricate these devices, single layer graphene was encapsulated between two h-BN crystals with the top h-BN being $\sim$ 28 nm thick and the bottom h-BN being $\sim$ 18 nm thick. Graphene was then edge-connected to two superconducting electrodes on its two parallel edges where the superconducting electrodes were made of Ti/Al (5 and 60 nm, respectively). The other two transverse edges of the graphene were then connected to two normal metal electrodes made of Ti/Cu/Al (5, 80 and 5 nm, respectively). This results in the two transverse graphene based junctions as mentioned before, namely the SGS and the NGN junctions as has been shown in Fig.5.1. In the end, a 25 nm thick Al_2O_3 layer was deposited by using atomic layer deposition which was followed by the fabrication of individual overall top gate electrodes made of Ti/Cu/Al (5, 100 and 5 nm, respectively). In the normal metal electrode as well as in the gate electrode, the Ti layer serves as an adhesion layer while the Al layer works as the capping layer to protect Cu from oxidation. Details on the fabrication methods have already been provided in **Chapter 3**.

Fig.5.1 shows the two devices that were experimentally studied to provide the results discussed in this chapter. Fig.5.1(a) shows device A which shares a 4 μm long junction between the two N electrodes and a 0.46 μm long junction between the S electrodes that defines the width of the NGN junction. The width of the graphene channel along the S electrodes is 2 μm. Across the SGS junction, this device falls in the category of high aspect ratio with W/L being close to 4.3 . In Fig.5.1(b), device B is shown where the

length of the NGN junction is 1 μm and its width is 0.36 μm which defines the length of the SGS junction. The width of the SGS junction for this device is 0.47 μm. With W/L being close to 1.2 across the SGS junction, this device has comparatively lower aspect ratio than device A.

5.2 Normal state characterisation

As these devices have two transverse junctions with different materials used for the contact electrodes, the electronic transport through the two transverse graphene based channels might have different properties despite the fact that they share the same graphene layer. In the light of this, normal state characterisation of these devices was carried out before the devices were cooled down below the critical temperature of the superconducting electrode. The experimental results obtained from the normal state measurements of the two devices are presented and discussed in this section.

5.2.1 Gate dependent electronic transport

Fig. 5.2(a) and (b) show the gate-dependent resistance across the SGS and NGN junctions, respectively, as observed in device A at 6 K under zero magnetic field. It is to be noted that the Ti/Al electrode is in its normal state at this temperature, and hence, the categorisation "SGS" is not factually correct but has been kept as that for the sake of simplicity. As the measurements are conducted in a pseudo-four probe or three-probe configuration which includes the contact resistance, the comparison is only qualitative. It can be clearly seen that the two curves are quite different from each other with different charge neutrality points (CNP) for the two junctions (V_{CNP} = -2.3 V for the SGS junction and V_{CNP} = -1.8 V for the NGN junction), and a higher asymmetry in the resistance for the p-doped and n-doped regions across the SGS junction as compared to the NGN junction. It can be explained by taking into account that the two junctions behave like two individual two-terminal devices. Across the SGS junction, the device is 2 μm wide and 0.46 μm long which makes it a wide and short device. On the contrary, the device is 0.46 μm wide and 4 μm long across the NGN junction which makes it a narrow and long device. As the device is quite short across the SGS junction as compared to the NGN junction and the electrode material is different as well for the two junctions, lower gate coupling due to short junction effects, and difference in effective doping from the contact electrodes could result in a higher V_{CNP} across the SGS junction than the V_{CNP} across the NGN junction. This effective doping from the contact electrodes and the short channel across the SGS junction also explain the observed asymmetry in the resistance of the device between the p-doped and n-doped regions. These conditions also suggest the formation of a coherent electronic cavity in the p-doped region. Fabry-Pérot resonances observed in the p-doped region in Fig. 5.2(a) (also shown in the inset of the figure) serve

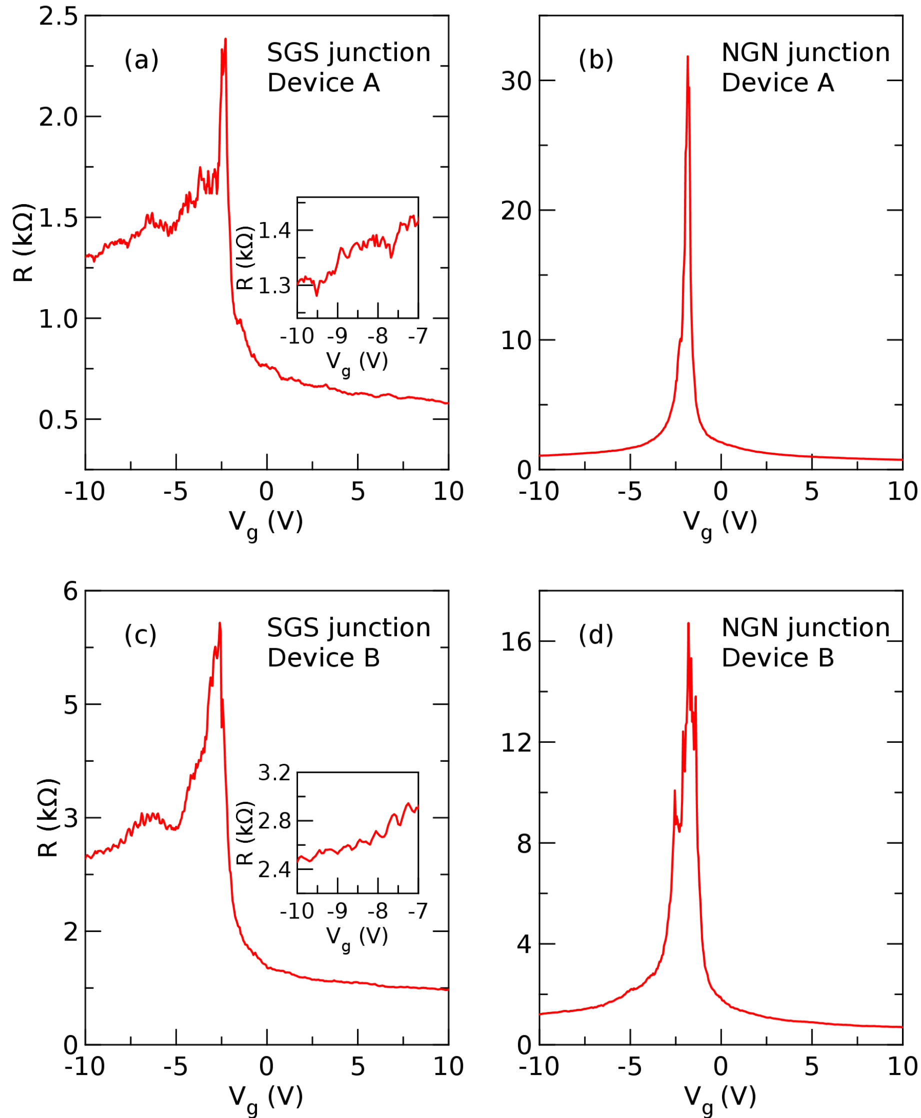

Figure 5.2: Resistance measured as a function of the gate voltage V_g at $T = 6\,\mathrm{K}$ across (a) and (c) the Superconductor/graphene/superconductor (SGS) junction for device A and device B, respectively, inset: resistance oscillations observed in the hole-doped regime. (b) and (d) the Normal metal/graphene/normal metal (NGN) junction for device A and device B, respectively.

as a proof for the formation of the electronic cavity and show that the device is in the ballistic transport regime across the SGS junction.

Fig. 5.2(c) and (d) show the gate-dependent resistance across the SGS junction and NGN junction, respectively, for device B which were measured at the same temperature as for device A. Comparing Fig. 5.2(a) with Fig. 5.2(c), and Fig. 5.2(b) with Fig. 5.2(d), it can be concluded that the characteristics across the SGS junction and the NGN junction

in both of the devices are quite similar qualitatively. The main difference between the two devices across the SGS junction is in terms of the charge neutrality point as V_{CNP} is -2.6 V for device B as compared to -2.3 V for device A. It can be explained by considering the dimensions of the SGS channel in the two devices. In device B, the SGS channel is 0.36 μm long as compared to 0.46 μm in device A. The difference in V_{CNP} can be attributed to the difference in the length of the two devices where a comparatively shorter device might have higher effective contact electrode doping leading to a higher V_{CNP}. At this point, it is worth noting that the difference in the length of the two devices across the SGS junction is 0.1 μm and hence, a difference in gate coupling efficiency for the SGS junctions in the two devices, if any, is expected to be insignificant. As can be seen in Fig. 5.2(c) (also in the inset), device B also exhibits clear Fabry-Pérot resonances in the p-doped region indicating ballistic transport across the SGS junction. Comparing the transport across the NGN junction in device A and device B as seen in Fig. 5.2(b) and (d), respectively, the V_{CNP} across the NGN junction in both of the devices is measured to be -1.8 V. It suggests that in device B, compared to the SGS junction, the NGN junction is still in the long junction regime and might have a higher gate coupling efficiency than the SGS junction.

The gate coupling efficiency α was extracted from the Shubnikov de Haas oscillations and found to be $3.496 \times 10^{11}\,\mathrm{V^{-1}cm^{-2}}$ across the SGS junction and $4.345 \times 10^{11}\,\mathrm{V^{-1}cm^{-2}}$ across the NGN junction which indicates that the two junctions are not equally coupled to the gate. It also suggests that the entire graphene channel across the NGN junction might behave as a three segment channel with respect to the gate voltage control: the middle segment being controlled by the gate coupling across the SGS junction and the two outer segments being controlled by the gate coupling across the NGN junction. It is to be noted that an applied gate voltage along with the gate coupling efficiency α, defines the charge carrier density. It suggests that these different gate-controlled segments will correspond to different charge carrier densities which, therefore, will result in different doping levels through the junction. Considering different V_{CNP} and α_{g} for the SGS and NGN junctions, it can be estimated that the charge carrier density $n = \alpha|V_{\mathrm{g}} - V_{\mathrm{CNP}}|$ will be $4.4 \times 10^{12}\,\mathrm{cm^{-2}}$ across the mid segment of the graphene channel (SGS junction) and $5.1 \times 10^{12}\,\mathrm{cm^{-2}}$ in the two outer segments (NGN junction) at $V_{\mathrm{g}} = 10\,\mathrm{V}$ in device B. This will give rise to additional interfaces in the graphene channel along the NGN junction in addition to the metal/graphene interfaces at the two ends of the channel.

5.2.2 Fabry-Pérot resonances and ballistic transport

As it is shown in Fig. 5.2(a) and (c), the FP-resonances can be observed for the electronic transport across the SGS junction in both of the devices. It was discussed in **Chapter 4** that these resonances can be tuned by tuning the Fermi wavevector which in turn, can be modified by the gate voltage while the energy of the resonances can be modified by the applied bias voltage across the device. Therefore, to study these resonances in

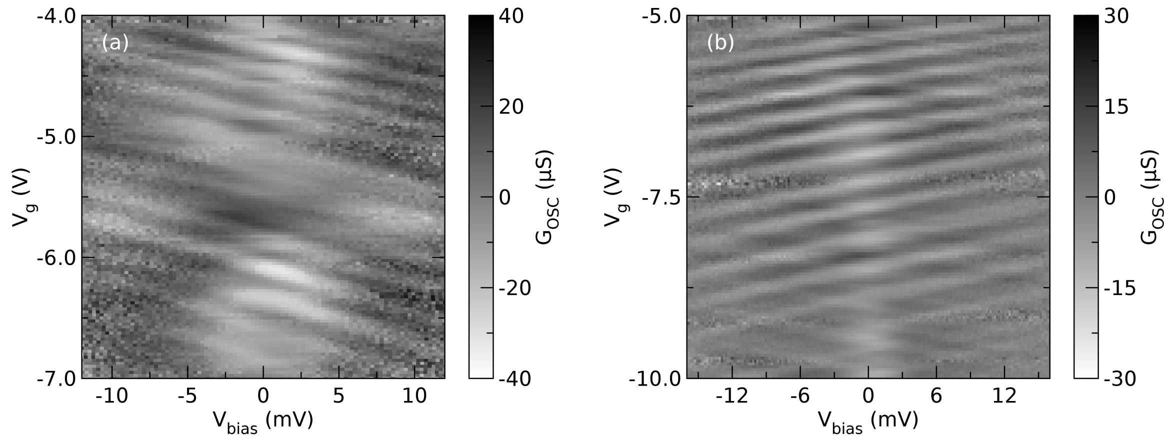

Figure 5.3: Bias spectroscopy of the Fabry-Pérot resonances in the normal state at $T = 6\,\mathrm{K}$ and $B = 0$ as a function of V_g for (a) device A, and (b) device B.

detail, bias spectroscopy measurements were conducted for both of the devices with the gate voltage being another tuning parameter. Fig. 5.3(a) and (b) show the oscillating differential conductance G_OSC as a function of V_g and bias voltage V_bias for device A and B, respectively. As the conductance profile of the device changes strongly with V_g and V_bias, a non-oscillating background conductance was subtracted to increase the visibility of the conductance oscillations. It can be immediately observed in these FP-resonance maps that device A shows a stripe-like interference pattern (similar to the one observed in **Chapter 4**, Fig. 4.4(a)) while device B shows a comparatively homogeneous but weak checkerboard pattern with one set of stripes being more prominent than the other. It indicates that the two graphene/metal contact interfaces defining the FP-cavity region are asymmetric in terms of transmission and this asymmetry is higher in device A (stripe like interference pattern) while it is relatively weaker in device B (weak checkerboard pattern). Another important fact is that these resonances are quite pronounced in device B compared to device A which suggests that the FP-cavity forming in device B is comparatively stronger than the cavity in device A. It can be understood by considering the fact that the cavity in these devices is defined by the formation of the pn-junctions in the vicinity of the metal graphene interfaces when the graphene channel is p-type doped by an applied gate voltage. It suggests that the cavity formed in this way will become weaker and ultimately, incoherent as the graphene channel becomes longer. Estimating the cavity length from these FP-resonances results in a cavity length L_C $\sim$450 $\pm$ 5 nm in case of device A and $\sim$353 $\pm$ 3 nm in case of device B. As the extracted L_C is in agreement with the device length for both of the devices, it can be established that the electronic transport is in the ballistic regime across the SGS junction in these devices.

5.3 Magnetic field dependence of the supercurrent

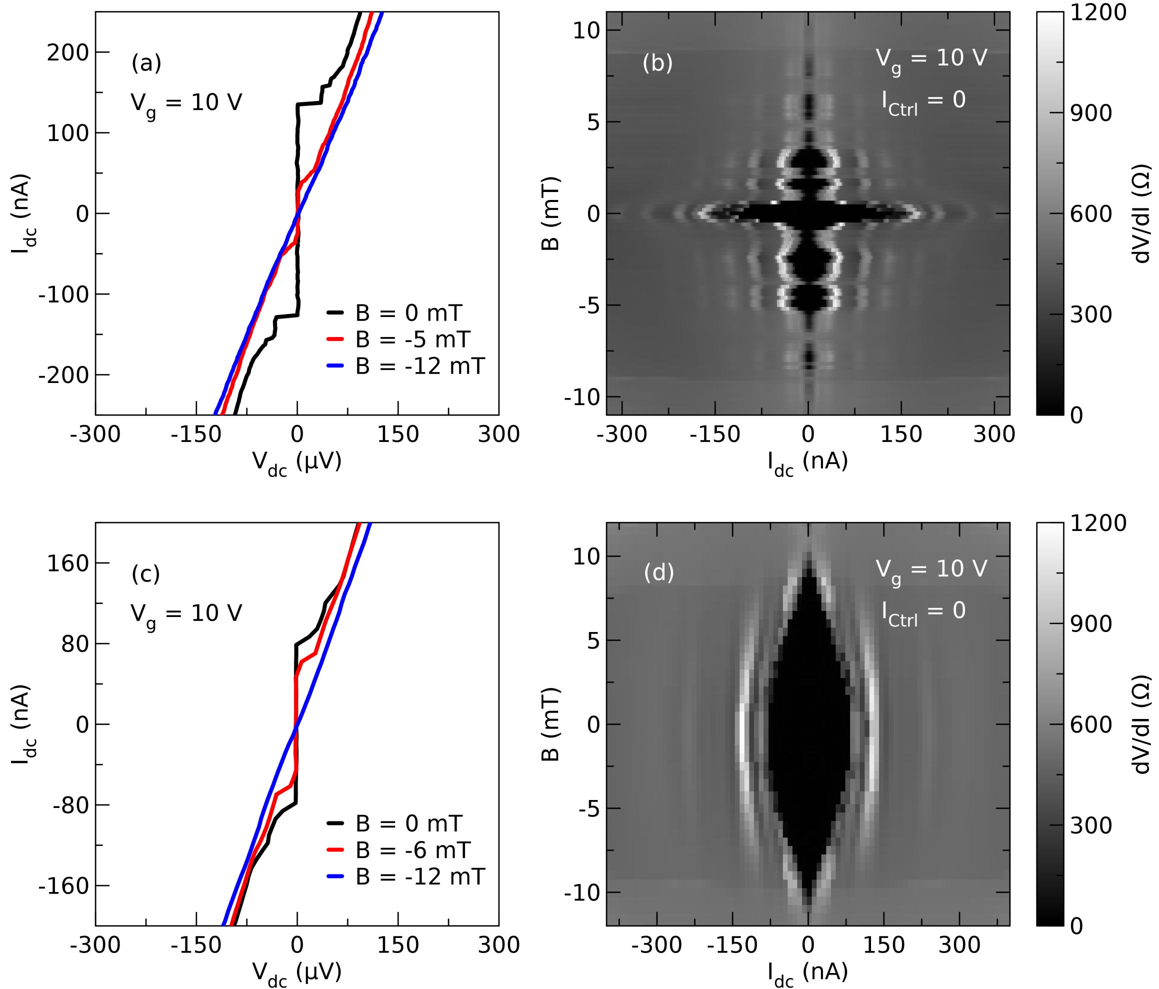

Figure 5.4: (a) and (c) Select $I-V$ characteristics in the presence of the perpendicular magnetic field B measured at $V_{\mathrm{g}} = 10\,\mathrm{V}$ and $T = 50\,\mathrm{mK}$ for device A and device B, respectively. (b) and (d) Magnetic field dependence of the supercurrent at the same V_{g} and T value for device A and device B, respectively. It is to be noted that a magnetic field offset correction was made in case of device A and therefore, the magnetic field represents the applied magnetic field in (a) and (b).

Supercurrent in a wide and short Josephson junction (rectangular junction having uniform current density distribution) modulates with a perpendicular magnetic field according to the relation

$$I_{\mathrm{c}}(B) = I_{\mathrm{c}}(0)\,\frac{\sin(\pi\phi/\phi_0)}{\pi\phi/\phi_0} \tag{5.1}$$

where $I_c(B)$ denotes the critical current at a perpendicular magnetic field B, $I_c(0)$ denotes the critical current at zero magnetic field, ϕ_0 denotes the magnetic flux quantum, and $\Phi = B \cdot A$ is the magnetic flux passing through the junction where A is the junction area. It is clear from Eqn. 5.1 that in a wide and short Josephson junction, the critical current follows a $\text{sinc}(\pi\phi/\phi_0)$ interference pattern in the presence of a perpendicular magnetic field, also known as the Fraunhofer pattern due to its similarity to the single-slit Fraunhofer interference pattern. However, this magnetic field interference pattern strongly depends on the current density distribution in the Josephson junction [109].

Fig. 5.4(a) and (b) show the effect of an applied perpendicular magnetic field B (offset-corrected) in case of device A at $V_g = 10$V and $T = 50$ mK. It is to be noted that during these measurements, no bias voltage or current was applied across the NGN channel. The supercurrent in the device is strongly tuned by the magnetic field and an oscillatory dependence can be clearly observed. The maximum critical current observed at zero magnetic field is ∼130 nA in this device. However, there is a clear asymmetry in the behaviour of the supercurrent for the positive and negative values of the magnetic field. This asymmetry is due to the flux trapping in the magnet itself and hence, could not be remedied in the measurement and analysis. Despite this externally induced asymmetry in the magneto-interference pattern, it can be loosely concluded that this device shows the oscillatory behavior of $I_c(B)$ as expected from a rectangular Josephson junction.

Fig. 5.4(c) and (d) show the magnetic field dependence of I_c in device B at $V_g = 10$V and $T = 50$ mK. It corresponds to the same measurement condition as for device A in Fig. 5.4(a) and (b). The maximum I_c observed at zero magnetic field in this device is ∼80 nA. Comparing the magnetic field dependence maps of the two devices, clear distinction can be seen as device B shows a slow, decaying pattern instead of the oscillatory behavior of $I_c(B)$. The Josephson junction in device B is comparatively smaller in dimensions than the junction in device A and geometrically falls in the category of W/L close to 1 . The observed behavior of $I_c(B)$ in this device is in agreement with the behaviour of low aspect ratio constrictions [25, 110–114].

5.4 Tuning the supercurrent in graphene based Josephson junctions

Controlling and tuning the supercurrent is an important part of the graphene based Josephson junctions [16, 17, 19, 25, 74, 115]. In this section, two important parameters are discussed which are used to control the supercurrent in these multiterminal devices. The first one is tuning the supercurrent with an applied gate voltage which has been demonstrated in most of the graphene based Josephson junctions and stems from the gate-controlled conductance of the graphene weak link.

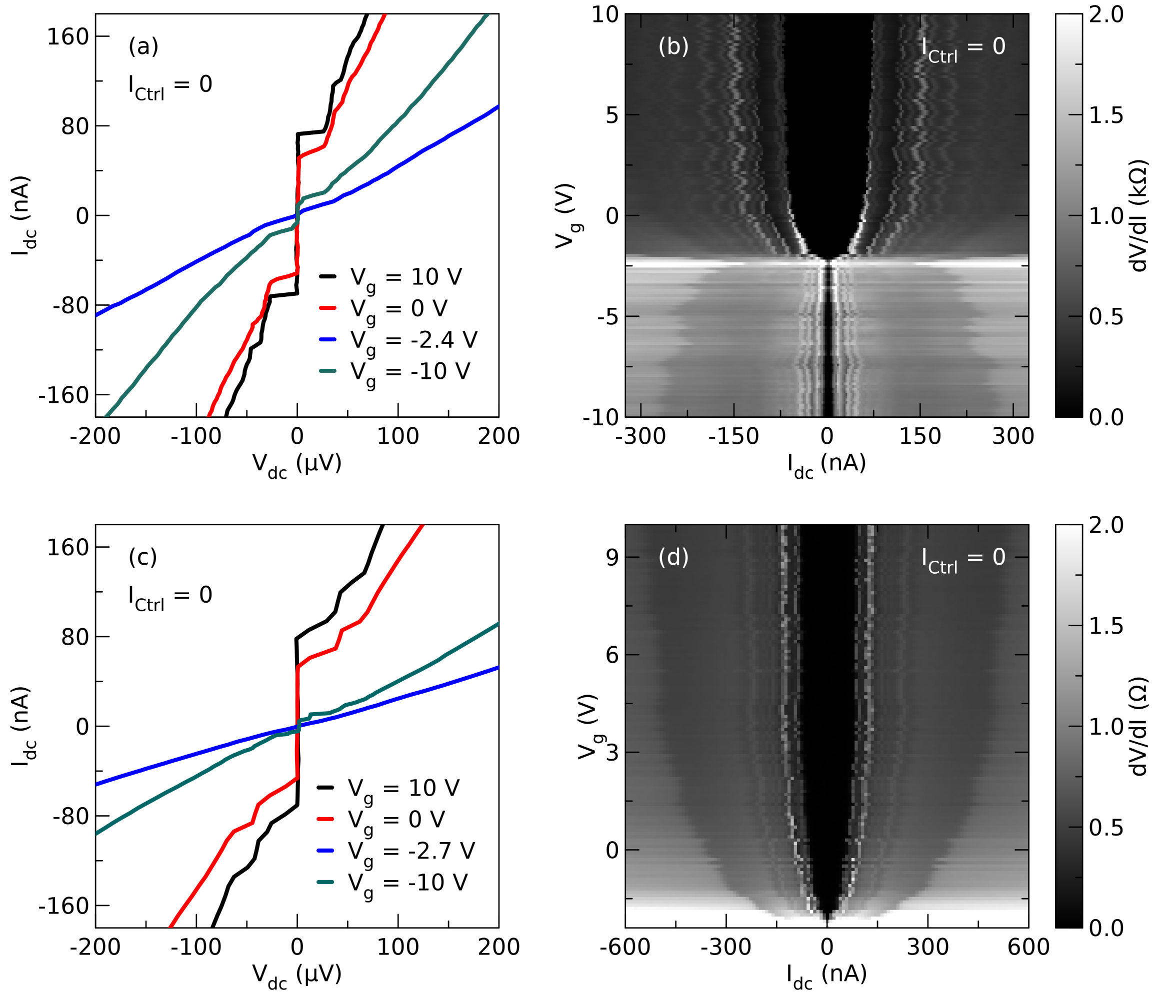

Figure 5.5: (a) and (c) Select $I-V$ characteristics at various V_g measured at $I_{\mathrm{Ctrl}}=0$ and $T=50\,\mathrm{mK}$ for device A and device B, respectively. (b) and (d) Gate voltage dependence of the supercurrent at the same I_{Ctrl} and T value for device A and device B, respectively.

The second one is tuning the supercurrent by passing a transverse current or applying a transverse potential across the Josephson junction which changes the occupation of the Andreev states in the Josephson junction [103–107]. This change in the occupation of the Andreev states is reflected in the magnitude of the supercurrent. In these multiterminal devices, it can be achieved by passing a control current I_{Ctrl} along the NGN junction which influences the supercurrent-carrying states in the graphene channel that forms the Josephson weak link in the SGS junction.

5.4.1 Gate voltage controlled supercurrent

One of the most important properties of the graphene based Josephson junctions is the gate voltage control over the supercurrent [16, 17, 19, 25, 74, 115]. In most of the graphene based devices, a supercurrent can be observed across the entire gate voltage range when the doping is tuned from n-type to p-type or vice versa. The magnitude of the supercurrent is tuned with the gate voltage due to the change in the resistance of the graphene weak-link.

A similar trend was observed in case of device A as shown in Fig. 5.5(a) and (b) as measured at $T = 50\,\mathrm{mK}$ and $B = 0$. It is to be noted that during these measurements no bias or current was applied across the NGN junction. Fig. 5.5(a) shows the $I-V$ characteristics at select V_g. It can be readily seen that the magnitude of the critical current I_c changes at different V_g values. The device is close to the normal state when the gate voltage is close to V_CNP and has a very small critical current in the p-doped regime even at high charge carrier density. On the other hand, it has a noticeable I_c in the n-doped regime. This dependence of I_c fits well with the resistance profile of the device across the SGS junction. An important point to be noted here is the magnitude of I_c which is not $\sim 130\,\mathrm{nA}$ at $V_\mathrm{g} = 10\,\mathrm{V}$ as seen in Fig. 5.4(a) at $B = 0$. It is due to a shift in the effective zero magnetic field and hence, the device was in a non-zero magnetic field during the measurement which led to a smaller I_c value. Fig. 5.5(b) shows the differential resistance dV/dI map measured across the SGS junction as a function of the bias current I_dc and V_g. A residual resistance of $6-18\,\Omega$ was observed and forms the central dark region of the map defined inside the high resistance envelope. As observed in the $I-V$ characteristics, the device has a relatively higher I_c in the entire n-doped region as compared to the p-doped region. Another important feature is the appearance of the equidistant, self-induced Shapiro steps-like switchings (can be clearly seen as step-like features in Fig. 5.5(a) and (c)) which appear as distinct resistance features that seem to follow the supercurrent. The origin of these features is unclear in these devices as they appear at constant energy values and their positions remain unaffected by the gate voltage and the magnetic field, and hence, can be attributed to the electromagnetic environment of the device.

Fig. 5.5(c) and (d) show the $I-V$ characteristics and the dV/dI map across the SGS junction as a function of I_dc and V_g measured at $T = 50\,\mathrm{mK}$ and $B = 0$ in device B. Similar to the measurements on device A, these measurements were conducted without any bias voltage or current across the NGN junction. As can be seen in Fig. 5.5(c) the device shows I_c $\sim$80 nA at $V_\mathrm{g} = 10\,\mathrm{V}$ in the n-doped region, however, it is not in the superconducting state close to V_CNP which corresponds to the characteristics at $V_\mathrm{g} =$ -2.7 V. The device has slightly non-linear characteristics in the p-doped regime as shown at $V_\mathrm{g} =$ -10 V corresponding to p-type high charge carrier density. This non-linearity is due to a dip in the resistance of the device in the p-doped regime while the device

does not show any measurable supercurrent. Fig. 5.5(d) shows the dV/dI across the SGS junction measured as a function of I_{dc} and V_{g} in a limited gate voltage range where a supercurrent could be measured. It can be clearly seen that the device gets highly resistive as V_{g} approaches V_{CNP}. Comparing device A and device B, a smaller I_{c} is observed in device B than device A which is natural due to the dimensions of the devices. For both of the devices, superconductivity is suppressed close to their respective V_{CNP}, however, the major difference between the two devices is their behaviour in the p-doped regime. Here, device A remains superconducting even though it has a rather small I_{c} of $\sim$15 nA, while device B is not in the superconducting regime despite a small resistance dip close to zero bias. In case of device B, it is safe to say that a measurable supercurrent appears only in the n-doped regime, while in the p-doped regime, the supercurrent is too small to be measured. Therefore, it is clear that the supercurrent can be efficiently tuned in graphene based Josephson junctions by tuning the dimensions of the weak link.

5.4.2 Tuning the supercurrent with a transverse normal current

As mentioned before, supercurrent through a Josephson junction can be tuned by a transverse normal current/potential difference which changes the occupation of the Andreev states in the weak link. In these devices, the bias current I_{dc} is applied across the SGS junction, the transverse current or the control current I_{Ctrl} is applied across the NGN junction, and the differential resistance is measured across the SGS junction.

Fig. 5.6 shows the tuning of the supercurrent in the n-doped regime at $V_{\mathrm{g}} = 0\,\mathrm{V}$ (Fig. 5.6(a) - (c)), and 10 V (Fig. 5.6(d) - (f)) as measured in device A at $T = 50\,\mathrm{mK}$ under zero magnetic field. Comparing the $I - V$ characteristics as shown in Fig. 5.6(a) and (d), it can be clearly seen that the magnitude of I_{c} is strongly tuned by the control current I_{Ctrl}. Fig. 5.6(b) and (e) show the dV/dI map across the SGS junction as a function of I_{dc} and I_{Ctrl}. It can be clearly seen that higher the magnitude of the supercurrent, higher is the magnitude of the control current that is required to diminish it. However, in both of the cases, even at high control current, the device shows slight non-linearity indicating a dip in the resistance. Fig. 5.6(c) and (f) show the same data as (b) and (e), respectively, except the fact that the control current is translated to the control voltage V_{Ctrl} which denotes the potential difference across the NGN junction. For this device, $V_{\mathrm{Ctrl}} \approx 300\,\mu\mathrm{V}$ shifts the potential difference across the NGN channel above 2Δ where Δ denotes the superconducting gap. While this device does not show any sign of the π-junction phenomenon as observed by Baselmans *et al.* (disappearance and reappearance of the supercurrent as a function of I_{Ctrl}) in a similar device geometry with diffusive Josephson weak link [104], the supercurrent is continuously tuned by the control current throughout the entire $V_{\mathrm{Ctrl}} \leq 2\Delta$ range, as can be clearly seen in Fig. 5.6(b) and (c), and (e) and (f). Apart from this, there is an asymmetry in the magnitude of I_{c} for low I_{Ctrl} or

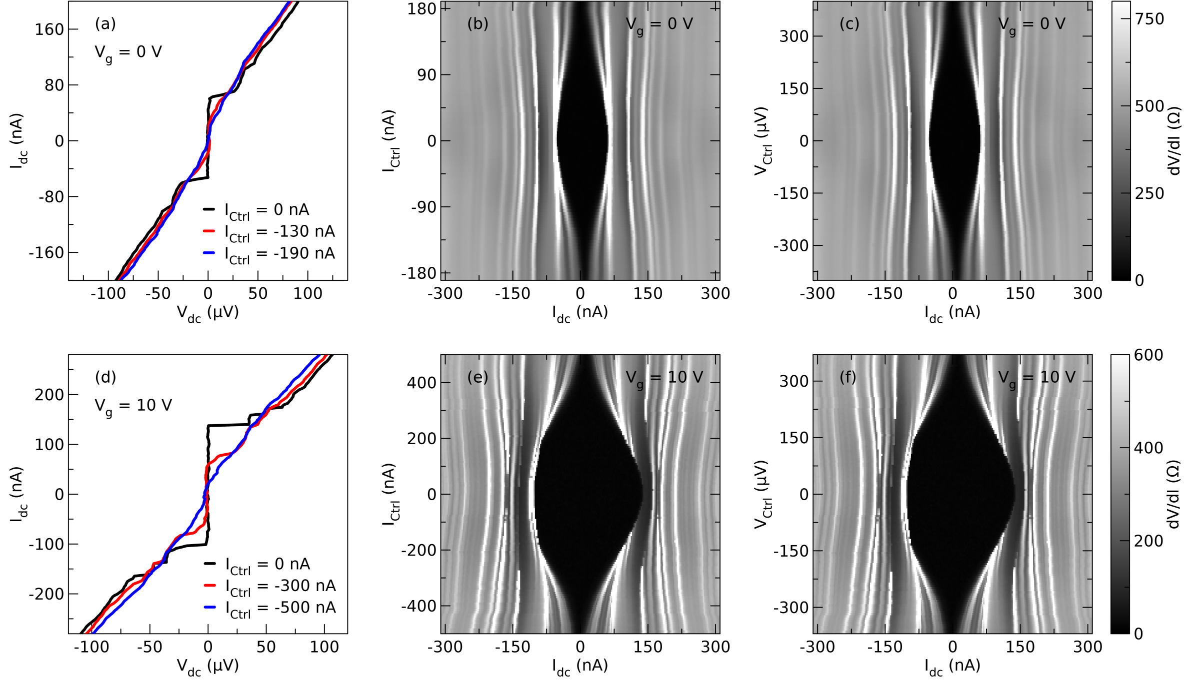

Figure 5.6: Experimental data from device A in the n-doped region at $T = 50\,\mathrm{mK}$, $B = 0$ and $V_\mathrm{g} = 0$ and $10\,\mathrm{V}$, respectively, (a) and (d) Select $I - V$ characteristics with an applied control current I_Ctrl, (b) and (e) differential resistance dV/dI map as a function of bias current I_dc and I_Ctrl, (c) and (f) dV/dI map as a function of I_dc and control voltage V_Ctrl.

V_Ctrl as seen in Fig. 5.6(d), (e) and (f) with respect to I_dc. One plausible reason for this asymmetry could be the self-heating of the device at high I_c, and since the bias-dependent measurements were made by sweeping the I_dc from the negative to positive side for the entire measurement range, the self-heating might generate the observed asymmetry with respect to I_dc.

As discussed in section 5.4.1, device A shows superconducting behaviour in the p-doped regime although with a smaller I_c than in the n-doped regime. Fig. 5.7(a) and (b) show the $I - V$ characteristics of this device measured in the p-doped regime at $V_\mathrm{g} =$ -10 V and -5 V, respectively, at 50 mK and zero magnetic field. It is clear that the state of the device can be tuned from superconducting to normal with a relatively lower I_Ctrl as compared to Fig. 5.6 (a) and (d).

Fig. 5.8(a)-(c) show the dV/dI across the SGS junction as a function of I_dc and I_Ctrl, I_dc and V_Ctrl, V_dc (dc bias voltage across SGS junction) and V_Ctrl, respectively, at $V_\mathrm{g} =$ -10 V. Fig. 5.8(d)-(e) show the similar measurements at $V_\mathrm{g} =$ -5 V. Two distinct features can be observed in the p-doped regime as compared to the n-doped regime: first, I_c can be quenched completely by applying a comparatively smaller control current/voltage; second, intersecting linear features making a diamond-like shape in the central region

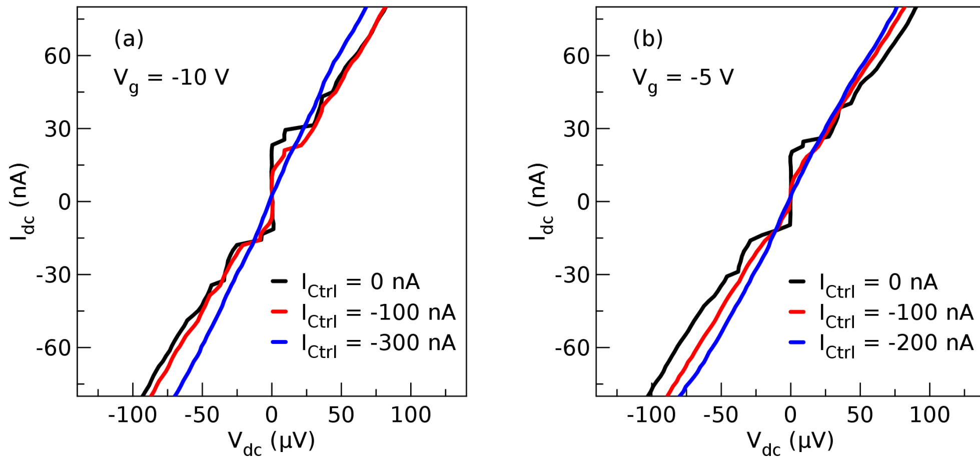

Figure 5.7: Select $I-V$ characteristics with an applied control current I_{Ctrl} in the p-doped region for device A at $B = 0\,\mathrm{mT}$, $T = 50\,\mathrm{mK}$ and (a) V_{g} = -10 V and, (b) V_{g} = -5 V.

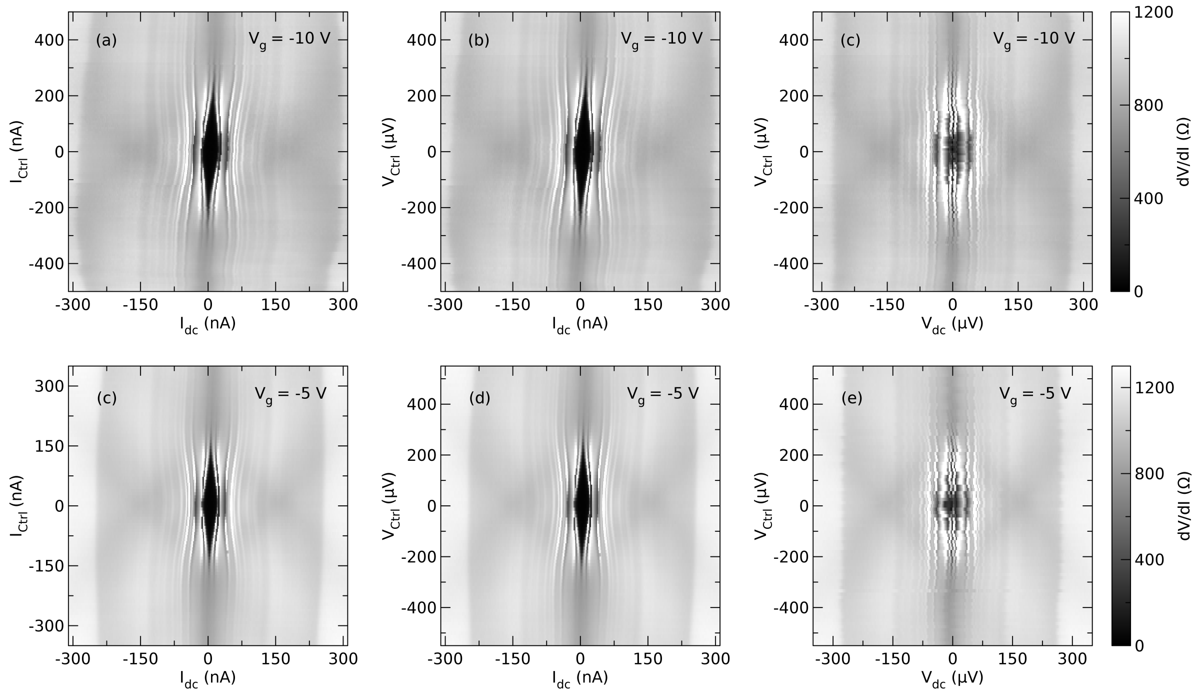

Figure 5.8: Experimental data from device A in the p-doped region at $T = 50\,\mathrm{mK}$, $B = 0$ and V_{g} = -10 and -5 V, respectively, (a) and (d) differential resistance dV/dI map as a function of the bias current I_{dc} and control current I_{Ctrl}, (b) and (e) dV/dI map as a function of I_{dc} and control voltage V_{Ctrl}, (c) and (f) dV/dI map as a function of the bias voltage V_{dc} and V_{Ctrl}.

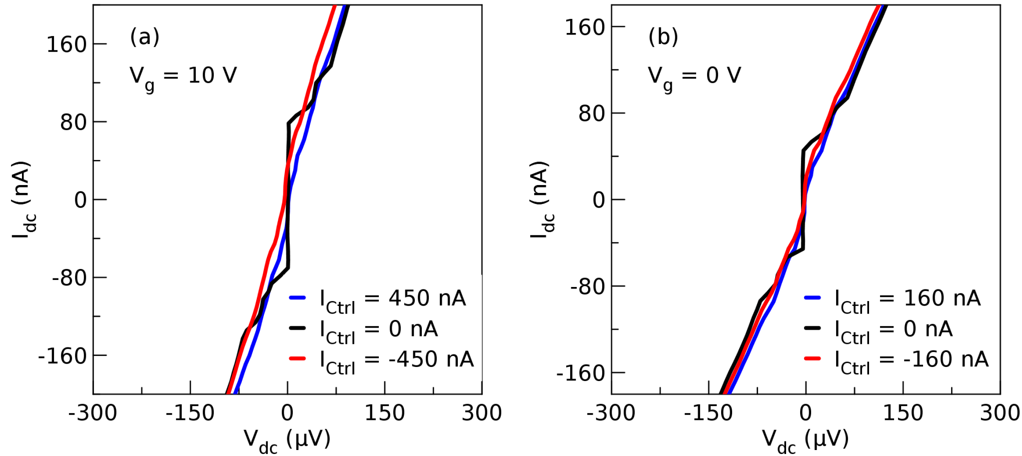

Figure 5.9: Select $I-V$ characteristics with an applied control current I_{Ctrl} in the n-doped region for device B at $B = 0\,\mathrm{mT}$, $T = 50\,\mathrm{mK}$ and (a) $V_{\mathrm{g}} = 10\,\mathrm{V}$ and, (b) $V_{\mathrm{g}} = 0\,\mathrm{V}$.

of the dV/dI map. The first one can be understood by taking into account that the magnitude of I_{c} is quite small in the p-doped regime implying that the device is weakly superconducting. Therefore, it can be easily influenced by external factors such as a change in the occupation of the current carrying states caused by the control current/voltage. The second feature, the diamond-like feature, in these devices corresponds to the charge transport along the corners of the Josephson weak link under an applied bias, *i. e.*, the transport along the NS corners of the device through the graphene channel. While this feature is present throughout the entire range of the gate voltage, its visibility is affected by the gate dependent conductance of the graphene channel. Since the overall conductance of the graphene channel is higher in the n-doped regime, a small change in the conductance caused by the transport along the NS corners gets overshadowed. In terms of energy, the tip and the bottom of the diamond along $V_{\mathrm{dc}} = 0$ denote the threshold $V_{\mathrm{Ctrl}} = \pm 2\Delta/e$ for the NGN junction where Δ denotes the superconducting gap. In this device, this threshold seems to appear at $V_{\mathrm{Ctrl}} \approx 300\,\mu\mathrm{V}$. This transport feature is discussed in detail in the successive chapter and no further details are provided here in order to avoid redundancy. The vertical conductance lines observed at $V_{\mathrm{dc}} = \pm 260\,\mu\mathrm{V}$ and $\pm 130\,\mu\mathrm{V}$ in Fig. 5.8(c) and (f) show the multiple Andreev reflections (MAR) at $2\Delta/e$ and Δ/e. The other MAR features, if present, are not clearly visible due to the self-induced Shapiro steps-like feature.

Fig. 5.9(a) and (b) show the $I-V$ characteristics measured in device B at $V_{\mathrm{g}} = 10\,\mathrm{V}$ and $0\,\mathrm{V}$ at $T = 50\,\mathrm{mK}$ and zero magnetic field. Similar to the data obtained from device A (as shown in Fig. 5.6(a) and (e)), the I_{c} in device B can be tuned with I_{Ctrl}. These $I-V$ characteristics also support the data shown in Fig. 5.7 that the magnitude of I_{Ctrl} required to diminish the supercurrent/superconductivity in the device depends on the

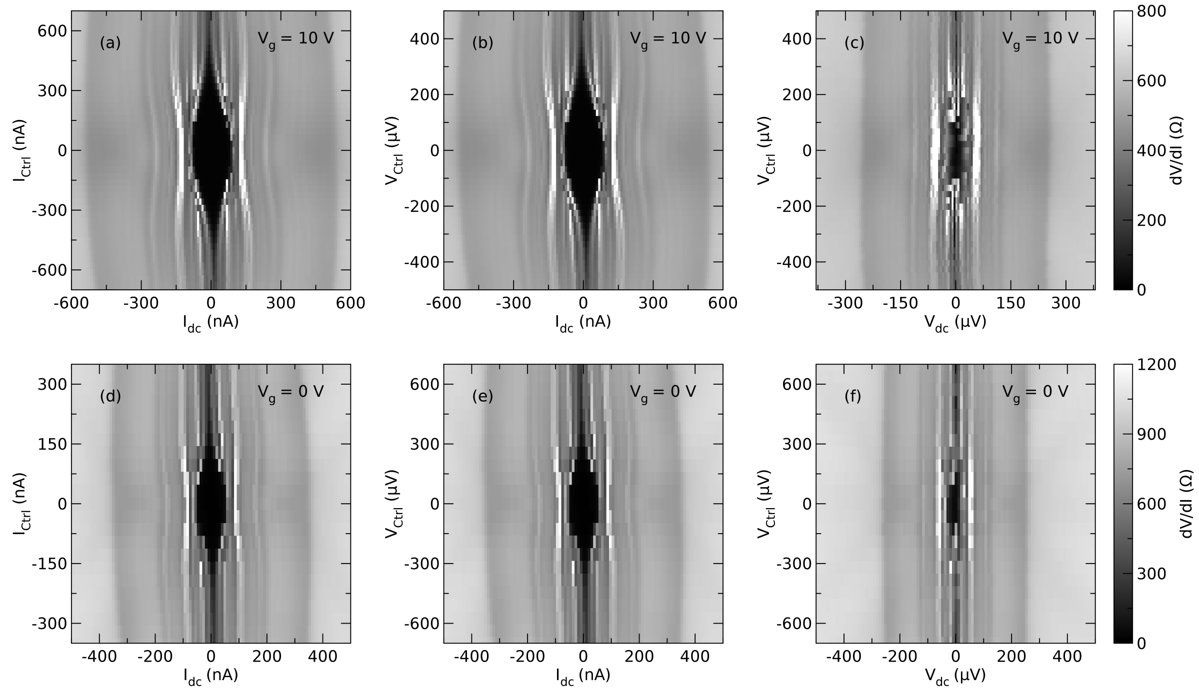

Figure 5.10: Experimental data from device B in the n-doped region at $T = 50\,\mathrm{mK}$, $B = 0$ and $V_\mathrm{g} = 10\,\mathrm{V}$ and $0\,\mathrm{V}$, respectively, (a) and (d) differential resistance dV/dI map as a function of the bias current I_dc and control current I_Ctrl, (b) and (e) dV/dI map as a function of I_dc and control voltage V_Ctrl, (c) and (f) dV/dI map as a function of the bias voltage V_dc and V_Ctrl.

magnitude of I_c.

The dV/dI maps for device B are shown in Fig. 5.10 at $V_\mathrm{g} = 10\,\mathrm{V}$ and $0\,\mathrm{V}$, and they bear similar features to the dV/dI maps shown in Fig. 5.8 and 5.7 for device A. Comparing Fig. 5.10 with Fig. 5.8, weak hints of the diamond-like pattern can be seen in the dV/dI maps of device B in the n-doped region as seen in the p-doped region in device A. It suggests that the transport along the NS corners is a likely mechanism of charge transport in these devices with the multiterminal geometry. It also supports the fact that while the transport along the NS corners is always present, its visibility depends on the conductance of the device. Another similar feature between the two devices is the appearance of the MAR features at $V_\mathrm{dc} = \pm\,260\,\mu\mathrm{V}$ and $\pm\,130\,\mu\mathrm{V}$ corresponding to $2\Delta/e$ and Δ/e, respectively. The main difference between the two devices is the magnitude of the I_c, and the I_Ctrl required to bring the device in the normal state which can be understood by considering the difference in their dimensions. In this device as well, no signature of π-junction could be observed while I_c is continuously tuned by I_Ctrl. One possible reason for the absence of the π-junction behavior could be the difference in the charge transport across the Josephson junction itself in these graphene based ballistic

devices as compared to the diffusive metallic Josephson junctions, as pointed out by Wilhelm *et al.* [103]. The authors acknowledge that the dimensions of the two transverse junctions might play a significant role in the tuning of the Josephson junction while the basic physics of the controlled supercurrent (change in the occupation of the Andreev levels in the weak-link) remains the same. A similar study by Sammuelsson *et al.* [105] also shows the significant changes in the transport properties of the Josephson weak links which depend on the dimensions of the junctions as well as on the contact interfaces.

5.5 Conclusion

To conclude, the electronic transport data in multiterminal graphene devices with two transverse junctions was presented and discussed in this chapter. It was shown that while the two junctions share the same graphene channel, they have different response to an applied gate voltage which was seen in their gate coupling efficiency as well as their different charge neutrality points. Signature of ballistic transport across the short junction (SGS junction) was observed in both of the devices as seen in the Fabry-Pérot interference pattern, however, the interference pattern observed in device B was relatively regular and homogeneous as compared to device A. In terms of the superconducting properties, device A exhibits the magnetic field dependence and gate tunable supercurrent as expected for a wide and short Josephson junction. Device B exhibits the magnetic field dependence as expected for a rather long and narrow junction. In addition, a supercurrent is observed only in the n-doped region in Device B contrary to device A where it is observed in the p-doped region as well. Using the transverse NGN junction for passing a control current I_{Ctrl} through the Josephson weak link in the SGS junction, it was shown that the critical current I_{c} through the SGS junction can be tuned in both of the devices.

Chapter 6

Crossed Andreev reflections in multiterminal graphene based Josephson junction

Nonlocal Andreev processes are of great interest when it comes to the study of normal metal/superconductor junctions as discussed in **Chapter 2**. Signatures of the crossed Andreev reflections (CAR) were observed in superconductor/ferromagnet spin valves [40, 41], while in case of normal metal/superconductor structures, CAR was observed in the metallic as well as in the tunnelling regime [42, 43]. In addition to these hybrid junctions, observation of the nonlocal Andreev reflections in multiterminal Josephson junctions is suggested in a recent theoretical report [116]. Owing to its peculiar electronic band structure, graphene is shown to host the specular Andreev reflection [7, 31], which sparks an obvious interest in studying the nonlocal Andreev processes in graphene based systems. In this direction, the crossed Andreev conversion (CAC) was observed in the encapsulated graphene devices in the quantum Hall regime [53]. CAR features, more precisely, Cooper-pair splitting is theoretically proposed to be observed in graphene based NS junctions by Cayssol [117] where the primary advantage comes from the tuning of the local Fermi level in a graphene channel in n-type graphene/proximitized graphene/p-type graphene scheme. Taking advantage of the tunability of the Fermi level, CAR features are proposed to be observed in graphene based superconducting spin-valves as well [118]. Note that both of these studies consider the local tuning of the Fermi level to encourage the CAR processes in graphene/superconductor systems.

In the light of the above discussion, the focus of the present chapter is to study the Andreev reflection processes in multiterminal graphene based Josephson junction. Due to the geometry of the multiterminal devices (presence of multiple terminals, difference in the gate controlled regions of the graphene channel), these devices are likely to host the nonlocal or crossed Andreev reflection process as discussed above. The experimental

results obtained from the study are presented and explained with an analytical model.

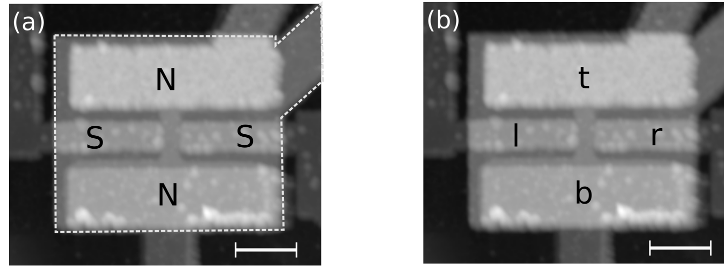

Figure 6.1: (a) AFM image of the device showing the superconductor/graphene/superconductor (SGS) and the normal metal/graphene/normal metal (NGN) junction. The region enclosed with the dashed lines shows the top gate electrode. Scale bar is 1 μm (b) Correlation notation (employed in the model) set for the electrodes with respect to (a).

Fig. 6.1(a) shows the AFM image of the device studied for the detection of the nonlocal Andreev reflection. Note that it is the same device, the device B, which was shown in the previous chapter, (**Chapter 5**) with a 1 μm long and 0.36 μm wide normal metal/graphene/normal metal (NGN) channel, and 0.36 μm long and 0.47 μm wide transverse superconductor/graphene/superconductor (SGS) channel. Fig. 6.1(b) shows the same image as in (a) with the correlation notation for the electrodes that is employed in the model.

6.1 Experimental results

Fig. 6.2(a) shows the four-terminal or the superconductor/graphene/superconductor (SGS) measurement configuration. In this case, the bias voltage V_b is applied across the

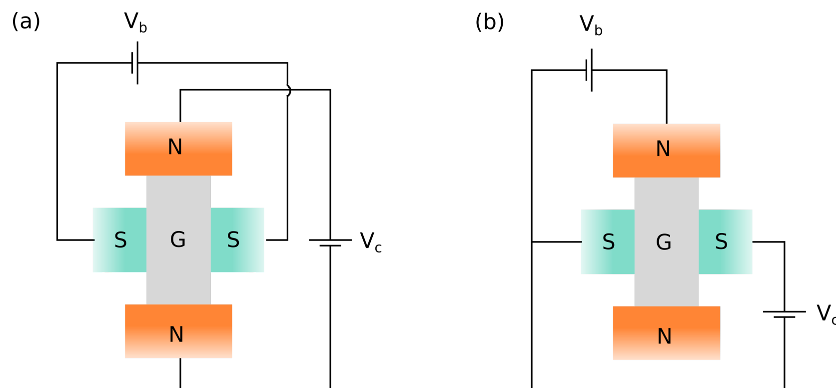

Figure 6.2: (a) Four-terminal measurement configuration (SGS configuration). (b) Three-terminal measurement configuration (NGS configuration). See text in section 6.1 for description.

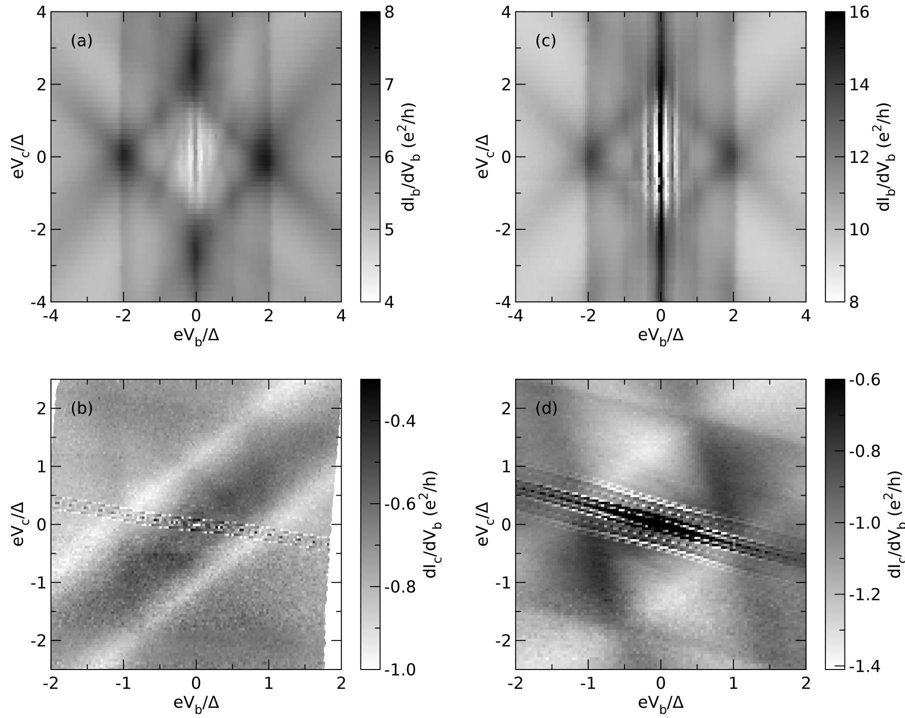

Figure 6.3: (a) Local differential conductance $dI_\mathrm{b}/dV_\mathrm{b}$ map in the SGS configuration (as shown in Fig. 6.2(a)), and (b) nonlocal differential conductance $dI_\mathrm{c}/dV_\mathrm{b}$ map in the NGS configuration (as shown in Fig. 6.2(b)) at V_g = -2.7 V, T = 20 mK and $B = 0$. (c) $dI_\mathrm{b}/dV_\mathrm{b}$ map in the SGS configuration, and (d) $dI_\mathrm{c}/dV_\mathrm{b}$ map in the NGS configuration at V_g = -5.5 V, T = 50 mK and $B = 0$

SGS junction and the control voltage V_c is applied across the NGN junction. Fig. 6.2(b) shows the three-terminal or the normal metal/graphene/superconductor (NGS) measurement configuration. In this case, V_b is applied across one of the NGS junctions and V_c is applied across the SGS junction.

Fig. 6.3(a) shows the local differential conductance $dI_\mathrm{b}/dV_\mathrm{b}$ map in the SGS configuration as measured at V_g = -2.7 V and 20 mK under zero magnetic field. V_b and V_c, both are normalized with the superconducting gap Δ. The vertical features appearing at $eV_\mathrm{b}/\Delta = \pm 1$ and ± 2 are due to the multiple Andreev reflections (MAR) as expected for the SGS junction. In addition, there are few other distinct features present in the map. First is the diamond-like pattern which encompasses the entire measurement range, and second are the cross-like features which can be observed between $|eV_\mathrm{b}/\Delta| \leq 1$ and $|eV_\mathrm{c}/\Delta| \leq 2$. The third feature is a conductance ridge which appears at $eV_\mathrm{b} = 0$ when $|eV_\mathrm{c}/\Delta| > 2$. Fig. 6.3(b) shows the nonlocal differential conductance $dI_\mathrm{c}/dV_\mathrm{b}$ map (across the SGS junction) in the NGS configuration as measured at V_g = -2.7 V under the same conditions as for the measurement in Fig. 6.3(a). Apart from the nearly vertical features (might appear due to the direct transport across the biased NGS channel) and the nearly

horizontal features (might appear due to the transport across the SGS channel), there are additional features that can be observed in this map as well.

In order to assure that the observed features are robust, similar measurements were carried out at V_g = -5.5 V in the p-doped regime. This regime was chosen to avoid the additional features as the supercurrent and the self induced Shapiro-like features which are prominent in the n-doped regime as well as in the highly p-doped regime. Fig. 6.3(c) and (d) show the $dI_\mathrm{b}/dV_\mathrm{b}$ map in the SGS configuration and the $dI_\mathrm{c}/dV_\mathrm{b}$ map in the NGS configuration, respectively, as measured at V_g = -5.5 V and 50 mK under zero magnetic field. Comparing Fig. 6.3(a) and (c) for the measurement in the SGS configuration, the MAR features can be observed at $eV_\mathrm{b}/\Delta = \pm 1$ and ± 2. The diamond-like feature appears to be more symmetric at V_g = -5.5 V than at V_g = -2.7 V (the lines that form the diamond appear to be splitting in Fig. 6.3(a)). On the other hand, the cross-like feature, which appears to be still present at V_g = -5.5 V, suffers in terms of visibility due to the supercurrent and the Shapiro-like features. In addition, the vertical conductance ridge at $eV_\mathrm{b} = 0$ and $|eV_\mathrm{c}/\Delta| > 2$ also cannot be clearly distinguished at V_g = -5.5 V due to the supercurrent feature. Comparing Fig. 6.3(b) and (d) for the measurement in the NGS configuration, similar features can be observed in both of the maps except the additional features in Fig. 6.3(d) in the low V_c regime. These additional features might appear due to the supercurrent and the Shapiro-like features.

Therefore, it can be said that there are additional transport processes taking place other than the directly observable MAR processes. In order to understand and explain the observed experimental results, an analytical model is employed which is described in the next section.

6.2 Analytical model

Credit note: This model was developed by Prof. Detlef Beckmann (Supervisor of this thesis). It is provided in the current thesis for completeness.

As it was shown in **Chapter 5**, Fig. 5.2(c) and (d), the SGS channel and the NGN channel have different charge neutrality points (V_CNP is -2.6 V for the SGS junction and -1.8 V for the NGN junction). It was also discussed that the two junctions have different gate coupling efficiency α_g which translates to the difference in the gate induced charge carrier doping across the two junctions. Fig. 6.4(a) shows the gate induced charge carrier density n in the SGS and NGN channel where n is calculated by using the relation $n = \alpha(V_\mathrm{g} - V_\mathrm{CNP})$. It can be seen that close to the V_CNP of the SGS channel ($n \approx 0$), different doping densities across the SGS channel and the NGN channel can generate pn-junctions. This process is schematically shown in Fig. 6.4(b) for the condition $V_\mathrm{g} = V_\mathrm{CNP}$ along the SGS channel. In this situation, the graphene region across the

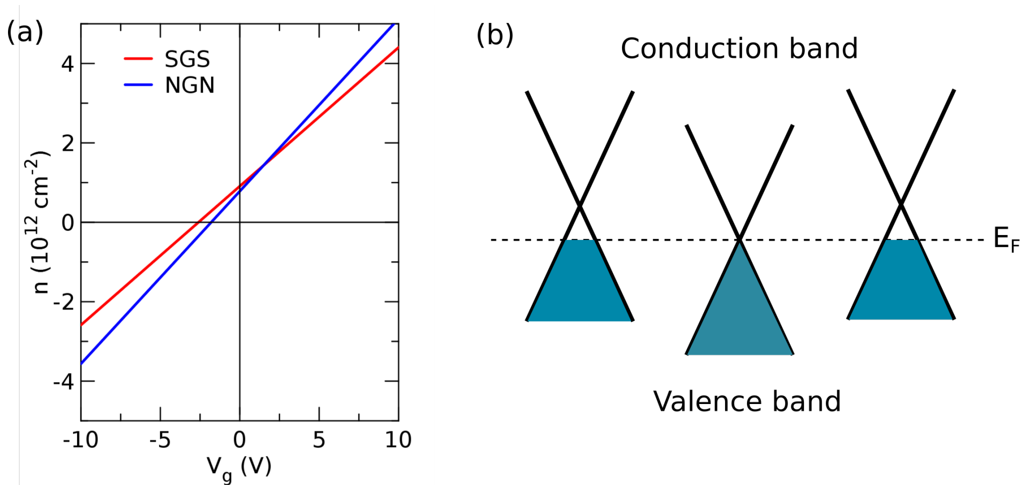

Figure 6.4: (a) Gate induced charge carrier density in the SGS and NGN channel. (b) Schematic of the doping profile across the NGN channel at $V_\mathrm{g} = V_\mathrm{CNP}$ of the SGS channel. The central Dirac cone shows the doping profile in the graphene region across the SGS channel, and the outer cones show the doping profile in the two outer graphene regions along the NGN channel.

SGS junction is at the charge neutrality point (the central Dirac cone in Fig. 6.4(b)), while the outer graphene regions along the NGN channel are p-doped (the left and right Dirac cones in Fig. 6.4(b)). As discussed in **Chapter 2, section 2.4**, in a single layer graphene system, the charge carriers can be transmitted through a potential barrier via the Klein tunnelling where the transmission depends on the barrier profile as well as on the angle of incidence [9, 10, 68]. It is to be noted that the potential barriers generated by the doping profile in this device might not be as sharp as those achieved by using two different gate electrodes to tune the carrier density profile [69]. In the present case, the tunnelling process through the barrier might give rise to nonlocal Andreev reflections. This process is discussed in the current section by using a three-terminal beam splitter.

The model treats graphene as a multichannel conductor connected to four terminals, superconducting terminals (S) on the left and the right, normal metal terminals (N) on the top and the bottom. The terminals labeled l, r, t, and b have transmission probabilities $\tau_\mathrm{l}, \tau_\mathrm{r}, \tau_\mathrm{t}$ and τ_b, respectively. The superconducting interfaces are modelled by using the generalized BTK model [3, 35, 36] as discussed in **Chapter 4**. To account for all of the possible transport processes, two types of transport channels are considered. First, each pair of electrodes is connected with ideal conductors (graphene channels) showing direct or local transport between the electrodes as shown in Fig. 6.5(a) with solid lines connecting the terminals. The number of transport channels for each of these conductors is accounted by using the parametric conductance $G_{\alpha\beta}$ where α, β denote the terminals. This gives six independent conductances which allow to model the device realistically as it accounts for the asymmetry between the various contact interfaces. The NS connections

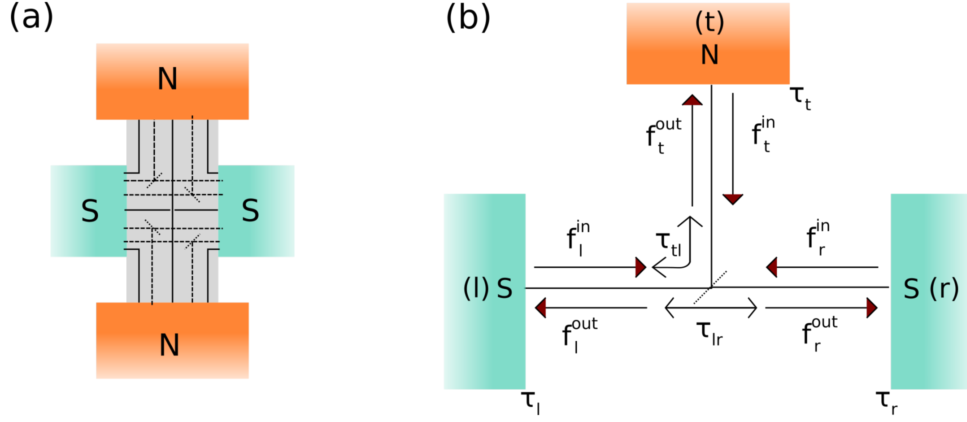

Figure 6.5: (a) Model schematic showing the transport channels. (b) Three-terminal beam splitter as shown in (a) and related distribution functions. (See text for description.)

are modelled by using the modified OTBK model [4], as discussed in **Chapter 4**, where the device has only one superconducting electrode.

Second, nonlocal transport processes involving three terminals are addressed by using three-terminal beam splitters as shown in Fig. 6.5(a) with dashed lines connecting the terminals. Given the geometry of the device, processes involving one N terminal and both of the S terminals are most likely to contribute to the nonlocal transport. In order to keep the simplicity of the model for basic understanding of the nonlocal processes, the model was restricted to the processes where an electron from the N terminal is transmitted to only one of the S terminals (utilising the contact interface asymmetry of the device). For reference, Fig. 6.5(b) shows a beam splitter between the top N terminal and the left S terminal. The transport to the right S terminal takes place only from the left S terminal via the beam splitter. The incoming and outgoing distribution functions shown in the three branches are connected by the beam splitter according to the matrix

$$\begin{pmatrix} f_{\mathrm{l}}^{out} \\ f_{\mathrm{r}}^{out} \\ f_{\mathrm{t}}^{out} \end{pmatrix} = \begin{pmatrix} 0 & 1-r & r \\ 1-r & r & 0 \\ r & 0 & 1-r \end{pmatrix} \begin{pmatrix} f_{\mathrm{l}}^{in} \\ f_{\mathrm{r}}^{in} \\ f_{\mathrm{t}}^{in} \end{pmatrix} \tag{6.1}$$

An additional simplification is made that there is no backscattering from the beam splitter into the left S terminal. It leaves one free parameter r to be chosen. In analogy to the OTBK model, the boundary condition for the distribution functions at the superconducting terminal α held at a chemical potential μ is given as

$$f_{\alpha}^{in}(\epsilon) = T_{\alpha}(\epsilon-\mu_{\alpha})f_0(\epsilon-\mu_{\alpha}) + R_{\alpha}(\epsilon-\mu_{\alpha})f_{\alpha}^{out}(\epsilon) + A_{\alpha}(\epsilon-\mu_{\alpha})(1-f_{\alpha}^{out}(-\epsilon+2\mu_{\alpha})), \tag{6.2}$$

where T_α, R_α and A_α denote the normal transmission, normal reflection and Andreev reflection coefficients as obtained from the BTK model. The boundary condition at the normal terminal γ is given by the same expression as shown in Eqn. 6.2 where $T_\gamma = \tau_\gamma$, $R_\gamma = 1 - \tau_\gamma$ and $A_\gamma = 0$. Combining Eqn. 6.2 with Eqn. 6.1 results in a coupled equation system for the distribution functions. The current in each branch of the beam splitter system can, then, be calculated as

$$I_\alpha = f_{\mathrm{nss}} \frac{G_{\alpha\beta}}{e} \int (f_\alpha^{in} - f_\alpha^{out})\, d\epsilon, \tag{6.3}$$

where $G_{\alpha\beta}$ is the two-terminal NS conductance (G_{tl} in the example shown in Fig. 6.5(b)), and f_{nss} is an additional fit parameter which allows to scale the nonlocal processes relative to the two-terminal local processes. It is to be noted that the beam splitter includes the local processes between the NS and SS terminals, however, they have different weight due to finite transmission of the beam splitter. In particular, the MAR processes between the superconducting terminals are weighed differently. It also includes the nonlocal MAR processes where a local MAR cycle between the superconductors begins due to an initial crossed Andreev reflection.

In the normal state, the model reduces to a conductance matrix as shown below

$$\begin{pmatrix} I_{\mathrm{l}} \\ I_{\mathrm{r}} \\ I_{\mathrm{t}} \\ I_{\mathrm{b}} \end{pmatrix} = \begin{pmatrix} \mathcal{G}_{\mathrm{ll}} & \mathcal{G}_{\mathrm{lr}} & \mathcal{G}_{\mathrm{tl}} & \mathcal{G}_{\mathrm{bl}} \\ \mathcal{G}_{\mathrm{lr}} & \mathcal{G}_{\mathrm{rr}} & \mathcal{G}_{\mathrm{tr}} & \mathcal{G}_{\mathrm{br}} \\ \mathcal{G}_{\mathrm{tl}} & \mathcal{G}_{\mathrm{tr}} & \mathcal{G}_{\mathrm{tt}} & \mathcal{G}_{\mathrm{tb}} \\ \mathcal{G}_{\mathrm{bl}} & \mathcal{G}_{\mathrm{br}} & \mathcal{G}_{\mathrm{tb}} & \mathcal{G}_{\mathrm{bb}} \end{pmatrix} \begin{pmatrix} \mu_{\mathrm{l}} \\ \mu_{\mathrm{r}} \\ \mu_{\mathrm{t}} \\ \mu_{\mathrm{b}} \end{pmatrix} \tag{6.4}$$

where the diagonal elements are given by

$$\mathcal{G}_{\alpha\alpha} = -\textstyle\sum_{\beta\neq\alpha} \mathcal{G}_{\alpha\beta} \tag{6.5}$$

It is to be noted that the conductance parameters $\mathcal{G}_{\alpha\beta}$ are not the same as the $G_{\alpha\beta}$ in Eqn. 6.3. The parameters $\mathcal{G}_{\alpha\beta}$ include the finite transmission probabilities of the interfaces and the additional contributions from the beam splitters. The six independent off-diagonal conductances in Eqn. 6.4 can be determined from the six two-probe resistances $R_{\alpha\beta}$ in the normal state, and then, solving Eqn. 6.4 for $I_\gamma = 0$ and $I_\delta = 0$, where γ and δ denote the floating terminals of the two probe measurement. Note that $R_{\alpha\beta}$ is the resistance between the two terminals and should not be confused with the symbol R_α which denotes the normal reflection at the superconducting terminal. From the $\mathcal{G}_{\alpha\beta}$, the six model parameters can be determined. For instance, if all of the transmission probabilities are fixed, it will give the value of $G_{\alpha\beta}$.

6.3 Bias conditions for the crossed Andreev reflections

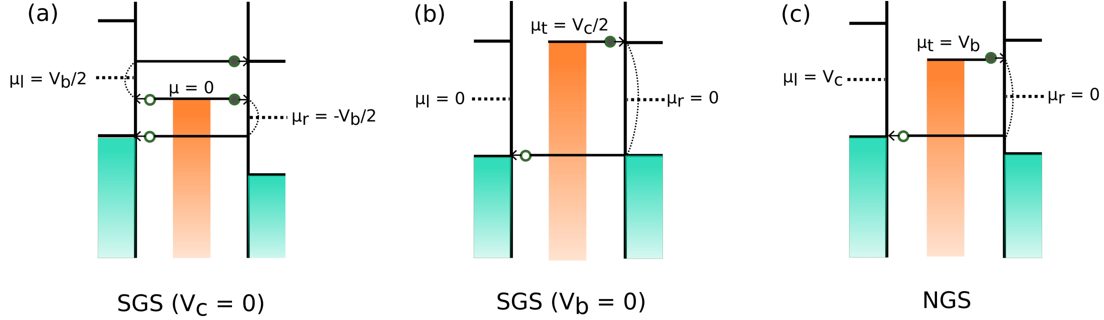

Figure 6.6: Bias conditions for the crossed Andreev reflection in (a) measurement geometry shown in Fig. 6.2(a) in the SGS configuration at $V_c = 0$, and (b) at $V_b = 0$. (c) measurement geometry shown in Fig. 6.2(b) in the NGS configuration. (Filled and empty circles denote electrons and holes, respectively.)

In Fig. 6.6, schematics for the bias conditions are shown that enable the crossed Andreev reflection processes. In the SGS configuration corresponding to Fig. 6.2(a), the threshold for V_b is at $eV_b = 2\Delta/3$ when $V_c = 0$. As shown in Fig. 6.6(a), under these bias conditions, the CAR process is enabled for an electron from the normal metal with an Andreev reflection at the right superconductor, and an inverse CAR for a hole from the normal metal with an Andreev reflection at the left superconductor. As $|V_c| > 0$, these thresholds change as one of it is lowered, the other increases and vice versa. This results in the cross-like feature observed in Fig. 6.8(a) and Fig. 6.10(a) in the region $|eV_b/\Delta| \leq 1$ and $|eV_c/\Delta| \leq 2$. On the other hand, when $eV_c/\Delta \geq 2$ in the SGS configuration, the CAR process is always possible when eV_b is very small, practically close to zero as shown in Fig. 6.6(b), and a conductance peak is observed due to a peak in the Andreev reflection probability at $\epsilon = \Delta$ when the gap features of the two superconductors are aligned. This results in the vertical CAR feature observed in Fig. 6.8(a) and Fig. 6.10(a) at $eV_b/\Delta = 0$ and $|eV_c/\Delta| \geq 2$. In the NGS configuration (Fig. 6.2(b)), the CAR process takes place according to the condition $eV_b + eV_c = \Delta$ as shown in Fig. 6.6(c).

6.4 Observation of the crossed Andreev reflections

As described in the model, the appearance of the crossed Andreev reflection is explained by using the beam-splitter model where the beam-splitter forms due to the difference in the doping density in the graphene channel. It is expected to result in well-pronounced signatures of CAR close to the charge neutrality point of the SGS junction since the NGN junction will be in the low p-doping regime forming pn-junctions or pp′-junction

(due to the different CNP at $V_g = -1.8$ V for NGN junction as compared to $V_g = -2.6$ V for the SGS junction) near the central graphene region as shown in Fig. 6.4.

V_g (V)	G_{lr}	G_{tb}	G_{tl}	G_{tr}	G_{bl}	G_{br}	$\tau_l = \tau_r$	$\tau_t = \tau_b$	f_{nss}	r
-2.7	0*	1.22	3.67	2.38	4.57	6.09	0.72*	0.7*	0.45	0.6*
-5.5	0*	17.52	5.57	4.84	4.63	5.01	0.76*	0.7*	0.73	0.47*

Table 6.1: Parameters used for the modelling of the data. Conductances G are in units of e^2/h. Starred parameters were chosen to model the experimental data, the other parameters were determined from the two-probe resistances of the device in the normal state (shown in Table 6.2). The conductance G_{lr} is set to zero as the conductance between the two S contacts is very low at these gate voltages.

V_g (V)	R_{lr} (kΩ)	R_{tb} (kΩ)	R_{tl} (kΩ)	R_{tr} (kΩ)	R_{bl} (kΩ)	R_{br} (kΩ)
-2.7	5.13	6.86	6.14	6.42	4.83	3.89
-5.5	3.07	1.87	2.79	2.71	2.88	2.66

Table 6.2: Normal state two-probe resistances as measured at 20 mK, 50 mT and $V_b = V_c = 0$.

Fig. 6.7(a), (b) and (c) show the line traces of the differential conductance dI_b/dV_b map shown in Fig. 6.3(a) (measured at V_g = -2.7 V, T =20 mK and $B = 0$) at $eV_c/\Delta = 0, \approx 2$ and ≈ 4, respectively, along with the dI_b/dV_b curves generated with the model. The parameters used for the modelling are shown in Table 6.1. The transmission probability for the graphene/superconductor interfaces (τ_l and τ_r) is chosen to be 0.72 while it is chosen to be 0.7 for graphene/normal metal interfaces (τ_t and τ_b). It can be readily seen that the model provides a good comparison with the experimental data. An important point of consideration is that G_{lr} is set to zero which denotes the transport across the SGS channel. The reason is that the SGS channel at this gate voltage is close to the Dirac point, and hence the normal state resistance is very high which results in negligible direct conductance across the channel. In this scenario, the transport through the NS corners is more likely to be an effective way of charge transport as can be seen in Table. 6.1. Therefore, the transport across the SGS channel in this regime is addressed by using the beam splitters which account for both, the MAR and the CAR, processes.

Fig. 6.8(a) shows the experimental dI_b/dV_b map as shown in Fig. 6.3(a), which can be compared with the dI_b/dV_b map generated with the model as shown in Fig. 6.8(b). Comparing the two dI_b/dV_b maps, it can be clearly seen that the the features in the experimental data can be very well generated with the model. For the interpretation of the observed features, Fig. 6.8(c) shows the same map as shown in Fig. 6.8(b), with the guidelines. As discussed before, the vertical lines (orange in Fig. 6.8(c)) appearing at $eV_b/\Delta = \pm 1$ and ± 2 are due to the MAR which show the transport between the superconducting contacts through the graphene channel. The intersecting lines (green

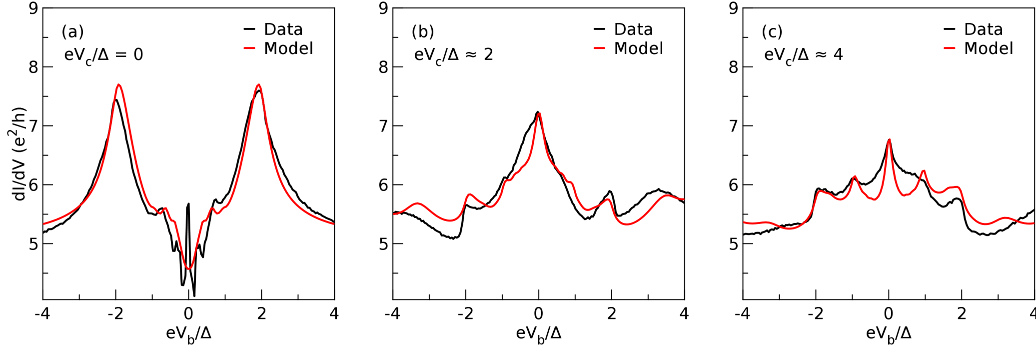

Figure 6.7: Line traces of the $dI_\mathrm{b}/dV_\mathrm{b}$ map shown in Fig. 6.3(a) at V_g = -2.7 V, T = 20 mK, $B = 0$, and the curves generated with the model for the same measurement conditions at (a) $eV_\mathrm{c}/\Delta = 0$, (b) $eV_\mathrm{c}/\Delta \approx 2$, and (c) $eV_\mathrm{c}/\Delta \approx 4$.

in Fig. 6.8(c)) that form the diamond-like feature are due to the transport between the N and S contacts along the corners of the graphene channel. The dotted green lines in Fig. 6.8(c) show the spread of energy for the electronic transport along the NS corners in the presence of asymmetry in graphene/metal contact interfaces. This asymmetric coupling of the contacts, which can be observed in the conductance values in Table 6.1, can be readily seen in the two probe resistances as shown in Table 6.2. This asymmetry results in the splitting of the intersecting green lines and marks the region shown by the dotted green lines. This splitting of the intersecting lines can be clearly seen in Fig. 6.8(a). The feature that appears at $eV_\mathrm{b}/\Delta = \pm 2/3$ when $eV_\mathrm{c}/\Delta = 0$ and evolves into a cross-like feature in the region $|eV_\mathrm{b}/\Delta| \leq 1$ and $|eV_\mathrm{c}/\Delta| \leq 2$ is attributed to the CAR process as shown in Fig. 6.6(a). The vertical feature appearing at $eV_\mathrm{b}/\Delta = 0$ and $|eV_\mathrm{b}/\Delta| \geq 2$ is also linked to the CAR process as shown in Fig. 6.6(b).

Fig. 6.8(d) shows the experimental $dI_\mathrm{c}/dV_\mathrm{b}$ map as shown in Fig. 6.3(b) for the NGS configuration. It can be compared with the $dI_\mathrm{c}/dV_\mathrm{b}$ map generated with the model as shown in Fig. 6.8(e) with the same modelling parameters as used for the SGS configuration. It is to be noted that in the NGS configuration, the experimental measurement is two-probe instead of the pseudo four-probe as in the SGS configuration, and hence includes the series resistances from the RC filters. Therefore, the comparison between the experimental data and the model is only qualitative in the NGS configuration. To interpret the observed experimental data, Fig. 6.8(f) shows the modelling data with the guidelines. In order to distinguish the two S terminals, one in the bias junction (NGS) and the other in the control channel (SGS) which is outside of the bias circuit (as shown in Fig. 6.2(b)), the S terminal outside of the NGS bias channel is referred to as S′ for the sake of clarity in the interpretation.

As shown in Fig. 6.8(f) and can be compared to Fig. 6.8(d), the transport in this configuration is attributed to four processes. Slightly tilted vertical lines (green in

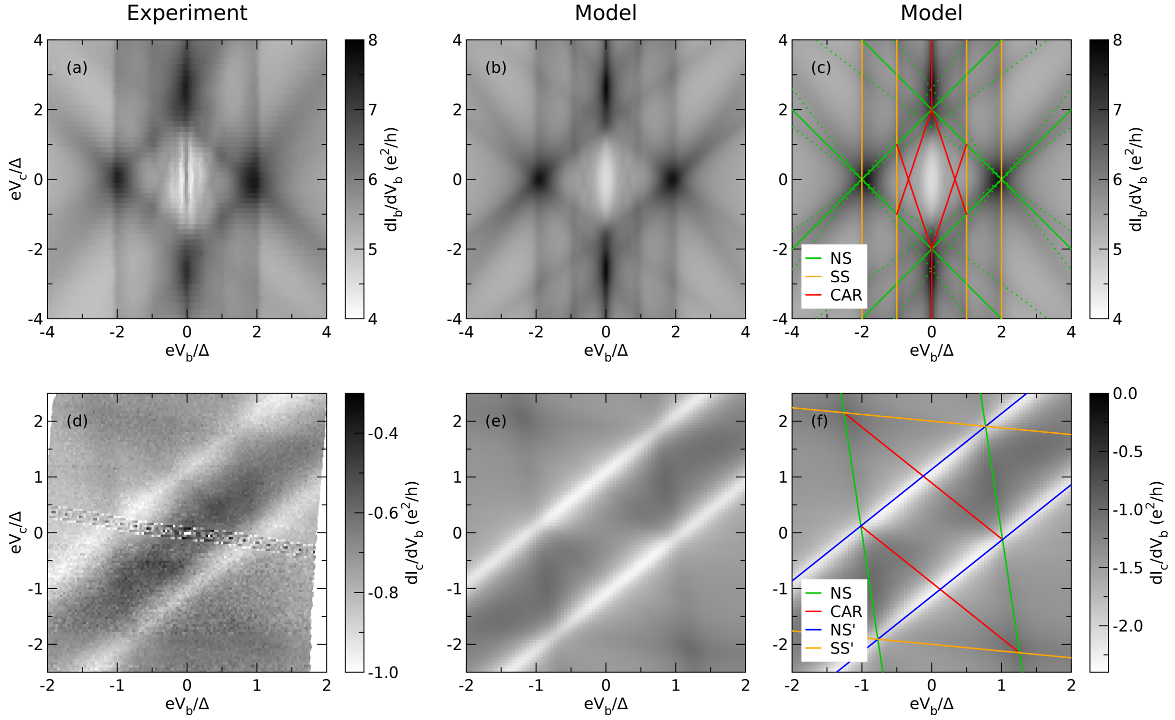

Figure 6.8: (a) Experimental $dI_\mathrm{b}/dV_\mathrm{b}$ map in the SGS configuration (as shown in Fig. 6.3(a)) at V_g = -2.7 V, T = 20 mK, B = 0. (b) and (c) show the $dI_\mathrm{b}/dV_\mathrm{b}$ map without and with the guidelines, respectively, obtained from the model for the measurement conditions in (a). (d) Experimental $dI_\mathrm{c}/dV_\mathrm{b}$ in the NGS configuration (as shown in Fig. 6.3(b)) under the same measurement conditions as in (a). (e) and (f) show the $dI_\mathrm{c}/dV_\mathrm{b}$ map without and with the guidelines, respectively, obtained from the model for this measurement configuration.

Fig. 6.8(f)) correspond to the transport between the biased NGS channel. The backward slope in these lines is due to the series resistances from the filters and implies that the bias sources are not perfectly stiff. It also results in the cross-talk between V_b and V_c of about 12% which has been taken into account in the model. The nearly horizontal lines (orange in Fig. 6.8(f)) are due to the direct transport across the SGS′ junction which is the control channel in this measurement geometry. It appears due to the cross talk between V_b and V_c. It also leads to a small ac modulation of the voltage along the control channel. The diagonal lines (blue) show the transport across the NGS′ channel. It is modulated backwards, and hence it has a negative contribution. In this case too, the lines shown in red in Fig. 6.8(f), which can be clearly seen in Fig. 6.8(d), are due to the CAR process as shown in Fig. 6.6(c) for the NGS configuration.

It was shown in Fig. 6.3(c) and (d) that similar measurements were carried out at V_g =-5.5 V in the p-doped regime. Fig. 6.9(a), (b) and (c) show the line traces of the $dI_\mathrm{b}/dV_\mathrm{b}$ map in the SGS configuration, as shown in Fig. 6.3(c), at $eV_\mathrm{c}/\Delta = 0, \approx 2$

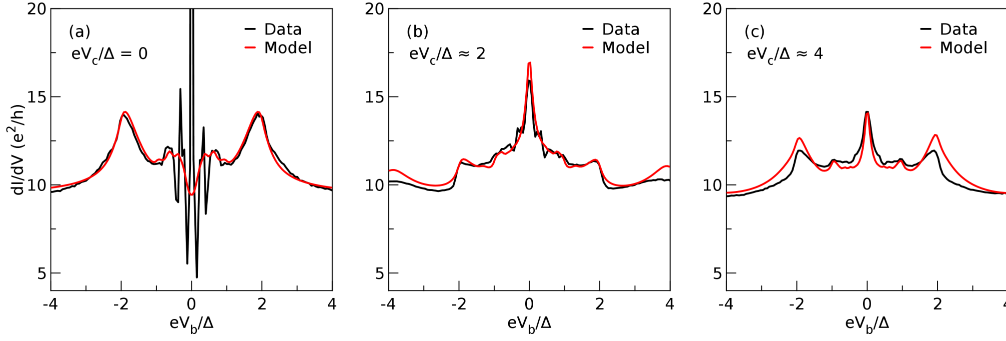

Figure 6.9: Line traces of the $dI_\mathrm{b}/dV_\mathrm{b}$ map shown in Fig. 6.3(c) at V_g = -5.5 V, T = 50 mK, B = 0, and the curves generated with the model for the same measurement conditions at (a) $eV_\mathrm{c}/\Delta = 0$, (b) $eV_\mathrm{c}/\Delta \approx 2$, and (c) $eV_\mathrm{c}/\Delta \approx 4$.

and $\approx$ 4 along with the curves generated with the model. The parameters used for modelling the experimental data are as shown in Table 6.1. The transmission probability is chosen to be 0.76 for the graphene/superconductor interfaces (τ_l and τ_r) and 0.7 for graphene/normal metal interfaces (τ_t and τ_b). In Fig. 6.9(a), the additional peaks and dips in the conductance close to $eV_\mathrm{b}/\Delta = 0$ (due to the superconducting dip in resistance and self-induced Shapiro-like features) are not captured with the model, however, a good comparison between the experimental data and the model can be seen for the other features as well as for the data shown in Fig. 6.9(b) and (c).

Fig. 6.10(a) and (b) show the experimental $dI_\mathrm{b}/dV_\mathrm{b}$ map (as shown in Fig. 6.3(c) at V_g = -5.5 V) and the map generated with the model, respectively, in the SGS configuration. Fig. 6.10(c) shows the modelling data with the guidelines. It can be readily seen in the experimental data that the CAR features (red lines in Fig. 6.10(c)) are still present, however, it is not clearly distinguishable from the self induced Shapiro-like feature and high conductance in the zero bias regime due to the supercurrent. The MAR features (orange lines in Fig. 6.10(c)) can be observed at $eV_\mathrm{b} = \pm 1$ and ± 2. A clear difference between Fig. 6.10 (V_g = -5.5 V) and Fig. 6.8 (V_g = -2.7 V) is in the diamond-like pattern (green and dotted green lines in Fig. 6.8(c) and green lines in Fig. 6.10(c)). As explained before, this pattern appears due to the transport along the NGS corners and it splits in the presence of asymmetry in the coupling of the contacts. This diamond-like pattern is not split at the present gate voltage $V_\mathrm{g} = -5.5$ V contrary to the pattern observed in the vicinity of the Dirac point. It suggests that the device has relatively homogeneous coupling of the contacts at this gate voltage which is also clear from the conductance values shown in Table 6.1, and the two-probe resistances shown in Table 6.2. It can also be seen from Table 6.1 that the conductance G_tb (conductance between the N contacts) is quite high. This could indicate that the pn-junctions forming in the vicinity of the graphene/superconducting interfaces aid transport between the N contacts.

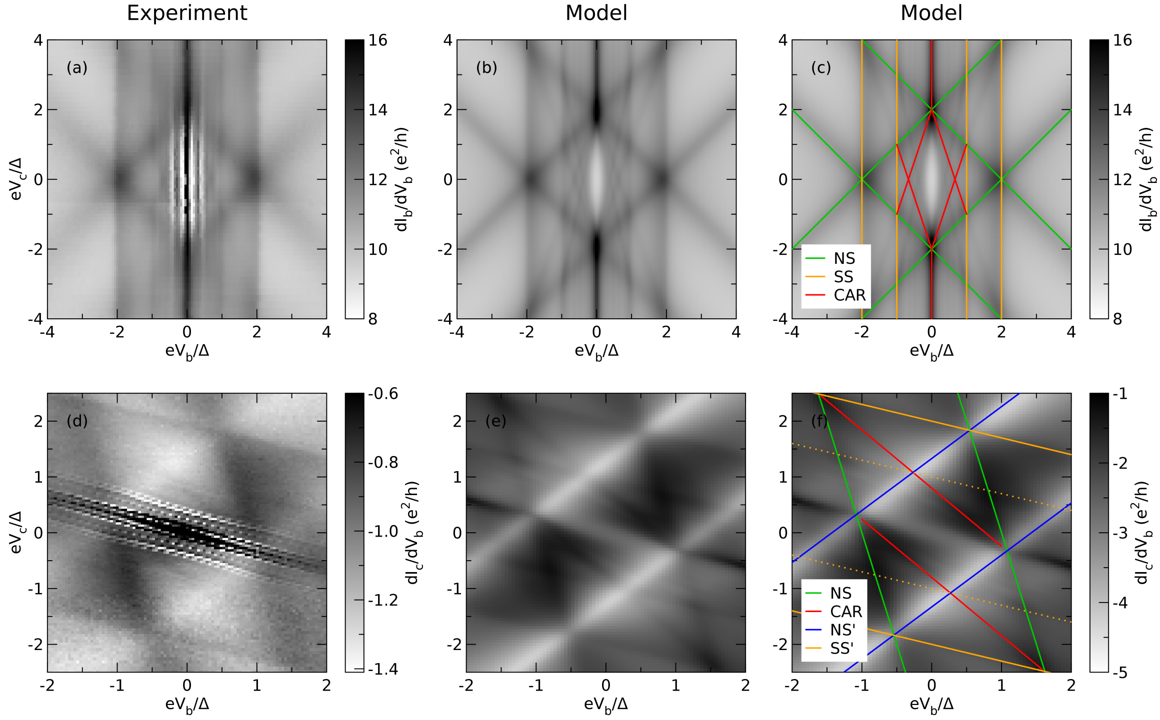

Figure 6.10: (a) Experimental local differential conductance dI_b/dV_b map in the SGS configuration (as shown in Fig. 6.3(c)) at V_g = -5.5 V, T = 50 mK, B = 0. (b) and (c) show the dI_b/dV_b map without and with the guidelines, respectively, obtained from the model for the measurement conditions in (a). (d) Experimental nonlocal differential conductance dI_c/dV_b in the NGS configuration (as shown in Fig. 6.3(d)) under the same measurement conditions as in (a). (e) and (f) show the dI_c/dV_b map without and with the guidelines, respectively, obtained from the model for this measurement configuration.

Fig. 6.10(d) shows the experimental dI_c/dV_b map as shown in Fig. 6.3(d) in the NGS configuration at $V_g = -5.5$ V. Fig. 6.10(e) and (f) show the map generated with the model with and without the guidelines, respectively. As observed in the nonlocal conductance at V_g = -2.7 V in this configuration (Fig. 6.8(d)-(f)), the four transport processes can also be observed in Fig. 6.10(d)-(f) at V_g = -5.5 V: the transport across the biased NGS channel (slightly tilted vertical green lines), the transport across the SGS′ channel (nearly horizontal orange and dotted orange lines showing the MAR at 2Δ and Δ), the transport across the NGS′ channel (diagonal blue lines), and faint signatures of CAR (slanting red lines). Since the resistance of the device is lower at V_g = -5.5 V compared to V_g = -2.7 V (close to the Dirac point), the cross-talk between the bias and control voltages is larger. It results in the increased slope of the transport features in Fig. 6.10 (V_g = -5.5 V) as compared to Fig. 6.8 (V_g = -2.7 V).

6.5 Gate dependence of the crossed Andreev reflections

As discussed in the previous section, the CAR features and their visibility depend on the gate voltage. While these features can be very clearly observed close to the Dirac point, they become significantly fainter in the high doping regime due to the supercurrent and self induced Shapiro-like features. In the present section, the evolution of the CAR features is traced as a function of the gate voltage V_g in the SGS measurement configuration as shown in Fig. 6.2(a).

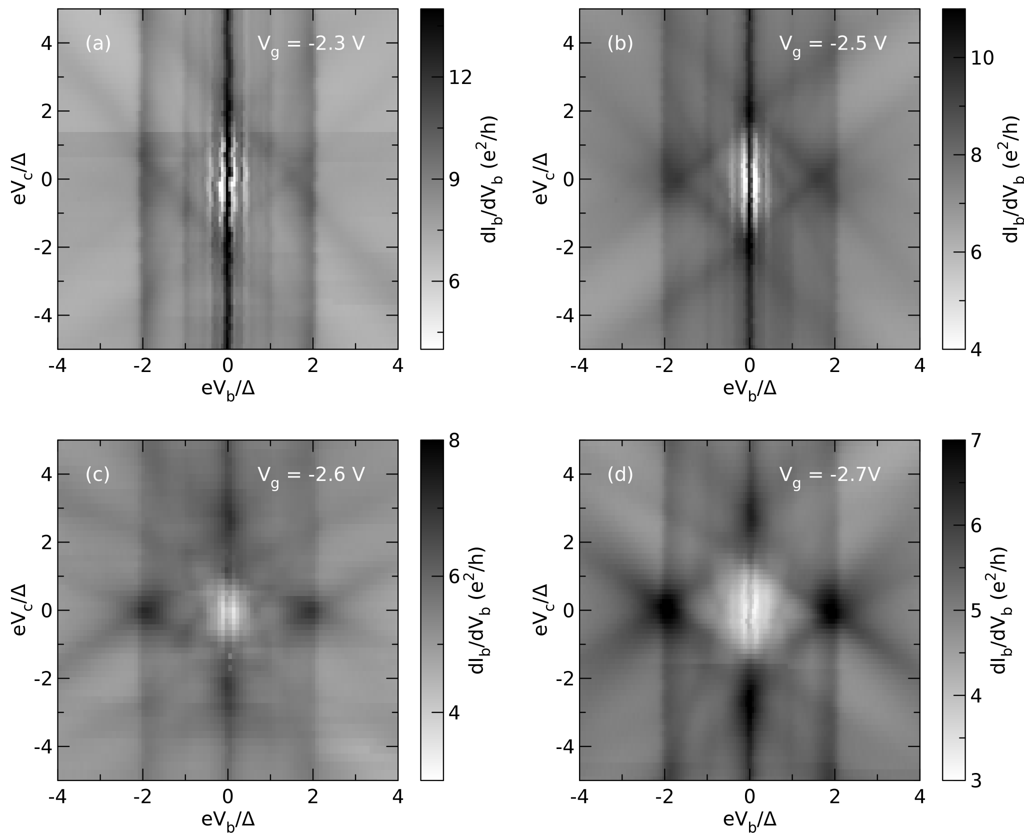

Figure 6.11: Differential conductance map across the SGS junction as a function of V_b and V_c, both normalized with the superconducting gap energy, measured in the vicinity of the charge neutrality point at (a) V_g = -2.3 V, (b) V_g = -2.5 V, (c) V_g = -2.6 V, (d) V_g = -2.7 V showing the evolution of the observed CAR.

Since the CAR features were clearly distinguishable in the vicinity of the SGS Dirac point as seen in Fig. 6.8(a) and (d), Fig. 6.11 shows a series of the differential conductance $dI_\mathrm{b}/dV_\mathrm{b}$ maps measured in the vicinity of the SGS Dirac point. Fig. 6.11(a), (b), (c) and (d) show the experimental results at V_g = -2.3, -2.5, -2.6 and -2.7 V, respectively, measured at 50 mK and zero magnetic field. The MAR features appearing as vertical

lines at $eV_\mathrm{b}/\Delta = \pm 1$ and ± 2 can be observed at all of the gate voltages, however, the diamond-like feature coming from the transport along the NGS corners as well as the CAR feature change significantly in this gate voltage range. The intersecting lines creating the diamond-like feature are not split at V_g = -2.3 V, they are weakly split at V_g = -2.5 V, and they are strongly split at V_g = -2.6 V and -2.7 V. As the splitting of these lines is related to the asymmetry in the coupling of the contacts, it suggests that the charge transport in the device is highly asymmetric close to the Dirac point of the SGS junction while it is relatively symmetric everywhere else. Regarding the observation of CAR, the features (cross-like features in the region $|eV_\mathrm{b}/\Delta| \leq 1$ and $|eV_\mathrm{c}/\Delta| \leq 2$, and vertical line at $eV_\mathrm{b} = 0$ and $|eV_\mathrm{c}/\Delta| \geq 2$) are not distinguishable at V_g = -2.3 V due to the supercurrent and the self induced Shapiro-like steps, while they are weakly distinguishable at V_g = -2.5 V and clearly distinguishable at V_g = -2.6 V and -2.7 V. It can be concluded form these measurements that in this device, the CAR features cannot be clearly distinguished in the presence of a large supercurrent. It was shown in **Chapter 5, section 5.4.1** that a critical current magnitude of 80 nA and $\sim$50 nA was measured in this device at V_g = 10 V and 0 V, respectively. There was no observable supercurrent close to the SGS Dirac point and only a dip in the resistance was observed in the p-doped regime. However, as seen in Fig. 6.11(a) at V_g = -2.3 V, the weak residual superconductivity in graphene still hinders the visibility of the CAR features. It restricts the measurement window of CAR features in this device to a very small gate voltage range in the p-doped regime while the observation in the n-doped regime is not possible due to a high supercurrent despite the formation of nn′ junctions which might also act as the beam splitters. In addition, it should be noted that the potential barriers in the nn′ region might be different from the pn-junctions or the pp′-junctions, and this could also modify the transport across the graphene channel with regard to the Klein tunnelling [9, 10, 68].

Fig. 6.12(a)-(f) show the $dI_\mathrm{b}/dV_\mathrm{b}$ maps measured in the p-doped region in the SGS configuration at V_g = -2.85, -3.25, -3.5, -4.5, -5.5 and -10 V, respectively, at 50 mK and zero magnetic field. The MAR features appearing at $eV_\mathrm{b}/\Delta = \pm 1$ and ± 2 can be observed in all of the maps. As seen previously in Fig. 6.11(c) and (d), the intersecting lines forming the diamond-like feature (transport along the NGS corners) are clearly split at V_g = -2.85 V (Fig. 6.12(a)) which is close to the CNP. However, these features become homogeneous with the increasing negative V_g, as seen in Fig. 6.12(b) - (f). It is in agreement with the argument that the device has higher contact asymmetry close to the CNP while it is relatively symmetric far from the CNP. Looking at the CAR features, they are most prominent at V_g = -2.85 V and -3.25 V, Fig. 6.12(a) and (b), respectively. These features are visible in Fig. 6.12(c) and (d) corresponding to V_g = -3.5 V and -4.5 V, respectively, along with the vertical superconducting feature at $eV_\mathrm{c}/\Delta = 0$ and the accompanying self induced Shapiro-like features in the region $|eV_\mathrm{b}/\Delta| \leq 1$. However, the CAR features are faintly visible in Fig. 6.12(e) corresponding to V_g = -5.5 V (same data as

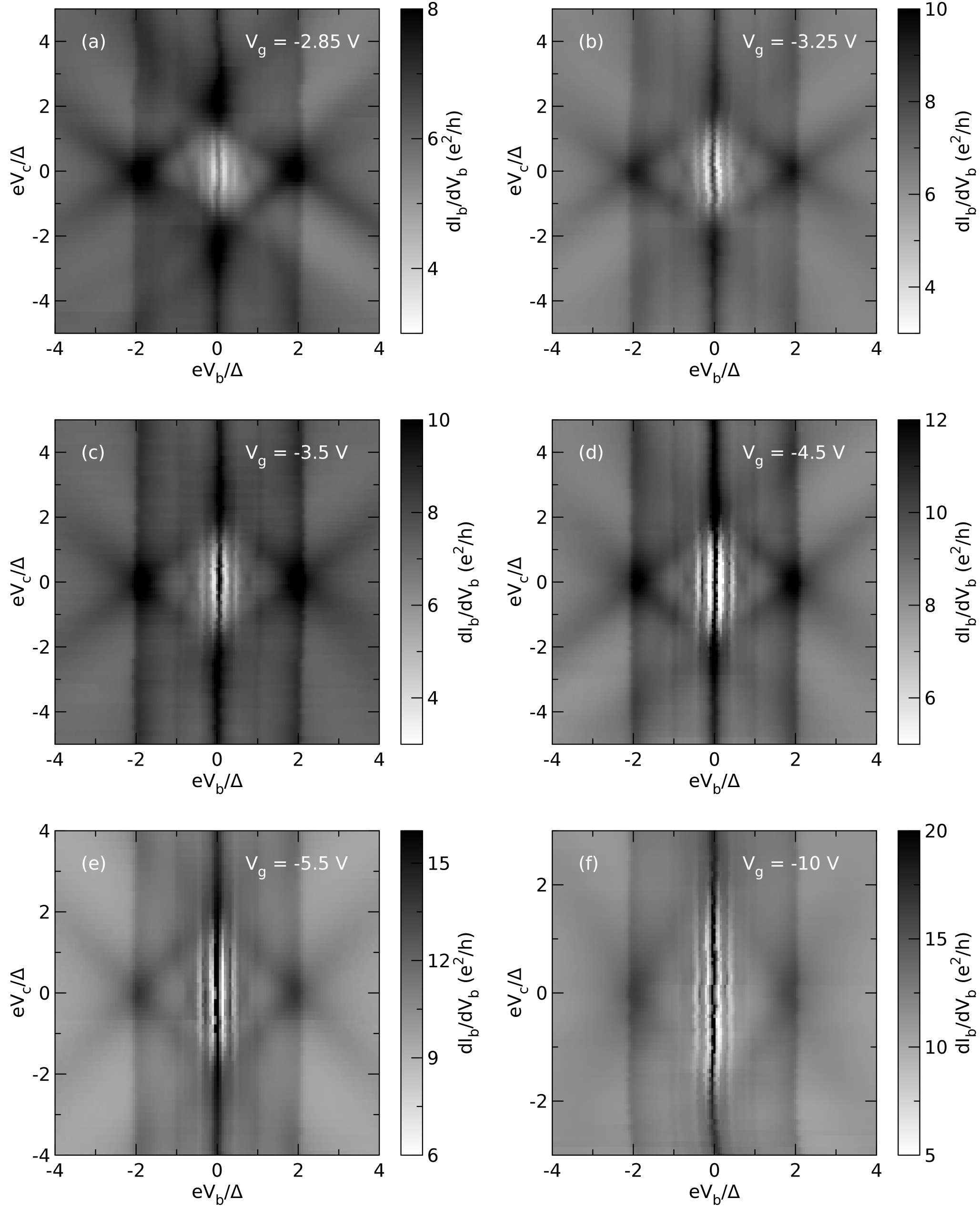

Figure 6.12: Differential conductance map across the SGS junction as a function of eV_b/Δ and V_c/Δ measured in the p-doped region at $B = 0$, $T = 50\,\mathrm{mK}$, and (a) V_g = -2.85 V, (b) V_g = -3.25 V, (c) V_g = -3.5 V, (d) V_g = -4.5 V, (e) V_g = -5.5 V, and (f) V_g = -10 V showing the evolution of CAR.

in Fig. 6.10(a) which is shown here for completeness), they cannot be seen in Fig. 6.12(f) corresponding to V_g = -10 V (highly p-doped region) due to the higher conductance at this gate voltage and relatively stronger dip in the resistance appearing at zero V_b. The vertical CAR feature appearing at $eV_\mathrm{b}/\Delta = 0$ in the region $|eV_\mathrm{c}/\Delta| \geq 2$ is present in all of the maps. This feature can be clearly observed in Fig. 6.12(a) where V_g is close to the V_CNP of the SGS channel, and therefore, the supercurrent and the Shapiro-like features are weak in this regime. In the successive maps, from Fig. 6.12(b) - (f), this feature is present along with the supercurrent feature in the zero V_b regime.

6.6 Temperature dependence of the crossed Andreev reflections

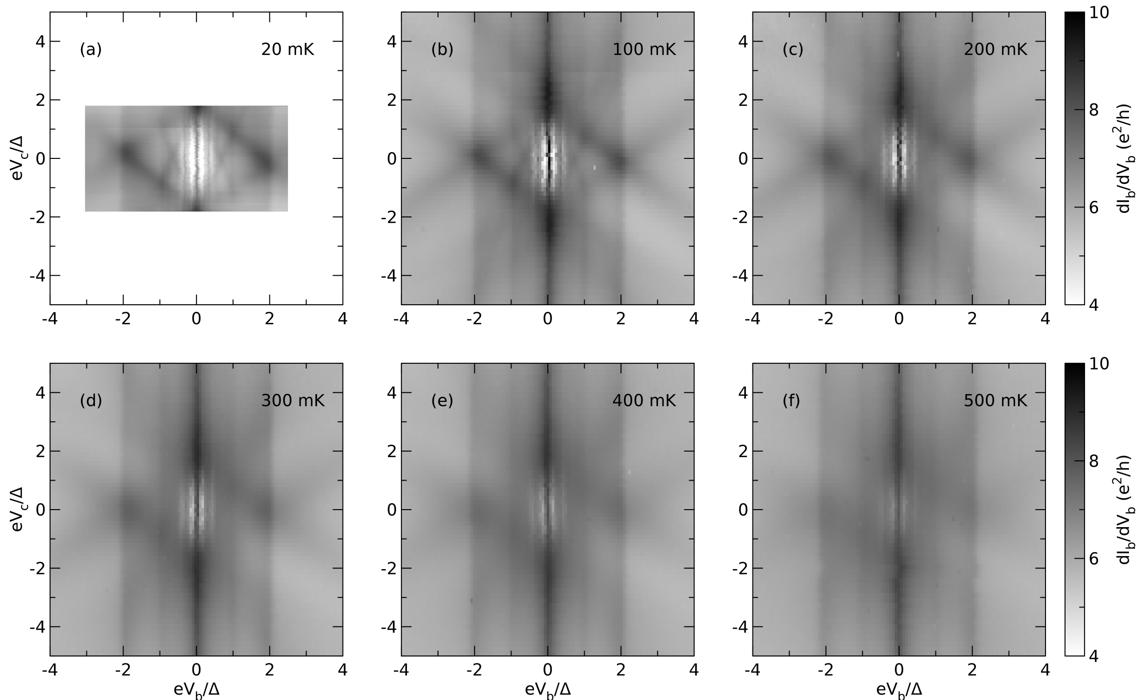

Figure 6.13: Differential conductance map across the SGS junction as a function of eV_b/Δ and eV_c/Δ measured in the vicinity of the charge neutrality point at V_g = -2.68 V, B = 0 and (a) T = 20 mK (Measurement was conducted in a reduced V_b and V_c range.), (b) T = 100 mK, (c) T = 200 mK, (d) T = 300 mK, (e) T = 400 mK, and (f) T = 500 mK showing the dependence of CAR on temperature.

As the Andreev processes originate due to the normal metal/superconductor transport, they strongly depend on the properties of the superconductor, especially, the superconducting gap. Increasing temperature results in the decrease of the superconducting gap

which also changes the energy scale of the Andreev processes. Therefore, it is essential to study the evolution of the CAR features with the increasing temperature.

As the superconducting electrode in these devices is made of Ti/Al, a critical temperature T_C of $\sim 900\,$mK was observed. Fig. 6.13(a)-(f) show the differential conductance dI_b/dV_b maps measured in the SGS configuration at V_g = -2.6 V (close to the CNP where clear CAR features were observed as shown in Fig. 6.11(c)) under zero magnetic field and at a base temperature T = 20, 100, 200, 300, 400 and 500 mK, respectively. Fig. 6.13(a) shows the clearly visible cross-shaped CAR features at 20 mK which are slightly broader and less prominent at 100 mK. It is to be noted that the measurement at 20 mK was conducted in a reduced V_b and V_c range which accounts for the missing data in the map. These features can still be seen as a weak shadow at 200 mK, however, they become completely obscure at 300 mK and cannot be seen in Fig. 6.13(d), (e) and (f). It is to be noted that the observed superconducting gap changed by mere 13 μeV from 130 μeV at 20 mK to 117 μeV at 500 mK. This behaviour of the cross-shaped CAR feature can be attributed to the thermal broadening because of which, a small change in conductance due to the CAR features is overshadowed by the background conductance. This renders the CAR features indistinguishable from the background. The other CAR feature which appears as a vertical conductance ridge at $eV_b/\Delta = 0$ for $|eV_c/\Delta| \geq 2$ is robust against temperature change and can be clearly seen upto 500 mK. A valid reason for its robustness is that the conditions for its appearance are always satisfied as long as the device is in the superconducting state (shown in Fig. 6.6(b), section 6.3). An additional detail is the diamond-like feature which becomes less prominent with increasing temperature, however, it can still be observed in Fig. 6.13(f) at 500 mK. Further temperature dependence of these features with regard to the T_C of the device could not be measured as the base temperature of the dilution refrigerator is not stable enough in the desired range of 500 mK$< T <$900 mK.

6.7 Conclusion

To conclude, the crossed Andreev reflection process was investigated in a multiterminal graphene device with two transverse junctions, namely the SGS and NGN junctions. Clear signatures of CAR were observed in the four-terminal measurment geometry (SGS junction as the bias junction and NGN junction as the control junction) as well as in the three-terminal measurement geometry (NGS junction as the bias junction and SGS junction as the control junction). The CAR features were explained by using a beam splitter model along with the modified OTBK and generalized BTK models. Since the CAR features appear in the same biasing regime as the supercurrent and self induced Shapiro-like features, their visibility is affected by the latter features. The CAR features were found to be most prominent in the vicinity of the charge neutrality point of the SGS junction due to very weak superconductivity in this regime. These features were

observed in the p-doped regime as well, however, they become less prominent with higher negative gate voltage (higher doping density resulting in higher conductance of the device makes the features indistinguishable from the conductance background). Temperature dependence of the CAR features revealed that the two features (cross-like feature and vertical ridge-like feature in SGS measurement configuration) have different response to increasing temperature. While the cross-like feature becomes indistinguishable from the background conductance between 200 to 300 mK, the vertical ridge-like feature can be observed easily till 500 mK (Note that the superconducting critical temperature of the device is $\sim$900 mK).

It is to be noted that the multiterminal device which was employed to study the nonlocal Andreev reflection, takes advantage from its simple geometrical configuration of having a Josephson junction with a longer transverse normal metal junction. Due to the apparent as well as expected difference in the gate coupling efficiency of the two junctions, different doping densities across the graphene channel generate efficient beam splitting interfaces. This process can be loosely correlated to the report by Cayssol [117] where the author had addressed Cooper-pair splitting in n-type graphene/proximitized graphene/p-type graphene by using the relativistic band structure of graphene. The results presented here open the way to study quantum entanglement in these highly tunable graphene based hybrid junction devices.

Chapter 7

Summary and outlook

During the course of this thesis, the goal was to study the proximity induced superconductivity and Andreev reflection processes in encapsulated graphene based devices with hybrid edge contacts.

As the first step in this direction, simple two-terminal devices were fabricated where a single graphene layer (SLG) was encapsulated between two h-BN crystallites, and connected to a normal metal (Ti/Cu/Al) electrode on one edge and a superconducting (Ti/Al) electrode on the other parallel edge. This gives a device configuration of NGN′ (graphene connected to two different normal metals) in the normal state, *i. e.*, above the critical temperature of the superconductor. In this configuration, the asymmetry of the two graphene/metal contacts was clearly reflected in the Fabry-Pérot pattern. To analyse and explain the electronic transport properties of these devices in the superconducting regime (NGS configuration), modified OTBK and generalized BTK models were employed [3, 4, 35, 36]. It was shown that the signature of ballistic transport, *i. e.*, the Fabry-Pérot resonances, could be very well observed in the Andreev reflections as the oscillations in the transmission probability of the graphene/superconductor interface. While these Fabry-Pérot resonances are usually observed in graphene based Josephson junctions as a small modulation in the magnitude of the supercurrent [16–19, 23, 25], it is the first report on edge-connected NGS devices where this phenomenon was observed.

Building on the experimental results obtained from the two-terminal NGS devices, multiterminal graphene based devices were fabricated. In these devices, h-BN encapsulated SLG was connected to two superconducting electrodes (Ti/Al) on two parallel edges, and to two normal metal electrodes (Ti/Cu/Al) on the other two edges. Due to this geometry, these devices have two transverse junctions, the SGS junction (Josephson junction with graphene weak link) and the NGN junction. In this device configuration, the electronic transport through one junction can be tuned by applying a control voltage/current across the other junction [103–107]. Ballistic charge transport was observed in these devices across the SGS junction in the normal state. In addition to the gate tunability

of the supercurrent across the SGS junction, it was shown that the magnitude of the supercurrent can be significantly tuned by applying the control current across the NGN junction. The magnitude of the control current required to diminish the supercurrent was found to depend on the magnitude of the supercurrent, *i. e.*, a smaller supercurrent would require a smaller control current to bring the device into the normal state. While this kind of device geometry is apt to observe the π-junction behavior [103–106], this phenomenon was not observed in the measured devices.

These multiterminal graphene based junctions also open the possibility to study the nonlocal transport processes in the superconducting state due to the combination of normal metal and superconducting electrodes. An analytical model based on the modified OTBK and generalized BTK models was employed to explain the various transport processes in the superconducting regime. The signatures of crossed Andreev reflection were observed, and explained with a beam splitter model involving both of the superconducting electrodes and one normal metal electrode. The visibility of the observed CAR features was found to strongly depend on the conductance of the graphene weak link and the magnitude of the supercurrent. It is to be noted that both of these quantities, conductance of the graphene weak link and the magnitude of the supercurrent, are tuned by an applied gate voltage. The CAR features were found to be clearly visible in the vicinity of the Dirac point of the SGS channel due to very low conductance of the graphene weak link in this regime. Temperature dependent study of the CAR features in this region showed that the observed features have different response to the temperature. One of the CAR feature becomes obscure (indistinguishable from the conductance background) between 200 - 300 mK while the other remains robust upto 500 mK.

To conclude, it has been shown that the graphene based junctions with hybrid contacts offer interesting possibilities to study Andreev processes. These junctions take advantage of the gate tunability of graphene which tunes the Andreev processes as well. It suggests strong possibilities for such kind of devices in terms of fundamental physics as well as their potential applications in quantum entanglement. A simple approach will be to study these multiterminal devices using a bilayer graphene (BLG) instead of the single layer since the electronic properties of these two systems are significantly different from each other [10]. In contrast to SLG, an electrostatically induced bandgap can be opened in BLG which provides an additional control knob on the charge transport. In addition, it also provides an opportunity to observe the specular Andreev reflection which is relatively harder to observe in SLG due to the strong fluctuations in the Fermi energy close to the Dirac point. Apart from this, another fascinating field will be to use ferromagnetic electrodes instead of the normal metal electrodes in these junctions. It is expected to give a pure nonlocal spin current signal in this transverse junction geometry due to the spin selectivity of the ferromagnetic electrode and Cooper pair transport in the superconducting electrode [119]. In this case too, the SLG and BLG systems might offer

different response, however, both of them will open up the possibility of electrostatically tunable spin valves with spin-selected Andreev processes.

Bibliography

[1] B. D. Josephson. “Possible new effects in superconductive tunnelling”. In: *Phys. Lett.* 1 (1962), p. 251.

[2] A. F. Andreev. “The Thermal Conductivity of the Intermediate State in Superconductors”. In: *Sov. Phys. JETP* 19 (1964), p. 1228.

[3] G. E. Blonder, M. Tinkham, and T. M. Klapwijk. “Transition from metallic to tunneling regimes in superconducting microconstrictions: Excess current, charge imbalance, and supercurrent conversion”. In: *Phys. Rev. B* 25 (1982), p. 4515.

[4] M. Octavio et al. “Subharmonic energy-gap structure in superconducting constrictions”. In: *Phys. Rev. B* 27 (1983), p. 6739.

[5] M. Tinkham. *Introduction to Superconductivity.* Courier Dover, 2012.

[6] T. M. Klapwijk. “Proximity effect from an Andreev perspective”. In: *J. Supercond.* 17 (2004), p. 593.

[7] C. W. J. Beenakker. “Specular Andreev reflection in graphene”. In: *Phys. Rev. Lett.* 97 (2006), p. 067007.

[8] M. Titov, A. Ossipov, and C. W. J. Beenakker. “Excitation gap of a graphene channel with superconducting boundaries”. In: *Phys. Rev. B* 75 (2007), p. 045417.

[9] C. W. J. Beenakker. “Andreev reflection and Klein tunneling in graphene”. In: *Rev. Mod. Phys.* 80 (2008), p. 1337.

[10] M. I. Katsnelson. *Graphene: Carbon in Two Dimensions.* Cambridge University Press, 2012.

[11] A. H. Castro Neto et al. “The electronic properties of graphene”. In: *Rev. Mod. Phys.* 81 (2009), p. 109.

[12] F. Schwierz. “Graphene transistors”. In: *Nat. Nanotechnol.* 5 (2010), p. 487.

[13] W. Han et al. “Graphene spintronics”. In: *Nat. Nanotechnol.* 9 (2014), p. 794.

[14] E. V. Castro et al. “Biased Bilayer Graphene: Semiconductor with a Gap Tunable by the Electric Field Effect”. In: *Phys. Rev. Lett.* 99 (2007), p. 216802.

[15] G.-H. Lee and H.-J. Lee. “Proximity coupling in superconductor-graphene heterostructures”. In: *Rep. Prog. Phys.* 81 (2018), p. 056502.

[16] V. E. Calado et al. “Ballistic Josephson junctions in edge-contacted graphene”. In: *Nat. Nanotech.* 10 (2015), p. 761.

[17] M. Ben Shalom et al. “Quantum oscillations of the critical current and high-field superconducting proximity in ballistic graphene”. In: *Nat. Phys.* 12 (2016), p. 318.

[18] F. Amet et al. “Supercurrent in the quantum Hall regime”. In: *Science* 352 (2016), p. 966.

[19] I. V. Borzenets et al. “Ballistic Graphene Josephson Junctions from the Short to the Long Junction Regimes”. In: *Phys. Rev. Lett.* 117 (2016), p. 237002.

[20] M. J. Zhu et al. “Edge currents shunt the insulating bulk in gapped graphene”. In: *Nat. Commun.* 8 (2017), p. 14552.

[21] M. T. Allen et al. “Observation of electron coherence and Fabry-Perot standing waves at a graphene edge”. In: *Nano Lett.* 17 (2017), p. 7380.

[22] G. Nanda et al. “Current-phase relation of ballistic graphene Josephson junctions”. In: *Nano Lett.* 17 (2017), p. 3396.

[23] M. Zhu et al. “Supercurrent and multiple Andreev reflections in micrometer-long ballistic graphene Josephson junctions”. In: *Nanoscale* 10 (2018), p. 3020.

[24] J. Park et al. “Short ballistic Josephson coupling in planar graphene junctions with inhomogeneous carrier doping”. In: *Phys. Rev. Lett.* 120 (2018), p. 077701.

[25] R. Kraft et al. “Tailoring supercurrent confinement in graphene bilayer weak links”. In: *Nat. Commun.* 9 (2018), p. 1722.

[26] F. E. Schmidt et al. “A ballistic graphene superconducting microwave circuit”. In: *Nat. Commun.* 9 (2018), p. 4069.

[27] J. G. Kroll et al. “Magnetic field compatible circuit quantum electrodynamics with graphene Josephson junctions”. In: *Nat. Commun.* 9 (2018), p. 4615.

[28] A. W. Draelos et al. “Supercurrent Flow in Multiterminal Graphene Josephson Junctions”. In: *Nano Lett.* 19 (2019), p. 1039.

[29] J. I.-J. Wang et al. “Coherent control of a hybrid superconducting circuit made with graphene-based van der Waals heterostructures”. In: *Nat. Nanotech.* 14 (2019), p. 120.

[30] L. Bretheau et al. “Tunnelling spectroscopy of Andreev states in graphene”. In: *Nat. Phys.* 13 (2017), p. 756.

[31] D. K. Efetov et al. “Specular interband Andreev reflections at van der Waals interfaces between graphene and $NbSe_2$”. In: *Nat. Phys.* 12 (2016), p. 328.

[32] M. Popinciuc et al. “Zero-bias conductance peak and Josephson effect in graphene-NbTiN junctions”. In: *Phys. Rev. B* 85 (2012), p. 205404.

[33] T. Han et al. “Investigation of the two-gap superconductivity in a few-layer $NbSe_2$-graphene heterojunction”. In: *Phys. Rev. B* 97 (2018), 060505(R).

[34] L. Wang et al. “One-dimensional electrical contact to a two-dimensional material”. In: *Science* 342 (2013), p. 614.

[35] A. A. Golubov and M.Yu. Kupriyanov. “Quasiparticle current of ballistic NcS’S contacts”. In: *JETP Lett.* 61 (1995), p. 851.

[36] F. Pérez-Willard et al. “Determining the current polarization in Al/Co nanostructured point contacts”. In: *Phys. Rev. B* 69 (2004), 140502(R).

[37] J. M. Byers and M. E. Flatté. “Probing Spatial Correlations with Nanoscale Two-Contact Tunneling”. In: *Phys. Rev. Lett.* 74 (1995), p. 306.

[38] G. Deutscher and D. Feinberg. “Coupling superconducting-ferromagnetic point contacts by Andreev reflections”. In: *Appl. Phys. Lett.* 76 (2000), p. 487.

[39] G. Falci, D. Feinberg, and F. W. J. Hekking. “Correlated tunneling into a superconductor in a multiprobe hybrid structure”. In: *Europhys. Lett.* 54 (2001), p. 255.

[40] D. Beckmann, H. B.Weber, and H. v. Löhneysen. “Evidence for Crossed Andreev Reflection in Superconductor-Ferromagnet Hybrid Structures”. In: *Phys. Rev. Lett.* 93 (2004), p. 197003.

[41] D. Beckmann and H. v. Löhneysen. “Negative four-terminal resistance as a probe of crossed Andreev reflection”. In: *Appl. Phys. A* 89 (2007), p. 603.

[42] S. Russo et al. “Experimental Observation of Bias-Dependent Nonlocal Andreev Reflection”. In: *Phys. Rev. Lett.* 95 (2005), p. 027002.

[43] P. Cadden-Zimansky and V. Chandrasekhar. “Nonlocal Correlations in Normal-Metal Superconducting Systems”. In: *Phys. Rev. Lett.* 97 (2006), p. 237003.

[44] L. Hofstetter et al. “Cooper pair splitter realized in a two-quantum-dot Y-junction”. In: *Nature* 461 (2009), p. 960.

[45] L. G. Herrmann et al. “Carbon Nanotubes as Cooper-Pair Beam Splitters”. In: *Phys. Rev. Lett.* 104 (2010), p. 026801.

[46] L. Hofstetter et al. “Finite-Bias Cooper Pair Splitting”. In: *Phys. Rev. Lett.* 107 (2011), p. 136801.

[47] J. Schindele, A. Baumgartner, and C. Schönenberger. “Near-Unity Cooper Pair Splitting Efficiency”. In: *Phys. Rev. Lett.* 109 (2012), p. 157002.

[48] J. Schindele et al. “Nonlocal spectroscopy of Andreev bound states”. In: *Phys. Rev. B* 89 (2014), p. 045422.

[49] Z. B. Tan et al. “Cooper Pair Splitting by Means of Graphene Quantum Dots”. In: *Phys. Rev. Lett.* 114 (2015), p. 096602.

[50] I. V. Borzenets et al. “High Efficiency CVD Graphene-lead (Pb) Cooper Pair Splitter”. In: *Sci. Rep.* 6 (2016), p. 23051.

[51] D. J. Clarke, J. Alicea, and K. Shtengel. “Exotic circuit elements from zero-modes in hybrid superconductor–quantum-Hall systems”. In: *Nat. Phys.* 10 (2014), p. 877.

[52] Z. Hou et al. “Crossed Andreev effects in two-dimensional quantum Hall systems”. In: *Phys. Rev. B* 94 (2016), p. 064516.

[53] G.-H. Lee et al. “Inducing superconducting correlation in quantum Hall edge states”. In: *Nat. Phys.* 13 (2017), p. 693.

[54] T. M. Klapwijk, G. E. Blonder, and M. Tinkham. “Explanation of subharmonic energy gap structure in superconducting contacts”. In: *Physica* 109, 110B (1982), p. 1657.

[55] S. Shapiro. “Josephson currents in superconducting tunneling: The effect of microwave and other observations”. In: *Phys. Rev. Lett.* 11 (1963), p. 80.

[56] C. C. Grimes and S. Shapiro. “Millimeter-wave mixing with Josephson junctions”. In: *Phys. Rev.* 169 (1968), p. 397.

[57] W. W. Webb and R. J. Warburton. “Intrinsic quantum fluctuations in uniform filamentary superconductors”. In: *Phys. Rev. Lett.* 20 (1968), p. 461.

[58] J. D. Meyer and G. v. Minnigerode. “Instabilities in the transition curve of current-carrying one-dimensional superconductors”. In: *Phys. Lett.* 38A (1972), p. 529.

[59] J. E. Mooij and Y. V. Nazarov. “Superconducting nanowires as quantum phase-slip junctions”. In: *Nat. Phys.* 2 (2006), p. 169.

[60] I. M. Pop et al. “Measurement of the effect of quantum phase slips in a Josephson junction chain”. In: *Nat. Phys.* 6 (2010), p. 589.

[61] L. Arndt, A. Roy, and F. Hassler. “Dual Shapiro steps of a phase-slip junction in the presence of a parasitic capacitance”. In: *Phys. Rev. B* 98 (2018), p. 014525.

[62] P. R. Wallace. “The Band Theory of Graphite”. In: *Phys. Rev.* 71 (1947), p. 622.

[63] K. S. Novoselov et al. “Electric Field Effect in Atomically Thin Carbon Films”. In: *Science* 306 (2004), p. 666.

[64] K. S. Novoselov et al. “Two-dimensional atomic crystals”. In: *Proc. Natl. Acad. Sci. U.S.A* 102 (2005), p. 10451.

[65] K. S. Novoselov et al. “Two-dimensional gas of massless Dirac fermions in graphene”. In: *Nature* 438 (2005), p. 197.

[66] S. D. Sarma et al. “Electronic transport in two-dimensional graphene”. In: *Rev. Mod. Phys.* 83 (2011), p. 407.

[67] O. Klein. “Die Reflexion von Elektronen an einem Potentialsprung nach der relativistischen Dynamik von Dirac”. In: *Z. Phys.* 53 (1929), p. 157.

[68] M. I. Katsnelson, K. S. Novoselov, and A. K. Geim. “Chiral tunnelling and the Klein paradox in graphene”. In: *Nature Phys.* 2 (2006), p. 620.

[69] A. F. Young and P. Kim. “Quantum interference and Klein tunnelling in graphene heterojunctions”. In: *Nat. Phys.* 5 (2009), p. 222.

[70] H. B. Heersche et al. “Bipolar supercurrent in graphene”. In: *Nature* 446 (2007), p. 56.

[71] P. Rickhaus et al. “Quantum Hall Effect in Graphene with Superconducting Electrodes”. In: *Nano Lett.* 12 (2012), p. 1942.

[72] K. Komatsu et al. “Superconducting proximity effect in long superconductor/graphene/superconductor junctions: From specular Andreev reflection at zero field to the quantum Hall regime”. In: *Phys. Rev. B* 86 (2012), p. 115412.

[73] N. Mizuno, B. Nielsen, and X. Du. “Ballistic-like supercurrent in suspended graphene Josephson weak links”. In: *Nat. Commun.* 4 (2013), p. 2716.

[74] P. Rickhaus et al. “Ballistic interferences in suspended graphene”. In: *Nat. Commun.* 4 (2013), p. 2342.

[75] F. Miao et al. “Phase-coherent transport in graphene quantum billiards”. In: *Science* 317 (2007), p. 1530.

[76] E. H. Hwang, S. Adam, and S. Das Sarma. “Carrier Transport in Two-Dimensional Graphene Layers”. In: *Phys. Rev. Lett.* 98 (2007), p. 186806.

[77] J. Martin et al. “Observation of electron–hole puddles in graphene using a scanning single-electron transistor”. In: *Nat. Phys.* 4 (2008), p. 144.

[78] K. I. Bolotin et al. “Ultrahigh electron mobility in suspended graphene”. In: *Solid State Commun.* 146 (2008), p. 351.

[79] X. Du et al. “Approaching ballistic transport in suspended graphene”. In: *Nat. Nanotechnol* 3 (2008), p. 491.

[80] K. I. Bolotin et al. “Observation of the fractional quantum Hall effect in graphene”. In: *Nature* 462 (2009), p. 196.

[81] C. R. Dean et al. “Boron nitride substrates for high-quality graphene electronics”. In: *Nat. Nanotechnol.* 5 (2010), p. 722.

[82] G. Giovannetti et al. “Doping graphene with metal contacts”. In: *Phys. Rev. Lett.* 101 (2008), p. 026803.

[83] M. Yankowitz et al. “Van der Waals heterostructures combining graphene and hexagonal boron nitride”. In: *Nat. Rev. Phys.* 1 (2019), p. 112.

[84] A. K. Geim and I. V. Grigorieva. “Van der Waals heterostructures”. In: *Nature* 499 (2013), p. 419.

[85] A. C. Ferrari et al. “Raman Spectrum of Graphene and Graphene Layers”. In: *Phys. Rev. Lett.* 97 (2006), p. 187401.

[86] L .M. Malard et al. “Raman spectroscopy in graphene”. In: *Phys. Rep.* 473 (2009), p. 51.

[87] A. C. Ferrari and D. M. Basko. “Raman spectroscopy as a versatile tool for studying the properties of graphene”. In: *Nat. Nanotechnol.* 8 (2013), p. 235.

[88] M. B. el Mekki et al. “Structure investigation of BN films grown by ion-beam-assisted deposition by means of polarised IR and Raman spectroscopy”. In: *Surf. Coat. Technol.* 116-119 (1999), p. 93.

[89] Jens Mohrmann. “Quantum Transport and Shot Noise in Graphene-Boron Nitride Heterostructures”. Doctoral thesis. Karlsruhe Institute of Technology, 2016.

[90] P. Pandey et al. “Andreev reflection in ballistic normal metal/graphene/superconductor junctions”. In: *Phys. Rev. B* 100 (2019), p. 165416.

[91] P. A. Khomyakov et al. “First-principles study of the interaction and charge transfer between graphene and metals”. In: *Phys. Rev. B* 79 (2009), p. 195425.

[92] P. A. Khomyakov et al. “Nonlinear screening of charges induced in graphene by metal contacts”. In: *Phys. Rev. B* 82 (2010), p. 115437.

[93] K. von Klitzing, G. Dorda, and M. Pepper. “New Method for High-Accuracy Determination of the Fine-Structure Constant Based on Quantized Hall Resistance”. In: *Phys. Rev. Lett* 45 (1980), p. 494.

[94] Supriyo Datta. *Electronic Transport in Mesoscopic Systems.* Cambridge, 2009.

[95] J. R. Williams, L. DiCarlo, and C. M. Marcus. “Quantum Hall Effect in a Gate-Controlled p-n Junction of Graphene”. In: *Science* 317 (2007), p. 638.

[96] D. A. Abanin and L. S. Levitov. “Quantized Transport in Graphene p-nJunctions in a Magnetic Field”. In: *Science* 317 (2007), p. 641.

[97] S. Cho and M. Fuhrer. “Massless and massive particle-in-a-box states in single- and bi-layer graphene”. In: *Nano Res.* 4 (2011), p. 385.

[98] A. L. Grushina, D.-K. Ki, and A. F. Morpurgo. “A ballistic pn junction in suspended graphene with split bottom gates”. In: *Appl. Phys. Lett.* 102 (2013), p. 223102.

[99] F. Wu et al. “Shot noise with interaction effects in single-walled carbon nanotubes”. In: *Phys. Rev. Lett.* 99 (2007), p. 156803.

[100] J. Bardeen, L. N. Cooper, and J. R. Schrieffer. “Theory of Superconductivity”. In: *Phys. Rev.* 108 (1957), p. 1175.

[101] K. Maki. “The behavior of superconducting thin films in the presence of magnetic fields and currents”. In: *Prog. Theor. Phys.* 31 (1964), p. 731.

[102] R. Meservey and P. M. Tedrow. “Tunneling measurements on spin-paired superconductors with spin-orbit scattering”. In: *Phys. Rev. B* 11 (1975), p. 4224.

[103] F. K. Wilhelm, G. Schön, and A. D. Zaikin. “Mesoscopic Superconducting–Normal Metal–Superconducting Transistor”. In: *Phys. Rev. Lett.* 81 (1998), p. 1682.

[104] J. J. A. Baselmans et al. “Reversing thedirectionof the supercurrent in a controllable Josephson junction”. In: *Nature* 397 (1999), p. 43.

[105] P. Samuelsson et al. “Nonequilibrium Josephson effect in mesoscopic ballistic multiterminal SNS junctions”. In: *Phys. Rev. B* 62 (2000), p. 1319.

[106] A. Richter, P. Baars, and U. Merkt. “Supercurrents in two-dimensional electron systems”. In: *Physica E* 12 (2002), p. 911.

[107] Th. Schäpers et al. “Current-injection in a ballistic multiterminal superconductor/two-dimensional electron gas Josephson junction”. In: *Phys. Rev. B* 67 (2003), p. 014522.

[108] S. Sopic. “Superconducting proximity effect in graphene”. Doctoral thesis. University of Geneva, 2015.

[109] A. Barone and G. Paterno. *Physics and Applications of the Josephson Effect.* Wiley Interscience, 1982.

[110] J. C. Cuevas and F. S. Bergeret. “Magnetic Interference Patterns and Vortices in Diffusive SNS Junctions”. In: *Phys. Rev. Lett.* 99 (2007), p. 217002.

[111] F. S. Bergeret and J. C. Cuevas. “The Vortex State and Josephson Critical Current of a Diffusive SNS Junction”. In: *J Low Temp Phys* 153 (2008), p. 304.

[112] L. Angers et al. “Proximity dc squids in the long-junction limit”. In: *Phys. Rev. B* 77 (2008), p. 165408.

[113] F. Chiodi et al. “Geometry-related magnetic interference patterns in long SNS Josephson junctions”. In: *Phys. Rev. B* 86 (2012), p. 064510.

[114] M. Amado et al. “Electrostatic tailoring of magnetic interference in quantum point contact ballistic Josephson junctions”. In: *Phys. Rev. B* 87 (2013), p. 134506.

[115] H. B. Heersche et al. “Induced superconductivity in graphene”. In: *Solid State Commun.* 143 (2007), p. 72.

[116] M. P. Nowak, M. Wimmer, and A. R. Akhmerov. “Supercurrent carried by nonequilibrium quasiparticles in a multiterminal Josephson junction”. In: *Phys. Rev. B* 99 (2019), p. 075416.

[117] J. Cayssol. “Crossed Andreev Reflection in a Graphene Bipolar Transistor”. In: *Phys. Rev. Lett* 100 (2008), p. 147001.

[118] J. Linder, M. Zareyan, and A. Sudbø. “Spin-switch effect from crossed Andreev reflection in superconducting graphene spin valves”. In: *Phys. Rev. B* 80 (2009), p. 014513.

[119] D. Greenbaum et al. “Pure spin current in graphene normal-superconductor structures”. In: *Phys. Rev. B* 75 (2007), p. 195437.

Acknowledgements

I would like to thank all the people who supported me during the course of my doctoral research and made my stay in Karlsruhe wonderful.

I thank the Deutscher Akademischer Austauschdienst (DAAD) for providing the financial support through the DAAD PhD scholarship programme.

I am indebted to Prof. Dr. Detlef Beckmann and Dr. Romain Danneau for their guidance and support as my PhD advisors. Without their help, motivation and patience, it would be very hard for me to finish my work. I am also thankful to Prof. Dr. Wolfgang Wernsdorfer for being the co-referee for my doctoral thesis.

I am highly grateful to Prof. Dr. Ralph Krupke for his support as the head of the research unit. I am thankful to the entire Krupke group in INT as they are the nicest colleagues I could have ever imagined. It has been a pleasure to work with them. I am specially thankful to Rainer, my colleague and officemate, who has always been there to help me out with my work.

Special thanks to my friends Pranauv, Shyam, Veena and Aswathi who never let me feel that I was far away from home. They made it home for me here in Karlsruhe.

There are no words for me to thank my family who has loved me, believed in me, and always wants the best for me. All that I can say at this point is that I am blessed to have them in my life.